OBSERVATION OF NUCLEAR SHADOWING AT LOW X_{Bj} IN CARBON, CALCIUM AND LEAD

BY

TIMOTHY J. CARROLL
B.S., University of Illinois, Urbana, IL. 1985

THESIS

Submitted as partial fulfillment of the requirements
for the degree of Doctor of Philosophy in Physics
in the Graduate College of the
University of Illinois at Chicago, 1994

Chicago, Illinois

Press on, nothing in the world can take the place of persistence. Talent will not: nothing is more common than unsuccessful men with talent. Genius will not: unrewarded genius is almost a proverb. Education alone will not: the world is full of educated derelicts. Persistence and determination alone are omnipotent.

Author Unknown

This thesis is dedicated to my parents.

ACKNOWLEDGMENTS

I would like to express my gratitude to my thesis committee: Mark Adams(Chairman), Clive Halliwell, Shuichi Kunori, Don Mcleod and Antonio Pagnementa.

Now, since this thesis did not come out of thin air, I guess it is time to give credit were credit is due. First and foremost I'd like to thank Mark Adams. Aside from guiding me through this analysis, he was also was my mentor and the father of the SAT trigger upon which this analysis is based. David Jaffe was the other prominent figure in the development of the SAT, as well as the techniques used in the analysis of the low x_{Bj} kinematic region. I would also like to thank Clive Halliwell and Don Mcleod for their painstaking proofreading of this thesis. Gone but not forgotten is Steve Magill who was responsible not only for working on the small angle pattering recongnition code, but also for breaking in these professors for me. Mark, David, Clive, Don and Steve all deserve a round of applause.
Clap, clap, clap.

Another group of people which deserve mention are our Fermilab collaborators who were responsible for the unglamorous task of data production and splitting. Even though splitting/data reduction sounds like it's more fun than people should be allowed to have, Steve Wolbers and John Schell deserve thanks.
Clap, clap, clap.

The E665 spectrometer and software the result of hard work by several people. When I came to E665 the production code had already been written, by people like Harry Melanson, John Ryan, Alex Savalrani, Ahwar Bhatti, Wolfgang Wittek and a many more.
Clap, clap, clap.

The calorimeter is understood because of the efforts of Ashutosh Kotwal, Guang Fang and Michael Schmitt, from Harvard University.
Clap,clap,clap.

Thanks also to my fellow graduated students who have been "down in the trenches" all these years: Arijit, Mark Baker, Janet Conrad, Rob Kennedy, Spentz, Bill, Mathias, Pat Madden and especially Guo. Well, Guo, we made it, keep working on that golf game! For anybody I failed to mention- sorry.

TJC

TABLE OF CONTENTS

1 THE A-DEPENDENCE OF SHADOWING 1

1.1 Lepton Nucleon Scattering 1

1.1.1 Elastic Lepton Nucleon Scattering 2

1.1.2 Inelastic Lepton Nucleon Scattering 5

1.1.3 DIS and the Quark-Parton Model 11

1.2 Nuclear Effects in DIS 13

1.2.1 Experimental Review of Virtual Photon Shadowing 14

1.2.2 Why Study Shadowing? 18

1.2.3 Theoretical Interpretations of Shadowing 19

1.2.4 Generalized Vector Dominance Models 19

1.2.5 Parton Recombination Models 23

1.3 Summary 26

2 EXPERIMENTAL APPARATUS 28

2.1 General Overview 28

2.2 The Beam 30

2.3 The Beam Spectrometer 31

2.4 Targets 35

2.5 Forward Spectrometer 39

2.6 Electromagnetic Calorimeter 46

2.7 Muon Identification 49

2.8 Scalers 50

2.8.1 Spill Scalers 51

2.8.2 Event Scalers 51

2.9 Triggers 53

2.9.1 Small Angle Trigger 53

2.9.2 The SAT "Clean" Signals: Cluster and No Neighbor 61

2.9.3 SATPS and RSAT Triggers 64

2.10 Data Acquisition 66

2.11 Summary 67

3 OFFLINE RECONSTRUCTION 68

3.1 Decoding and Translation 69

3.2 Pattern Recognition 70

3.2.1 Beam Pattern Recognition 71

3.2.2 Forward Spectrometer Muon Phase 72

3.2.3 Forward Spectrometer Hadron Phase 72

3.3 Track Fitting 73

3.4 Muon Matching 73

3.4.1 Multiple Scatter Matching 74

3.4.2 Intersection Match 76

3.4.3 Ray Trace Matching 76

3.5 Vertexing 77

3.6 VDC Pattern Recognition 78

3.7 Electromagnetic Calorimeter 79

3.8 Run90 Filter 81

3.9 Data Reduction and Splitting 82

3.10 The LOX Program: PAW DST Generation 84

3.10.1 Beam Quality Requirements 84

3.10.2 Physics Trigger Requirements 87

3.11 Data Validation 88

3.12 Summary 93

4 ANALYSIS CUTS 94

4.1 DST Distributions 94

4.2 Run Dependence 95

4.2.1 Alignment 96

4.2.2 Scalers 98

4.2.3 Interfile Event Loss 101

4.2.4 Calorimeter Response 103

4.2.5 Target Cycling 106

4.3 Kinematics Cuts 107

4.3.1 Minimum Q^2 108

4.3.2 Maximum y_{Bj} 112

4.3.3 Resolution 112

4.4 Calorimeter Cuts 112

4.4.1 μe^- and $\mu\gamma$ Backgrounds 113

4.4.2 Separating Hadron and Electron Clusters in the Calorimeter 115

4.4.3 Effectiveness of the Cal Cuts 118

4.4.4 DIS Event Topology 122

4.5 Minimum ν 125

4.6 Muon Reconstruction 127

4.7 Summary 127

5 CORRECTIONS TO RAW EVENT YIELDS 129

5.1 Raw Event Distributions 129

5.2 Normalization 131

5.2.1 Solid Target Densities 131

5.2.2 Liquid Deuterium Density 132

5.3 Beam Flux 135

5.3.1 Normalization Uncertainty 137

5.4 Empty Target Subtraction 138

5.4.1 Empty Target Distributions 138

5.5 Target Density Effects 143

5.5.1 Thin to Thick Carbon Comparison 144

5.5.2 SAT Self-Vetos 145

5.6 Sensitivity to the Applied Cuts 153

5.7 Fully Corrected Ratios 154

5.8 Summary 156

6 COMPARISON WITH THEORY AND PREVIOUS RESULTS 158

6.1 Saturation of Shadowing 158

6.1.1 The Onset of Saturation 159

6.1.2 Comparison with Theoretical Predictions 161

6.2 A-Dependence 164

6.3 Q^2-Dependence 169

6.4 ν-Dependence 169

6.5 Comparison with Previous Results 175

6.6 Summary 180

7 SUMMARY AND CONCLUSIONS 182

7.1 Summary 182

7.2 Conclusions 183

LIST OF FIGURES

1.1 Muon-Electron Scattering Feynman Diagram 2

1.2 Deep Inelastic Scattering Feynman Diagram 6

1.3 Photon-Parton Scattering in a Breit Frame. 10

1.4 F_2^A/F_2^D Verses x_{Bj} 17

1.5 Vector Meson Dominance 20

1.6 Parton Recombination Feynman Diagrams. 24

2.1 The Momentum Distribution of the Fermilab Muon Beam. 32

2.2 The E665 Beam Spectrometer 34

2.3 Beam Distribution at PBT 4(Y) 35

2.4 Beam Distribution at PBT 4(Z) 35

2.5 The Run90 Movable Target Assembly 36

2.6 Muon Lab Floor Plan 40

2.7 PSA-SSA Orientation 43

2.8 SSA Hodoscope Counters 43

2.9 SSA Scintillator and Fiber Optics Arrangement 44

2.10 $\mathrm{Log}_{10}(Q^2)$ v $\mathrm{Log}_{10}(\theta)$ For Sat Triggers 54

2.11 Muon Position at PTM1Y(Y) 55

2.12 Muon Position at PTM1Y(Z) 55

2.13 Schematic Representation of the SAT Trigger. 59

2.14 SAT No Neighbor Logic Diagram 63

3.1 Muon Match Schematic 77

3.2 Vertex Chamber Resolution 80

3.3 Beam Multiplicity Distribution 85

3.4 Beam Momentum Resolution 85

3.5 The SBT Reflection 86

3.6 Analysis Flowchart 90

3.7 Comparison of Scatters from DR90 and PTMV 93

4.1 ν For Unscattered Beam 97

4.2 $< \nu >$ For Unscattered Muons vs.Run 97

4.3 Comparison of RSAT to Spill Scalers 100

4.4 $\mu\gamma$/beam 102

4.5 $\mu\gamma$/beam Interfile Event Loss 102

4.6 Calorimeter Energy For DIS Candidates 104

4.7 Bad Runs Based on Calorimeter Response 105

4.8 Trigger Acceptance for "Bare" Muons vs. Q^2 109

4.9 Q^2 Acceptance: Ca/D 110

4.10 Q^2 Acceptance: Pb/D 110

4.11 Trigger Acceptance for "Bare" Muons vs. y_{Bj} 111

4.12 y_{Bj} Acceptence: Ca/D 111

4.13 y_{Bj} Acceptence: Pb/D 111

4.14 Fractional Error on x_{Bj} 113

4.15 The x_{Bj} Distribution of Elastic μe^- Scatters 114

4.16 The Q^2 Dependence of $\mu\gamma$ Scatters 114

4.17 Eclus/Ptrack for Electrons 117

4.18 Eclus/Ptrack for Hadrons 117

4.19 Cluster Energy from Electrons 118

4.20 Cluster Energy from Hadrons 118

4.21 Identifying Muon Bremsstrahlung Using ECAL 121

4.22 Identifying Elastic Muon-Electron Scattering Using ECAL 123

4.23 x_{Bj} Distribution Before and After Calorimeter Cuts 124

4.24 Planarity 126

4.25 Planarity Comparing DIS Cuts 126

4.26 Fractional Error on ν After x_{Bj} Resolution Cuts 126

5.1 $\text{Log}_{10}(x_{Bj})$ Before and After CAL Cuts 130

5.2 Deuterium Pressure Transducer Calibration 132

5.3 Deuterium Density Verses Time 133

5.4 Deuterium Density 133

5.5 Corrected Density Verses Time 134

5.6 Corrected Density 134

5.7 Vertex Distribution For Full And Empty Targets 140

5.8 x_{Bj} Dependence of the Empty Target Correction 141

5.9 x_{Bj} Cross Section Ratio of Thin to Thick Carbon 145

5.10 Muon Topology for SAT Self-Veto Candidates 147

5.11 Muon Topology Final Self-Veto Sample 148

5.12 SAT Self-Veto Rate As a Function of x_{Bj} 150

5.13 Fully Corrected Nuclear Cross Section Ratios 155

6.1 Saturation Onset vs Atomic Number 160

6.2 Saturation Ratio vs Atomic Number 160

6.3 Comparison of the A-Dependence with a GVD Prediction 163

6.4 Logarithmic A-Dependence of Shadowing 165

6.5 Logarithmic A-Dependence vs x_{Bj} 166

6.6 R(A) verses x_{Bj} 168

6.7 Q^2-Dependence of Shadowing for Carbon 170

6.8 Q^2-Dependence of Shadowing for Calcium 171

6.9 Q^2-Dependence of Shadowing for Lead 172

6.10 Logarithmic Q^2-Dependence vs x_{Bj} 173

6.11 Nuclear Cross Section Ratios as a Function of ν 176

6.12 Comparison with Previous Results 177

6.13 A_{eff}/A for Cu (Q^2=0) 179

6.14 σ^A/σ^D E665 Xe 179

6.15 $dR(\nu)/d\nu$ Verses Atomic Number 180

LIST OF TABLES

TABLE		PAGE
I	Beam Station Wire Planes	29
II	Target Properties.	34
III	SSA Hodoscope Components	40
IV	S mall Angle Trigger Matrix Hardware Map.	52
V	Small Angle Trigger Prescale Factors.	58
VI	Run90 Data Reduction Cuts	74
VII	DST Beam Requirements	78
VIII	DST Physics Requirements	79
IX	Event Statistics Before Analysis Cuts	86
X	Fit Parameters for RSAT Prescale Validation	91
XI	Interfile Event Loss $\sigma(\mu\gamma)$ Versus Target	93
XII	Event Statistics Before Kinematic Cuts	98
XIII	Final Event Statistics	116
XIV	Target Dependence Of Beam Flux Measurements	125
XV	Empty Target Material For Each Target Configuration	130
XVI	Calculated and Measured Empty Target Corrections	131
XVII	Fits to the SAT Self-Veto Rate Verses x_{Bj}	138
XVIII	$R_s(x_{Bj})$:Nuclear Cross Section Ratio Saturation	146

XIX $R_s(x_{Bj})$ in the Saturation Region-Comparison with Theory 147

XX Statistical Analysis R(A) verses x_{Bj} 153

XXI $d(R(x_{Bj}))/d(Log(Q^2))$: Q^2-Dependence of Shadowing 157

XXII Q^2-Dependence Verses x_{Bj} 157

XXIII Linear Fits to $R(\nu)$ Verses ν 160

XXIV Carbon/Deuterium Cross Section Ratio Verses x_{Bj} 169

XXV Calcium/Deuterium Cross Section Ratio Verses x_{Bj} 169

XXVI Lead/Deuterium Cross Section Ratio Verses x_{Bj} 170

XXVII Fully Corrected x_{Bj} Distributions for Deuterium 170

XXVIII Fully Corrected x_{Bj} Distributions for Carbon 171

XXIX Fully Corrected x_{Bj} Distributions for Calcium 171

XXX Fully Corrected x_{Bj} Distributions for Lead 172

XXXI Carbon/Deuterium Cross Section Ratio Verses ν 172

XXXII Calcium/Deuterium Cross Section Ratio Verses ν 173

XXXIII Lead/Deuterium Cross Section Ratio Verses ν 173

LIST OF ABBREVIATIONS

CCM	Chicago Cyclotron Magnet
CVM	Cern Vertex Magnet
DIS	Deep Inelastic Scattering
DC	Drift Chamber
ECAL	Electromagnetic CALorimeter
EMC	European Muon Collaboration
FNAL	Fermi National Accelerator Laboratory
GVD	Generalized Vector Dominance
LAT	Large Angle Trigger
NMC	New Muon Collaboration
PBT	Proportional Beam Tagging chamber
PR	Parton Recombination
PSA	Proportional Small Angle chamber
PTMV	Pattern recongnition,Track fitting, Muon match, Vertexing
QCD	Quantum ChromoDynamics
QED	Quantum ElectroDynamics
RSAT	Randomly prescale Small Angle beam Trigger
SAT	Small Angle Trigger
SATPS	Small Angle Trigger Pre Scaled
SMS	Small angle Muon Scintillators
SSA	Scintillation Small Angle hodoscope

SUMMARY

Nuclear shadowing has been studied through the process of deep inelastic muon scattering. Positive muons with a mean energy of 468 GeV/c were scattered from targets of deuterium, carbon, calcium and lead. Per-nucleon cross section ratios have been observed to exhibit "Shadowing", that is, cross section ratios of heavy nuclear targets to deuterium lie below unity when measured at small values of the Bjorken scaling variable, x_{Bj}.

Shadowing has been studied as a function of the atomic number of the target, the energy transfer to the target and the momentum transfer to the target. Results indicate the degree of shadowing becomes constant in the region $xbj < 0.001$. In addition the measured effect is consistent with a theoretical interpretation based on the Generalized Vector Meson dominance interpretation of shadowing.

1. THE A-DEPENDENCE OF SHADOWING

1.1 Lepton Nucleon Scattering

Over the past several decades much of what we know about the theory of strong interactions, quantum chromodynamics(QCD) has come from lepton scattering experiments. Since the electroweak interaction of leptonic probes is relatively well understood, electron, muon and neutrino probes, as a consequence of their pointlike nature, have been very useful in revealing nuclear structure. The following discussion will trace the history of lepton scattering, beginning with the simplest QED scattering cross section and conclude with nuclear effects in deep inelastic scattering(DIS).

1.1.1 Elastic Lepton Nucleon Scattering

As a starting point for the discussion of deep inelastic scattering, consider the simple QED process of elastic muon-electron scattering(μe^-). Both muons and electrons are Dirac particles and so have no measurable structure at current available energies, making the scattering diagram calculable in QED. In the Born approximation, single photon exchange(see figure 1.1), the scattering amplitude is the contraction of 2 fermion currents via a photon propagator,

$$\mathcal{M} = -e^2\overline{u}(k')\gamma^\mu u(k)\frac{1}{q^2}\overline{u}(p')\gamma_\mu u(p) \tag{1.1}$$

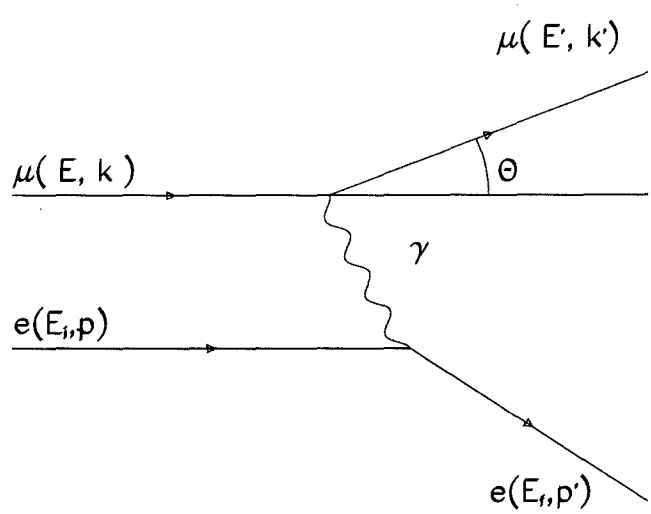

Figure 1.1: Muon-Electron Scattering Feynman Diagram

After spin summing/averaging and contracting the currents, the modulus squared of the

matrix element may be expressed as the product of two symmetric tensors, that of the muon and that of the electron

$$| \overline{\mathcal{M}} |^2 = \frac{e^2}{q^4} L_{\mu\nu}(\text{electron}) L^{\mu\nu}(\text{muon}). \tag{1.2}$$

This leads to the differential cross section:

$$\frac{d^2\sigma}{dE' d\Omega} = \frac{\alpha^2 E'^2}{Q^4} \left[cos^2(\theta/2) + \frac{Q^2}{2M_e^2} sin^2(\theta/2) \right] \delta(\nu - \frac{Q^2}{2M_e}) \tag{1.3}$$

where the energy transferred to the electron is: $\nu = \mathrm{E} - \mathrm{E}'$ and the momentum transfer is given by $q_\nu = (\nu, (\vec{k} - \vec{k'}))$ with $Q^2 \equiv -q_\mu q^\mu$. There are a few important things which can be learned about the physics of spin-1/2 spin-1/2 scattering from equation 1.3. The first term in the brackets is the Mott scattering result for scattering of a spin-1/2 object from a static electric field. The forward peaking $\cos^2(\theta/2)$ dependence is a result of helicity conservation. In the high energy limit, the incoming lepton is in a helicity eigenstate and after the interaction the outgoing lepton must have the same helicity. Back scattering requires the electron to flip its spin in order to conserve helicity and is allowed in μe^- scattering. The second term describes the back scattering in μe^- interactions because, if both leptons flip their spins, helicity and the total spin of the μe system may be conserved. The angular dependence of μe scattering is important in determining the spin of the partons in deep inelastic scattering. To summarize, the distribution is forward peaked due to the interaction of a charge with an electric field, and back scattering is allowed from the "magnetic" spin-spin interaction.

The previous discussion relied on the coupling of the photon propagator to the muon and

electron being pointlike. In order to use the formalism introduced above for extended objects, a nucleon for example, one needs to account for the non-pointlike nature of the target. This is done by expressing the coupling to the nucleon in terms of an expansion in the Dirac matrices, k_μ and k'_μ. The result of this generalization is that the cross section depends on two unknown functions, the form factors, $G_M(Q^2)$ and $G_E(Q^2)$,

$$\frac{d\sigma}{d\Omega} = \frac{\alpha^2}{4E^2 sin^4(\theta/2)}(\frac{E'}{E})\left[\frac{G_E^2(Q^2)+\tau G_M^2(Q^2)}{1+\tau}cos^2(\theta/2)+2\tau G_M^2 sin^2(\theta/2)\right] \tag{1.4}$$

where $\tau = Q^2/4m^2$. These form factors betray our ignorance of the γN coupling.

Comparing with the μe scattering result(1.3), the identification of G_M as the "magnetic form factor", because it is the cofactor of the spin-flip, backscattering term is obvious. Similarly the cosine term is referred to as the "electric form factor". In the limit that no structure exists, the form factors approach unity and the point-point interaction result is recovered. The form factors are unknown, they have not been determined in a theoretical manner. The reader should note that the nucleon remains intact in this type of interaction.

Experimental measurements of the scattering cross sections have been made for Q^2 values up to several hundred GeV^2 (1). Measurements of the electric form factor $\mathrm{G_E}(Q^2)$ find that the form factor is well described by

$$\mathrm{G_E}(Q^2) = (1 + Q^2/0.71\mathrm{GeV}^2)^{-2}. \tag{1.5}$$

Physically, what is happening? Since momentum and wavelength are related by

$$\lambda_\gamma = h/p = hc/\sqrt{Q^2} \tag{1.6}$$

as momentum transfer Q^2 increases, the photon's wavelength decreases, thereby increasing its spatial resolution. So if the nucleon is thought of as an extended cloud of charge, as the resolution of the photon increases, it no longer "sees" the entire nucleon's charge. Expressing equation 1.5 in coordinate space by taking its Fourier transform yields a proton charge distribution with a mean radius of $< r_P > \cong 0.86$ fm.

1.1.2 Inelastic Lepton Nucleon Scattering

Logically, the next step in lepton nucleon scattering experiments was to increase the Q^2 of the probe in order to search for more structure. In order to increase the resolution of the probe we can require a large energy transfer to the photon since:

$$Q^2 = (\nu^2 - (\vec{k} - \vec{k'})^2) \tag{1.7}$$

Therefore, by increasing the energy transfer, ν, one will increase the resolving power of the photon. When the energy transfer is "large", the photon dumps enough energy into the nucleon to break it apart, see figure 1.2. In the case where the scattering was elastic, the nucleon remained intact and so the nucleon's final state is accurately described by a Dirac spinor. For interactions in which the nucleon breaks apart, the final state is a many-particle state and the matrix element must reflect this.

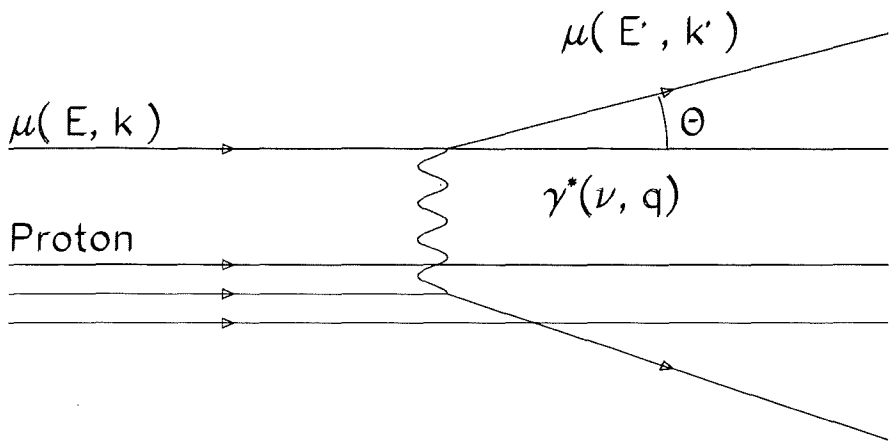

Figure 1.2: Deep Inelastic Scattering Feynman Diagram

In analogy to generalizing the photon coupling in the case of elastic nucleon scattering, the matrix element can be expressed generally so that it takes into account our lack of knowledge of the hadronic final state of the struck nucleon. It is expressed as a tensor symmetric in $\mu\nu$.

$$\overline{\mathcal{M}}^2 = L_{\mu\nu}(e^-)W^{\mu\nu}(target) \tag{1.8}$$

The most general expression, $W^{\mu\nu}$, after requiring conservation of flux, and parity (for the case of muon-nucleon only, neutrino-nucleon scattering allows for a parity violating term), reduces to two terms. This leads to the form of the scattering cross section for inelastic scattering:

$$\frac{d^2\sigma}{dE'd\Omega} = \frac{\alpha^2}{4E^2 sin^4(\theta/2)}\left[W_2(Q^2,\nu)cos^2(\theta/2) + 2W_1(Q^2,\nu)sin^2(\theta/2)\right] \tag{1.9}$$

The result of measuring the inelastic scattering cross section at large Q^2 revealed a remarkable result. The cross section did not vanished as expected. Recalling equation 1.5 it was expected

that the cross section should fall off as $1/Q^4$. Instead, the inelastic structure functions exhibited *scale invariance* (2). Simply put, Bjorken predicted that in the limit $Q^2 \rightarrow \infty$ with the ratio ν/Q^2 fixed, the structure functions $W_{1,2}$, loose their dependence on Q^2 and become functions only of the dimensionless ratio $\omega = Q^2/M\nu$, explicitly, in the Bjorken limit:

$$\lim_{\mathbf{Bj}} W_1(Q^2,\nu) \rightarrow f_1(\omega) \quad \text{and} \quad \lim_{\mathbf{Bj}} \nu W_2(Q^2,\nu) \rightarrow f_2(\omega) \tag{1.10}$$

This phenomenon was interpreted by Feynman as being evidence that nucleons are composed of several spin-1/2 point particles which he called "partons" (3). Feynman considered a frame of reference in which the nucleon has momentum large enough so that it's $\hat{z}$ component of momentum is much greater than the transverse momentum of it's partons. In this infinite momentum frame, the nucleon appears to be a parallel stream of non-interacting partons. If the fraction of the total nucleon's momentum a parton has is x, and the number of partons in the range $x \rightarrow x + dx$ is $f(x)$, then a parton has momentum xP where P is the momentum of the nucleon. For scattering from a single parton the structure functions become:

$$f(x) = 2MW_1(Q^2,\nu) \quad \text{and} \quad xf(x) = \nu W_2(Q^2,\nu) \tag{1.11}$$

with $x = Q^2/(2M\nu)$, commonly referred to as x_{Bj}, which is half Bjorken scaling variable, $\omega = 2x_{Bj}$. Bjorken scaling was interpreted by Feynman as evidence that electron scattering in the deep inelastic(Bjorken) limit was actually elastic scattering from a spin-1/2 point particles.

Since the scaling property of inelastic scattering is indicative of elastic pointlike scattering, it is logical to compare the cross section formula for inelastic nucleon scattering equation 1.9

to that of pointlike elastic scattering, equation 1.3. By direct comparison of the angular terms, and defining $\mathrm{F}_1(x_{Bj}) = MW_1$ and $\mathrm{F}_2(x_{Bj}) = \nu W_2$:

$$\mathrm{f}(x_{Bj}) = (1/2)\mathrm{F}_1(x_{Bj}) = (1/4)\delta(x_{Bj} - \frac{Q^2}{2M\nu}) \quad \text{and} \quad x_{Bj}\,\mathrm{f}(x_{Bj}) = \mathrm{F}_2(x_{Bj}) = x_{Bj}\,\delta(x_{Bj} - \frac{Q^2}{2M\nu}) \tag{1.12}$$

The delta function in these expressions limits $F_{1,2}$ to be zero unless the momentum fraction of the parton is equal to $Q^2/2\mathrm{M}\nu$. Since F_2 is proportional to x_{Bj}, F_2 is a direct measurement of the parton momentum distribution. In order to account for the fact that partons of different flavor may have different momentum distributions, $\mathrm{f}_i(x_{Bj})$ is summed over all partons and integrated over all x_{Bj}. F_2 may be expressed as:

$$F_2 = \sum_i \int e_i^2\, x_{Bj}\, \mathrm{f}_i(x_{Bj})\, dx_{Bj} \tag{1.13}$$

where the sum runs over all charged parton flavors. The e_i factor accounts for the fact that the electromagnetic coupling is proportional to charge and, the μe cross section which was used in this derivation, assumes a charge of 1. Since partons may have fractional charge, the charge fraction e_i must be included.

There are a few approximations and assumptions implicit in the parton model. First, drawing a direct analogy between μe scattering and parton scattering assumes that partons are spin-1/2. This assumption is responsible for the form of $F_{1,2}$. Additionally, deep inelastic scattering involves virtual photons which are not restricted to having only transverse polarizations. In order to determine how this may effect measurable quantities, consider the photon-nucleon

vertex. By decomposing the total photon-nucleon cross section into longitudinal and transverse components,

$$\begin{aligned}\sigma_{\text{transverse}} &= 1/2(\epsilon_+^{*\mu}\epsilon_+^{\nu} + \epsilon_-^{*\mu}\epsilon_-^{\nu})\mathrm{W}_{\mu\nu} \\ &= 2x_{Bj}\mathrm{F}_1 \qquad (1.14)\\ \sigma_{\text{longitudinal}} &= (\epsilon_0^{*\mu}\epsilon_0^{\nu})\mathrm{W}_{\mu\nu} \\ &= \mathrm{F}_2 - 2x_{Bj}\mathrm{F}_1 \qquad (1.15)\end{aligned}$$

where $\epsilon_{+,-,0}$ is the photon polarization, the inelastic cross sections can be expressed in terms of the ratio of these cross sections,

$$F_2 = 2xF_1(1 + \mathrm{R}) \qquad (1.16)$$

where $\mathrm{R} = \sigma_{\text{longitudinal}}/\sigma_{\text{transverse}}$.

Now consider a frame of reference in which the virtual photon has zero energy, called the Breit frame. A parton can reverse its momentum by absorbing the photon see(figure 1.3).

The parton is in a helicity eigenstate by virtue of its high momentum and spin-1/2 nature. Therefore in order to reverse its momentum, and conserve helicity, the parton must absorb 1 unit of spin from the photon. Since longitudinally polarized photons carry no spin, absorbing the photon and reversing momentum without altering the spin of the parton violates helicity conservation. Therefore scattering of spin-1/2 objects by longitudinal polarized photons is kinematically forbidden, $\sigma_l = 0$. Conversely transverse photons can scatter and conserve helicity by

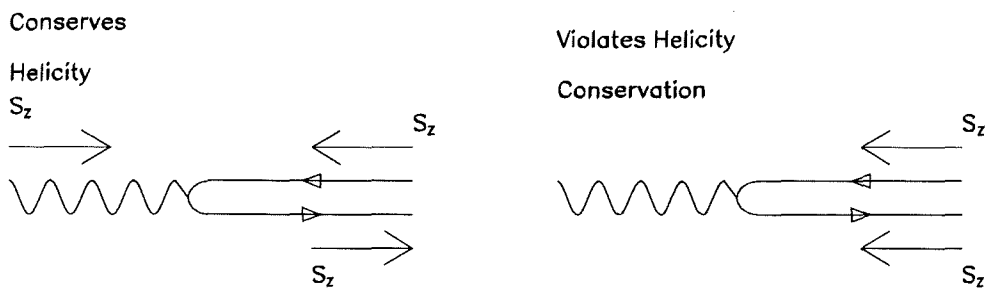

Figure 1.3: Photon-Parton Scattering in a Breit Frame.

imparting their spin to the parton, so $\sigma_t \neq 0$. By this argument, if partons are spin-1/2, then

$$\mathrm{R} = (\frac{\sigma_l}{\sigma_t}) = 0 \quad \text{and} \quad F_2 = 2xF_1 \tag{1.17}$$

Several electron and muon scattering experiments have measured the value of R (21), (22), (23). Typically, measurement errors are large, due to the difficulty involved in this measurement, but results indicate that R is consistent with zero, indicating that partons are indeed spin-1/2.

The assumption that partons behave as a parallel stream of non-interacting partons needs to be justified. This approximation relies on the assertion that in an infinite momentum frame, partons are quasi-free. Because the nucleon is moving relativistically, time dilation causes parton-

parton interactions to take place on a much longer time scale than the photon-parton interaction. Therefore in this frame partons can be considered to be non-interacting during the time in which the photon-parton interaction occurs. The momentum of a parton transverse to the $\hat{z}$ direction can be inferred from size of the nucleons, 1 fm, to be approximately 300 MeV. In a frame of reference which the nucleons have several GeV of energy, the assumption that the partons are moving parallel to each other in the $\hat{z}$ direction is well justified.

1.1.3 DIS and the Quark-Parton Model

Deep inelastic scattering(DIS) has produced experimental results which may be evidence that nucleons are made of quarks. Since the quark-parton model has had success in explaining the spectroscopy of hadrons, it is desirable to identify Feynman's partons as quarks.

In the quark parton model, baryons and mesons, are made of spin-1/2 point particles, quarks. Quarks come in six species referred to as flavors: u,d,s,c,b,t. Quarks carry electric charges of -1/3 and +2/3 as well as color charge. The color charge determines the quarks strong interactions which are mediated by massless gauge bosons called gluons. Gluons have no electric charge and thus are invisible to the electromagnetic interaction which is used to study quarks via inelastic lepton scattering.

Is it possible to show that partons are the quarks of QCD? As discussed previously, scaling is indicative of the point nature of partons. In order to determine the charge of the partons it is

necessary to measure the cross section for neutral current interactions. Neutrino experiments do just that. It has been shown that the ratio of $F_2^{\mu N}/F_2^{\nu N}$ is proportional to the charge squared sum of u and d quarks. Thus measurements in νN experiments indicate that quarks are fractionally charged.

Finally, since F_2 measures the momentum distribution of the charged constituents inside a nucleon, integrating the momentum distribution should yield the nucleon's momentum. Experimentally only 1/2 the momentum of the proton can be accounted for by charged partons. The conclusion is that the uncharged partons, gluons, account for approximately 1/2 of a nucleon's momentum. Another piece of evidence for the existence of gluons is the observation of charmed mesons in DIS, via the process of photon gluon fusion.

To summarize, since the structure function F_2 is independent of the resolution of the probe (when Q^2/ν is held fixed), deep inelastic scattering involves point-particles which make up the nucleon. The experimentally measured values of F_2 and F_1 lead us to believe that these constituents are spin-1/2, and from neutral current measurements of the nucleon's structure function, these spin-1/2 point particles are fractionally charged, and account for only 1/2 of the nucleon's momentum. These results validate the identification of the partons observed in inelastic lepton scattering with the quarks and gluons of quantum chromodynamics.

1.2 Nuclear Effects in DIS

Until the mid 1970's, it was thought that a nucleon's substructure was independent of the type of nucleus it was bound in. Nuclear cross sections were expected to be an incoherent sum of individual nucleon cross sections. If one took an isoscaler target, one in which the number of protons and neutrons are equal, of atomic number, A, and compared its cross section to a loosely bound isoscalar target, deuterium, there should be no difference as a function of x_{Bj}.

$$\sigma^A(x_{Bj}) = A \times \sigma^D(x_{Bj}) \tag{1.18}$$

This is an approximation. Well known nuclear effects like Fermi motion of an individual nucleons are not negligible in certain kinematic regions. Fermi motion was expected to distort the structure functions of heavy nuclear targets for $x_{Bj} > 0.5$ with no distortion at lower values of x_{Bj} (7). Another approximation which is made in interpreting experimental results is that the longitudinal photoabsorption cross section σ_l is the same for nuclei with large atomic numbers. When the deep inelastic scattering cross section is expressed in terms of R(see equation 1.16):

$$\frac{\mathrm{d}^2\sigma^{\mathrm{A}}}{\mathrm{d}x_{Bj}\mathrm{d}Q^2} = \frac{4\pi\alpha^2\mathrm{F}_2^A}{\mathrm{Q}^4 x_{Bj}}\left[1 - y_{bj} - \frac{Q^2}{4\mathrm{E}^2} + \frac{y_{bj}^2 + Q^2/\mathrm{E}^2}{2(1+\mathrm{R}^{\mathrm{A}})}\right] \tag{1.19}$$

it is evident that if R^{A} is the same for all nuclei, then measurements of cross sections are, in effect, measurements of F_2.

Experimentally, even after accounting for the Fermi motion inside the nucleus, the ratio of these cross sections was less than unity. The depletion in the high x_{Bj} region was termed "shadowing" in analogy with the depletion observed in photoproduction experiments. This was first discovered by the European Muon Collaboration(EMC) (4). They were measuring scaling violations with an iron target and discovered the ratio of per nucleon structure functions, F_2^N, was not unity. Expressed in terms of x_{Bj} the ratio was less than 1 at $x_{Bj} > .3$ but as x_{Bj} decreased below .3 the ratio rose above 1. The ratio reached a maximum of 1.15 at the lowest available x_{Bj} value, 0.05. The high x_{Bj} behavior was inconsistent with expectations even after fermi motion corrections were applied, the enhancement of the ratio below $x_{Bj} \sim .3$ was completely unexpected. At the time of the discovery of the enhancement of the iron structure function, it was assumed that there was no difference in R for nuclear targets. Subsequent measurements of the nuclear dependence of R have validated this assumption (25), (25), (22).

1.2.1 Experimental Review of Virtual Photon Shadowing

Some electron scattering experiment performed at the Stanford Linear Accelerator Center(SLAC) had taken data with target vessels made of iron (5), reanalysis of these data confirmed the EMC ratio (6). There existed some discrepancy in the magnitude of the enhancement in the iron cross section relative to deuterium in the x_{Bj} region below .3, but both groups saw an enhancement, even though the SLAC measurement suffered from large statistical errors in the low x_{Bj} region.

Following the EMC results, other groups attempted to measure the "EMC effect" at lower values of x_{Bj} in order to quantify the effect. SLAC Experiment 139 measured cross section ratio for several different targets in order to determine the dependence of the ratio on atomic number (10). Their measurement of the iron ratio showed much less enhancement than the EMC results, but the experiments agreed in the region $x_{Bj} > 0.3$. These results were compared with measurements made by the CERN BCDMS collaboration (11). BCDMS varied Q^2 between 10 - 200 $(\text{GeV})^2$ and found that the cross section ratios of iron and nitrogen to deuterium did not depend on the value of Q^2 as long as the value x_{Bj} was held constant. Their results agreed with the EMC and SLAC results, although their results didn't extend into the region in which EMC saw a 15% enhancement in the ratio. A later attempt by BCDMS to reproduce the EMC effect in iron resulted in a smaller enhancement, approximately 4% as compared to EMC's 15%, in the same Q^2 domain (12).

The x_{Bj} dependence of cross section ratios is displayed in figure 1.4 (15). The ratios for targets of helium, carbon and calcium are compared to weakly bound deuterium. Several CERN and SLAC results are included. All the results have several features in common. First, in the region $x_{Bj} > 0.3$ the ratios fall below unity(denoted as a dashed line). This depletion exists even after the the ratios had been corrected for Fermi motion. The region betweeen $0.01 \lesssim x_{Bj} \lesssim 0.3$, there is a 3-5% enhamncement in the ratios. This enhancement is sometimes call the "EMC" effect. Finally at $x_{Bj} \lesssim 0.08$ the ratios again exhibit a depletion below unity. This low x_{Bj}

depletion is the "shadowing" region.

Several CERN muon experiments continued to measure cross section ratios on various targets. In these experiments, great care was taken to address systematic effects in the data (13), (14), (16), (17), (18). The final results were very precise measurements of the F_2 ratios, with good control over systematic effects at values of x_{Bj} down to 0.01. They found that as the per nucleon structure function ratio was measured at lower values of x_{Bj} the ratio which had risen above 1 at x_{Bj} of .3 turned over and fell below 1 for x_{Bj} values close to 0.1. Targets of helium, lithium, carbon, nitrogen, calcium, iron, copper and tin with atomic numbers of 4, 6, 12, 14, 40, 54, 63, 118, respectively, were studied. Q^2 values ranged from 0.5 $(\mathrm{GeV})^2$ to 90 $(\mathrm{GeV})^2$ (17). The CERN experiments saw a marked dependence on the type of target used. For heavier targets, larger-A, shadowing was more pronounced and was observed at higher values of x_{Bj}.

In 1987, an experiment came on line which used a muon beam produced from the protons accelerated in the Fermilab Tevatron. Fermilab experiment 665 (E665) used the highest energy muon beam available to measure the A-dependence of shadowing in the low x_{Bj} region. This experiment was the earlier phase of the experiment reported on in this thesis. The high beam energy and the use of a "floating veto" low Q^2 trigger allowed E665 to measure shadowing at values of x_{Bj} as low as 0.00002. E665 compared gaseous xenon (A=131) to deuterium. Two independent analyses of the xenon-deuterium cross section ratio determined shadowing was present in xenon (19), (8). In one analysis (8) the cross-section ratio of Xe/D2 was observed

Figure 1.4: F_2^A/F_2^D Verses x_{Bj}

to saturate, that is the amount of shadowing, as a function of x_{Bj}, became constant. The saturation of shadowing had not been observed previously.

1.2.2 Why Study Shadowing?

The measurement of shadowing is important for several reasons. First, as will be discussed in the following section, the explanations of shadowing are based in QCD. Since QCD is a comparatively new theory, measurements of new observables are important feedback to theorists. In addition to nuclear shadowing many theorists believe the shadowing phenomenon will be observable in nucleons. Nucleon shadowing may occur at very high momentum transfers completely analogously to nuclear shadowing. High momentum transfer experiments will have data available shortly(HERA). Another important result from measuring nuclear structure functions at very low x_{Bj} will be the A-dependence of the structure functions, $F_{1,2}$. Experiments at the Relativistic Heavy Ion Collider (RHIC), currently under construction, will have to understand the low x_{Bj} distributions of quarks in nuclear targets in order to interpret their results. Finally, in order to determine structure functions in the widest range of kinematics, researchers combine the results of several experiments. Many of these measurements were made using hydrogen or deuterium targets, but neutrino experiments typically use iron as a target. In order to combine data sets in global fits, the source of shadowing in nuclear targets must be understood.

1.2.3 Theoretical Interpretations of Shadowing

The observation of the dependence of the cross section on x_{Bj} has spawned a plethora of theoretical interpretations. The earliest cross section ratio data were taken at intermediate values of x_{Bj} where the per nucleon cross section rose above 1. Models which attempted to explain this phenomenon have had qualified success. They accurately reproduced the "enhancement" region but break down in the Q^2 and x_{Bj} regions in which later experiments (NMC,SLAC, E665) took measurements. These models deal mostly with conventional nuclear physics explanations. Two classes of models which address the low x_{Bj} kinematical range will be the focus of the following discussion. These models are the generalized vector dominance models (GVD) and the parton recombination models(PR).

1.2.4 Generalized Vector Dominance Models

The generalized vector dominance models are based on the premise that the exchanged virtual photon fluctuates into a $q\bar{q}$ pair or a hadronic state. The hadronic fluctuation must have the same quantum numbers of the γ^*, that is, spin 1 and charge 0. The resulting fluctuation reaches the nuclear surface and interacts hadronically (26). Hadronic cross sections are typically large enough that the mean free path of a hadron in nuclear matter is less than the nuclear diameter of some nuclei. As a result, long lived hadronic fluctuations will tend to be scattered before traversing the entire nucleus. Therefore, the per nucleon cross section for heavy nuclear targets

will be reduced("shadowed")' relative to the free nucleon case due to the scattering of the hadronic component of the photon at the front face of the nucleus.

In the most naive GVD models, the virtual photon fluctuates into a vector meson(ρ, ω, ϕ). The time which the fluctuation survives can be determined from the muon kinematics and the mass of the vector meson. Defined as the *coherence length* , λ_c , it determines the amount of shadowing,

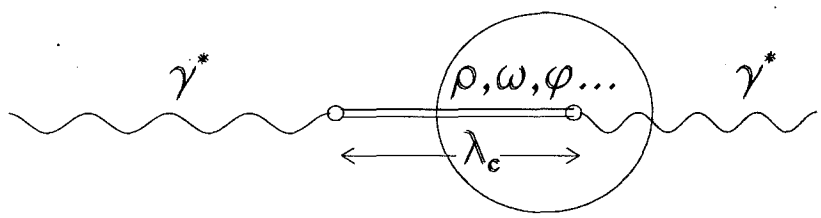

Figure 1.5: Vector Meson Dominance

$$\lambda_c = \frac{2\nu}{(Q^2 + m_v^2)^{1/2}} \tag{1.20}$$

where m_v is the mass of the vector meson (see figure 1.5).

As the coherence length increases, the strength of the photon's hadronic component increases

and the photon exists in its hadronic state for a larger portion of its lifetime, and therefore has a higher probability of interacting hadronically. As the coherence length decreases the fluctuations become shortlived and the photon will tend to interact electromagnetically. From the form of equation 1.20, one would expect a strong Q^2 dependence to shadowing. Various experiments have searched for the Q^2 dependence and there is general agreement that the measured Q^2 dependence is in marked disagreement with the naive GVD model.

In papers by Bilchack,Schildknect and Stroughair (27), (28), they present predictions based on a GVD model which takes into account higher mass vector meson states. They go beyond the naive model proposed above and introduce mixing of off diagonal vector meson states. Their prediction of the A-dependence of shadowing at $Q^2 \cong 2.8(\mathrm{GeV})^2$ shows a very definite saturation which is A-dependent. The range of saturation values are: $0.005 \leq x_{Bj} \leq 0.07$, for A values of 7 to 238. They also present the cross section ratio as a function of atomic number in different Q^2 regions at fixed x_{Bj}. Their results predict that as Q^2 increases, the amount of shadowing decreases, by approximately 10% in the range $0.75 \leq Q^2 \leq 4.6$ with x_{Bj} fixed at 0.0125.

In a paper by Shaw (29) an attempt to reconcile the strong Q^2 dependence of the naive vector dominance models is made by considering the ν dependence of the hadronic cross section. In this model shadowing depends on the mean free path, l_h, of the fluctuation in nuclear matter ($l_h = 1/\mathrm{density}*\sigma$). He uses the ρ^0's cross section as the cross section for the hadronic component

of the virtual photon.

$$\sigma_{\gamma^*} = \sigma_{\rho^0} = a + \frac{b}{\nu^{0.5}} \tag{1.21}$$

Since $\nu = Q^2/2\mathrm{M}x_{Bj}$, at fixed x_{Bj} the absorption length of the hadronic state is

$$l_h = \frac{1}{\rho(a + b(2Mx_{Bj}/Q^2)^{0.5})} \tag{1.22}$$

here ρ is nuclear density. For high ν,

$$\lim_{\nu\to\infty} l_h = 1/\rho a \tag{1.23}$$

this explains why the cross section for large-A nuclei is weakly dependent on Q^2 at low x_{Bj} (high ν). Shaw also includes high mass mesons, and a parameterization of the hadronic cross section. His results predict the onset of shadowing at $x_{Bj} \cong 0.04$ with no pronounced A-dependence for nuclei in which the nuclear density has saturated. This model has no explanation for the observed enhancement of the cross section above the onset of shadowing.

Other authors have also attempted to incorporate the high mass vector states into the GVD model. Piller and Wiese (30) attempt to account for $q\bar{q}$ states, vector mesons and hadronic multiple scattering. They parameterized the photon using the photon spectral function, $\Pi(\mu^2)$, from $e^+e^- \to$ hadrons data. For the free nucleon they arrive at:

$$F_2^N = \frac{Q^2}{\pi}\int d\mu^2 \frac{\mu^2\Pi(\mu^2)}{(\mu^2+Q^2)}\sigma_N(\mu^2) \tag{1.24}$$

where:

$$\Pi(\mu^2) = \frac{1}{12\pi^2}\frac{\sigma(e^+e^- \to \text{hadrons})}{\sigma(e^+e^- \to \mu^+\mu^-)} \tag{1.25}$$

and

$$\sigma_N \cong \frac{16\text{mbGev}^2}{\mu^2} \tag{1.26}$$

σ_N is the effective cross section of the state and μ^2 is the mass of the $q\overline{q}$ state.

Essentially they assume that the photon interacts hadronically, then use data from electron annihilation experiments to determine the mass distribution of the hadronic fluctuation. The fluctuation interacts with a cross section σ_N. The cross section for large nuclei is determined by considering multiple scattering in the nucleus. The multiple scattering amplitude depends on nuclear density and on how long the photon remains in the hadronic state as it propagates through the nucleus (the coherence length). The increase of the coherence length with decreasing μ^2 is cancelled by the fact that the effective cross section for the low mass states falls off as $1/\mu^2$, this is responsible for a softened Q^2 dependence.

Their results agree remarkable well with NMC data in x_{Bj} and Q^2. They predict shadowing to increase with A, and the Q^2 dependence to be approximately logarithmic. They don't make any predictions on the behaviour of their model in the saturation or enhancement region.

1.2.5 Parton Recombination Models

Another approach relies on parton-parton interactions to explain shadowing. The parton recombination approach hypothesizes that low x_{Bj} partons from different nucleons fuse, which shifts the parton densities to higher x_{Bj}, see figure 1.6.

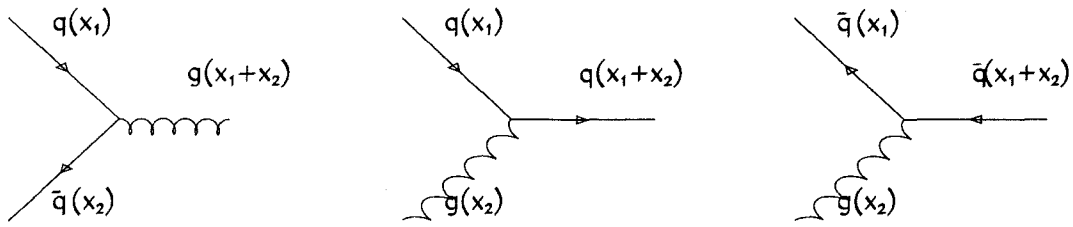

Figure 1.6: Parton Recombination Feynman Diagrams.

Parton model descriptions of shadowing differ from GVD models in that the GVD models attempt to explain shadowing as a property of the photon probe, and in the partonic approach the nuclear medium changes the momentum distribution of the low x_{Bj} $q\overline{q}$ sea.

In a model proposed by Nicolaev and Zahkarov (31) they introduce the partonic model of nuclear shadowing. Their model follows an intuitively simple argument: The uncertainty principle defines how well an object can be localized. For the longitudinal localization of a parton with momentum $x_{Bj}\mathrm{P}_N$ and position Δz

$$(\Delta z)(x_{Bj}\mathrm{P}_N) > 1 \tag{1.27}$$

where P_N is the momentum of the parent nucleon. $\Delta z > 1/x_{Bj}P_N$ is the limit on the localization of the parton. So as x_{Bj} decreases, the parton's position uncertainty grows. When the uncertainty is greater than the separation between nucleons, partons from different nucleons begin to overlap and interact. Nicolaev and Zahkarov define this as the "onset" of shadowing

which occurs at $\Delta z \cong 1$ fermi.

$$x_{Bj} \cong 1/(1\text{Gev fermi}) \cong .1 \tag{1.28}$$

They predict shadowing to "saturate" when the x_{Bj} of a parton is low enough that the parton can only be localized within the nucleus, that is:

$$\Delta z \cong \mathrm{R}_{\mathrm{nucleus}} \;\; \text{at} \;\; x_{Bj} \cong 1/(1\mathrm{GeV})(1.1\mathrm{fm})A^{1/3} \tag{1.29}$$

The important information is that the saturation point is A-dependent and well within the kinematical acceptance of E665. In their model, shadowing results from the redistribution of the momentum of the Dirac sea due to interaction with low x_{Bj} partons from different nucleons. Their model is explicitly x_{Bj} dependent, and predicts no Q^2 dependence. This model also predicts that because momentum is conserved, the depletion of the low x_{Bj} momentum in higher-A nuclei, relative to a free nucleon, will be offset by the enhancement of the momentum at higher x_{Bj}.

The Nicolaev and Zahkarov model has received quite a bit of attention from several theorist working in QCD (32), (33), (34), (35). In particular, Qiu (35) attempts to extend the Altarelli-Parisi parton splitting functions to include terms which allow for interactions between partons from different nucleons. For example consider two low x_{Bj} gluons which fuse to form a higher x_{Bj} gluon and a low x_{Bj} quark which is boosted to higher x_{Bj} by absorbing a gluon from another nucleon, see figure 1.6.

Qiu's treatment of parton recombination is an extension of the evolution equations to include non-linear terms. He claims that recombination terms (sometimes called evolution) are usually subsumed into the distribution function F_2. For free nucleons this is valid, but when the nucleon is in a nuclear medium, the higher order recombination terms distort the F_2 of high-A nuclei. His model recovers the momentum conservation which was assumed in the original Nicolaev and Zahkarov model. Qiu's model also predicts antishadowing which will be more pronounced in the nuclear gluon distribution. The Q^2-dependence is soft, very close to logarithmic. In this model the onset and saturation of shadowing is A-dependent and within the kinematical acceptance of E665. The saturation of shadowing is expected to be proportional to $A^{-1/3}$, the onset of shadowing is expected to be (34):

$$x_c = \frac{1}{mr[1 + 3(2/A^{1/3}) - 3(2/A^{1/3})^2 + (2/A^{1/3})^3]} \tag{1.30}$$

This model also claims to have validity in all regions of x_{Bj}; the predicted x_{Bj} distributions are valid from saturation to values of x_{Bj} above 1.

1.3 Summary

Deep inelastic lepton scattering has proven to be a valuable tool for probing the quark structure of nucleons. Experiments have observed unexpected distortions in the structure functions of bound nucleons, which measure the quark momentum distribution. Several authors have attempted to explain the distortions in terms of the hadronic component of the photon, as was

the case for real photon shadowing. A complementary approach attempts to explain shadowing with QCD inspired parton fusion models. Distinguishing between these two explanations will be important in interpreting the low x_{Bj} behavior of structure functions.

2. EXPERIMENTAL APPARATUS

2.1 General Overview

The data on which this thesis is based were obtained during the fixed target run in the spring and summer of 1990 at the Fermi National Accelerator in Batavia, Illinois. The experiment, number 665 (E665), used a muon spectrometer located in the New Muon Laboratory located approximately 1.1 km tangential to the Fermilab Tevatron ring, which provided the world's highest energy muon beam. The E665 coordinate system was a right handed cartesian coordinate system with the $\hat{X}$ direction pointing along the muon beam, $\hat{Y}$ pointed west and $\hat{Z}$ pointed up. Throughout this thesis, detectors will be referred to as being a "Y"("Z") view meaning the detector elements were oriented vertically(horizontally). The spectrometer magnets had their fields oriented parallel to the $\hat{Z}$ direction which provided charged particle deflection in the Y view; therefore the Y view will also be referred to as the "bend" view. E665 consisted of 2 spectrometers, one for measuring the momentum of the incident muon (the beam spectrom-

eter) and one for measuring momentum of the scattered muons and final state hadrons (the forward spectrometer). A 3 meter thick steel wall separated the forward spectrometer tracking chambers from the muon identification system. E665 was also instrumented with several particle identification detectors, only those detectors which are germane to this analysis will be discussed.

The 1990 fixed target run was one of three runs in which E665 has obtained data. The first run was during the 1987 fixed target run, the last was the 1991 fixed target run. Throughout this thesis these data will be referred to as "run87", "run90" and "run91". The E665 apparatus for run87 had as one component a streamer chamber and targets of xenon, hydrogen and deuterium to study A-dependent effects in structure functions and fragmentation. In run90 the streamer chamber was replaced with high resolution drift chambers and introduced a hodoscope and multiwire proportional chamber(MWPC) to improve the analysis of small angle scatters. Run90 data were taken on targets of hydrogen, deuterium, carbon, calcium and lead. The run91 data were taken predominantly on targets of hydrogen and deuterium, with a short calibration run which used of all the run90 targets. Detectors which were new to the 1990 and 1991 runs will be discussed in detail in this chapter.

2.2 The Beam

The Fermilab muon beam was the world's highest energy muon beam. It was a tertiary beam, meaning it was created in three stages. It began as 10^{12}, 800 GeV/c primary protons from the Tevatron(per Tevatron spill). Protons were aimed at a 48.5 cm thick beryllium production target. Proton-beryllium interactions produced pions and kaons as secondaries, along with non-interacting protons. The non-interacting primary proton beam was momentum selected steered into a beam dump. The pions and kaons in the secondary beam were allowed to decay in a 1.1 km focus-defocussing channel(FODO). The FODO was a long tunnel with quadrupole magnets through which the beam passed. The quadrupole magnet fields provided deflection in 2 dimensions, they served to focus the beam in one plane, and defocus in the perpendicular plane. The focus-defocus effect became more pronounced away from the axis of the magnet, therefore charged particles which passed close to the magnet axis experience very little deflection, those off the axis were deflected more. By alternating the focus-defocus planes the net effect was to focus the beam, called "strong focussing".

As the secondary beam passed through the FODO, the pions and kaons decayed into muons and muon neutrinos. By the end of the 1.1 km FODO, the beam was made of muons, pions and kaons. The resulting neutrino flux was low enough to be ignorable. The remaining pions and kaons were cleaned out of the beam by passing it through 11.0 m of beryllium, after which all that remained was the muon beam. The amount of residual pion contamination was less than

4×10^{-6}. The tertiary muon beam passed through a second 420 m FODO before entering the E665 beam spectrometer. Approximately 5% of the secondary beam ended up as muons (37), the number of muons produced from a single primary proton was typically 10^{-6}.

Every muon beam is accompanied by a spray of muons which are outside the phase space of the useable beam; these are referred to as "halo" muons. Halo muons must be removed from the nominal beam in order to avoid confusing these unusable muons with real scattered muons. The second FODO channel was instrumented with several sections of toroidal magnets including 4 sections of MUPIPE, a magnetized steel pipe with a 2.0 T field (37). The toriodal fields provided a radial kick for halo muons outside the bore of the magnet and no defection for the muon beam inside. The muon FODO reduced the halo muon flux to 20-30% of the nominal beam. The final beam momentum spectrum was broad, typically 60 GeV/c, and depending on the trigger, peaked at approximately 475 GeV/c. In figure 2.1, the momentum of a sample of beam muons which satisfy the small angle trigger beam requirement have been plotted.

2.3 The Beam Spectrometer

The muon beam was produced from the in flight decay of the secondary beam which was a line source, rather than a point source of muons. Since it was a line source, and produced from a three body decay, it was typically more difficult to focus and broader in its energy spectrum than a primary beam. For these two reasons, the energy and trajectory of the beam muons

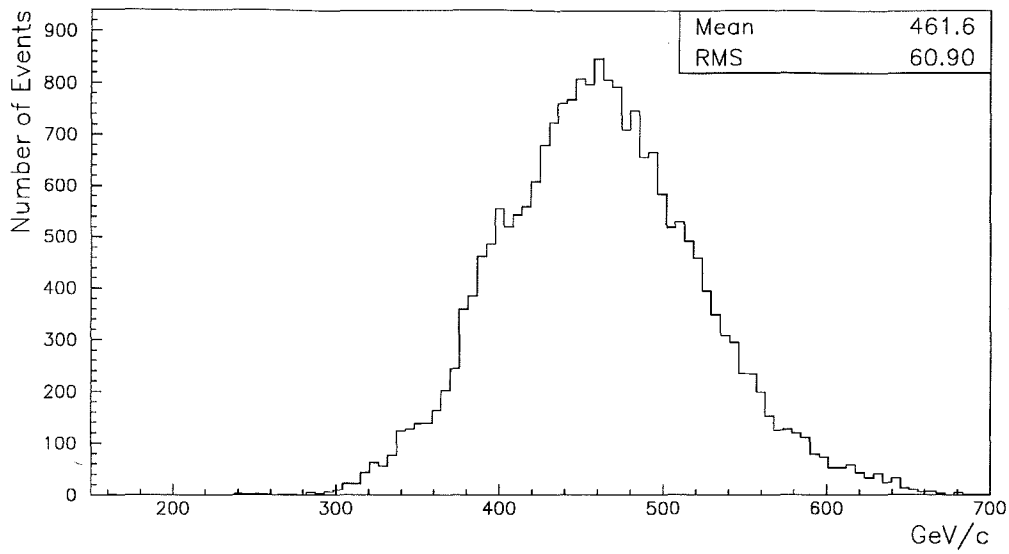

Figure 2.1: The Momentum Distribution of the Fermilab Muon Beam.

were measured before they reached the analysis targets. Beam momentum measurements were performed by the beam spectrometer.

The E665 beam spectrometer was a dual purpose spectrometer. Its purpose was to provide fast signals for triggering as well as measure the energy and trajectory of beam muons. The spectrometer consisted of four beam "stations"; each station contained 6 multiwire proportional chamber planes(PBTs) and at least one scintillation hodoscope plane(SBTs). The MWPCs used were Fermilab Fenker chambers which were designed to operate in the high muon flux generated in the beam region (39), typically $10^6 \mu/sec/\mathrm{mm}^2$ (37). Each set of 6 MWPC planes, called a "package", had their wires oriented differently within the package. The wire orientation and X positions of each station is listed in Table I. The X positions are listed relative to the center

of the forward spectrometer Chicago Cyclotron Magnet(CCM), which defined the origin of the E665 coordinate system. The primed chambers were identical to unprimed chambers but had

TABLE I: Beam Station Wire Planes

Station	X position	Wire planes(looking upstream)
1	- 71 meters	Y,Z,U,Y',Z',V
2	- 44 meters	U,Z,Y,V,Z',Y'
3	- 36 meters	U,Z,Y,Y',Z',V
4	- 15 meters	Y,Z,U,Z',Y',V

their centers staggered, that is, offset by 0.5 mm a wire spacing relative to unprimed chambers in order to increase the resolution of the package. Perpendicular planes, Y and Z, contained 128 gold plated tungsten wires, slant planes, U and V, were oriented at angles +30° and -30° relative to the Z axis and contained 64 wires. All planes had wire separations of 1 mm which, when combined with the offset planes, gave an effective wire spacing of 0.5 mm, in the Y and Z views. The upstream and downstream planes were oriented with a 3 mrad bend in the Y view in order to intercept as many of the incident beam muons as possible after the NMRE dipole magnet had deflected them(see figure 2.2).

The analysis magnet, NMRE, provided a momentum kick of 1.515 GeV/c in the Y view. The magnitude of the NMRE kick was determined from a special calibration run which was taken in 1991 (40). The Tevatron transported primary protons of known momentum to the

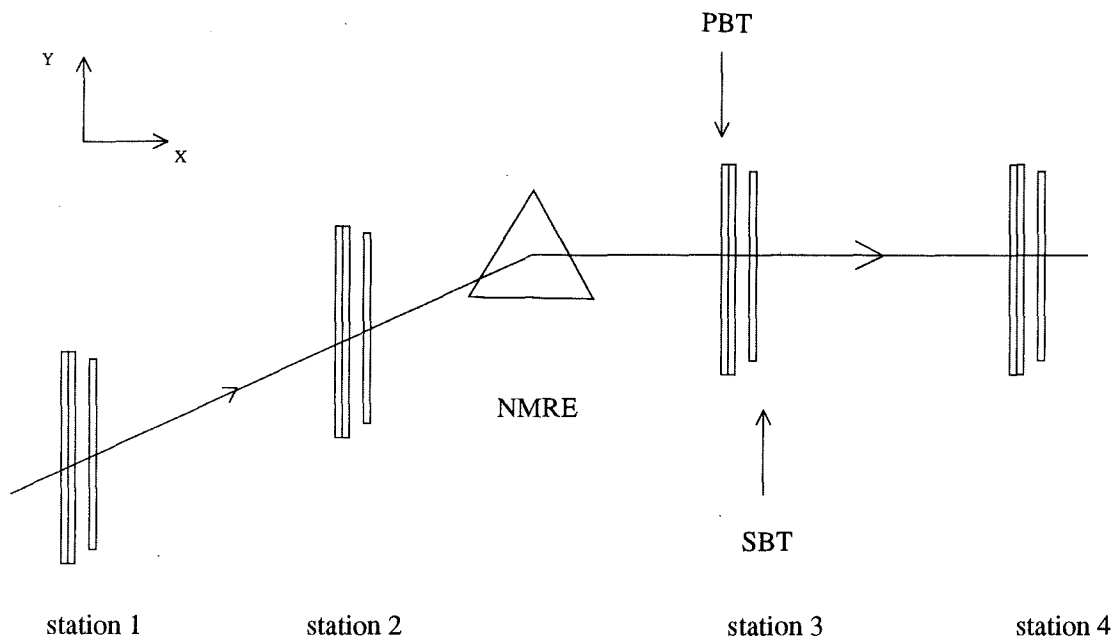

Figure 2.2: The E665 Beam Spectrometer

beam spectrometer, the NMRE kick was determined by comparing the proton momentum as determined by the E665 track fitting program to the momentum as measured by the accelerator. The size of the kick was chosen so that the track fitting program measured a proton momentum equal to the accelerator value (41). The beam spectrometer provided fractional momentum resolution $\delta p/p$, of 0.375%. Figures 2.3 and 2.4 show the spatial distribution of muons in Y and Z at the beam station immediately upstream of the analysis target, station 4 for small angle beam triggers.

Complementary to the PBT's were the beam scintillating hodoscopes, called SBT's. Each beam station was instrumented with one Y and one Z view hodoscope, with the exception of beam station 2 which had no Z view. Each hodoscope had 13 counters. The width of these

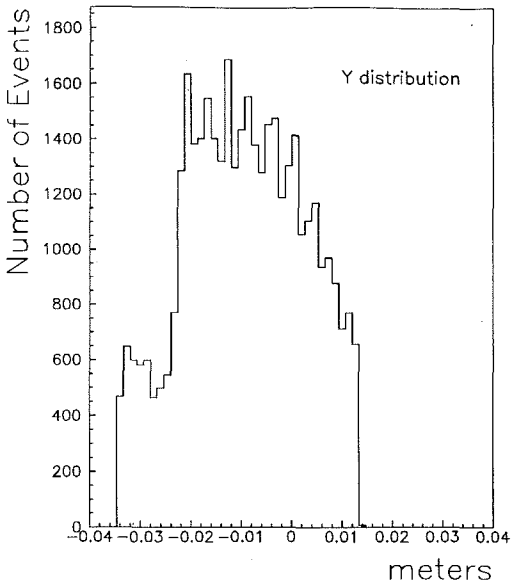

Figure 2.3: Beam Distribution at PBT 4(Y)

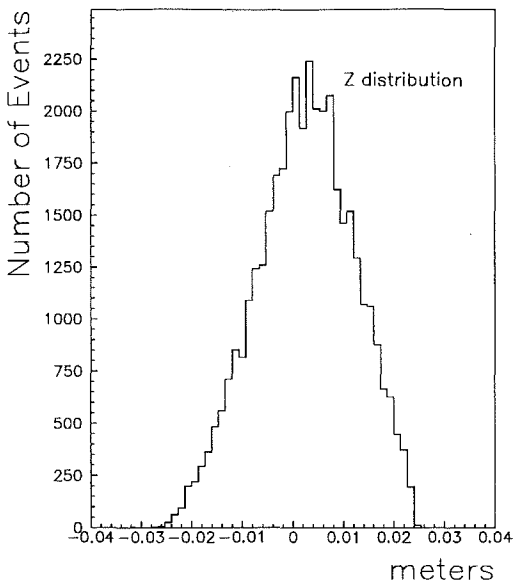

Figure 2.4: Beam Distribution at PBT 4(Z)

counters perpendicular to the beam direction was adjusted so that each saw approximately the same muon flux. Counter widths varied from 0.64 cm for the central counters to 2.54 cm on the edges. The signals from each counter were sent to a passive splitter panel so that the SBT output could be discriminated as well as pulse-height-analysed. As will be discussed in Chapter 3, this splitter panel was the source of spurious triggers.

2.4 Targets

The E665 target assembly was upgraded after the 1987 run. The streamer chamber-target which was used in run87 (37) was replaced with separate target and vertexing assemblies. A new rotating target was designed to specifically address one of the largest sources of systematic

error in previous structure function analyses: time dependence of event reconstruction. In order

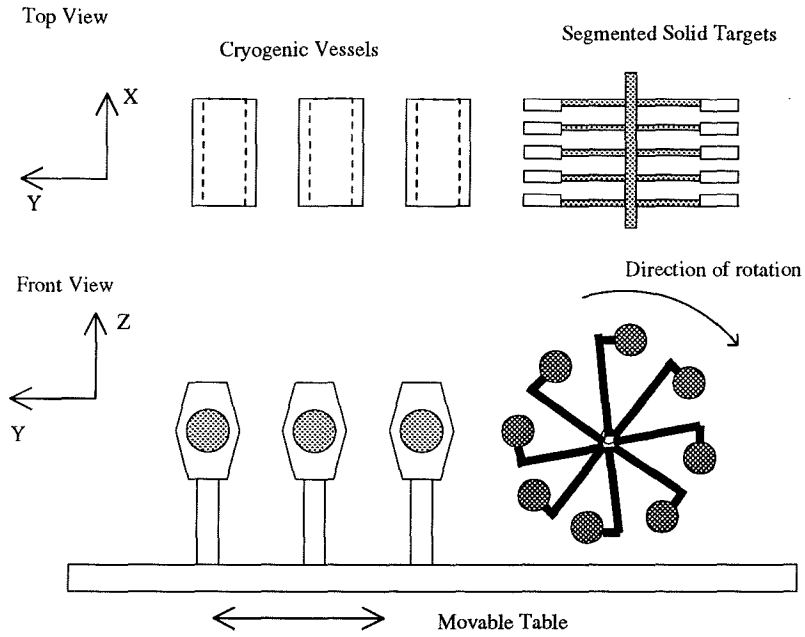

Figure 2.5: The Run90 Movable Target Assembly

to minimize time dependent effects, a movable target table was built to rotate targets in and out of the beam, once per Tevatron cycle(57 seconds). During beam extraction, termed a "spill", the target assembly was stationary. Target rotation was controlled by a computer program which allowed the shift crew to place any target in the beam on command, or run a pre-determined target cycle list, which interchanged the target automatically. Automatic target cycling was the nominal running condition.

In order to measure the A-dependence of shadowing, targets of hydrogen, deuterium, carbon, calcium and lead, with atomic mass numbers of 1, 2, 12, 40 and 208 were used. This analysis is concerned only with data obtained with deuterium, carbon, calcium and lead targets.

The deuterium target was constructed of a 1 meter Rohacell foam insulated flask filled with liquified deuterium. The front(upstream) face of the flask was a mylar window with an aluminum frame for support. An identical flask was constructed for data taking in order to measure the muon interactions which originated in the target flask.

The carbon, calcium and lead targets consisted segmented disks. Disks were held in the beam on a rotating boom made of aluminum. Each target consisted of five disks, disks of a given target were equal thickness. Carbon targets came in two thicknesses, one which consisted of twice the material of the other, see table II. These will be referred to as "thick" carbon and "thin" carbon. Thin and thick carbon were kept distinct from each other, so that during a spill only thin carbon or thick carbon targets were in the beam at one time. Two thickness were used in order to understand the effect of target rescattering.

The calcium target was encased in a thin stainless steel can in order to prevent the calcium from interacting with the atmosphere. Data were also taken with a single empty stainless steel can, identical to the 5 cans which enclosed the calcium targets so that the effect of the stainless steel on the the calcium cross section measurement could be estimated. Similarly, data were taken with an empty target boom with no targets held in it. The empty target data: empty solid holder, empty stainless steel can and evacuated cryogenic flask, were taken as part of the normal target cycling, not in a special run which would require necessary corrections for possible time dependent detector effects.

TABLE II: Target Properties.

Material	Atomic Number	Density/unit area (g/cm^2)	Interaction Lengths	Radiation Lengths	Type
Deuterium	2	$16.109 \pm .277$	.296	0.133	liquid
Thin Carbon	12	15.074 ± 0.0024	.176	0.352	5 solid disks
Thick Carbon	12	29.952 ± 0.005	.349	0.699	5 solid disks
Calcium	40	19.4977 ± 0.0007	.160	1.19	5 solid disks
Lead	208	5.370 ± 0.010	.029	0.853	5 solid disks

In order to identify which target was in the beam for any spill the target type was written to the data tapes, and a message was printed to a computer terminal in the control room. A television camera was trained on the target so that shift crews could visually compare the information written to tape, with what was physically in place. In addition to the target position monitoring, the densities of the cryogenic targets were also recorded by the Fermilab cryogenics group. Target density monitoring involved measuring the vapor pressure of the saturated deuterium vapor. Then, with knowledge of the thermodynamic properties of deuterium, this pressure was translated into the density of the liquid in the target.

In run90 the target assembly was located upstream of the Cern Vertex Magnet(CVM). The E665 forward spectrometer was a double dipole spectrometer built around two dipole magnets which provided complementary momentum kicks(see figure 2.6). The fields were adjusted so as to focus unscattered muons at an X position which corresponded to the first plane of muon

identification chambers, independent of the muon momentum. Prior to the 1990 run, the target was located inside the CVM field in order to observe track curvature within the streamer chamber. In 1987, when the target was located inside the field, the focussing condition was not perfect. This resulted in the trigger accepting muons which scattered with values of Q^2 down to 0.01 GeV^2 (8). Run90 data was limited to $Q^2 \geq 0.1\text{GeV}^2$

2.5 Forward Spectrometer

A second spectrometer located downstream of the targets measured the trajectory and energy of the scattered muon and the tracks of the produced hadrons. It was built around two superconducting magnets. The most upstream magnet, the CERN Vertex Magnet (CVM) was located immediately downstream of the target with its center at an X position of -10.5 meters relative to the center of the second magnet, the Chicago Cyclotron Magnet (CCM). The fields in these two magnets were opposite in direction and adjusted so that scattered muons would be focused at a point at the back of the hadron absorber, independent of the energy of the track, thus allowing the trigger to select the Q^2 of scattered muons. The forward spectrometer provided fractional momentum resolution, δP/P, of better than 5%.

Tracks were reconstructed in a series of proportional and drift chambers. Downstream of the CVM was a six plane proportional chamber, PCV, which contained 6 wire planes of Y, U(+45°), U'(+18.5°), V(-18.5°), V'(-45°) and Y orientations. The PCV chambers had 2 mm wire spacing

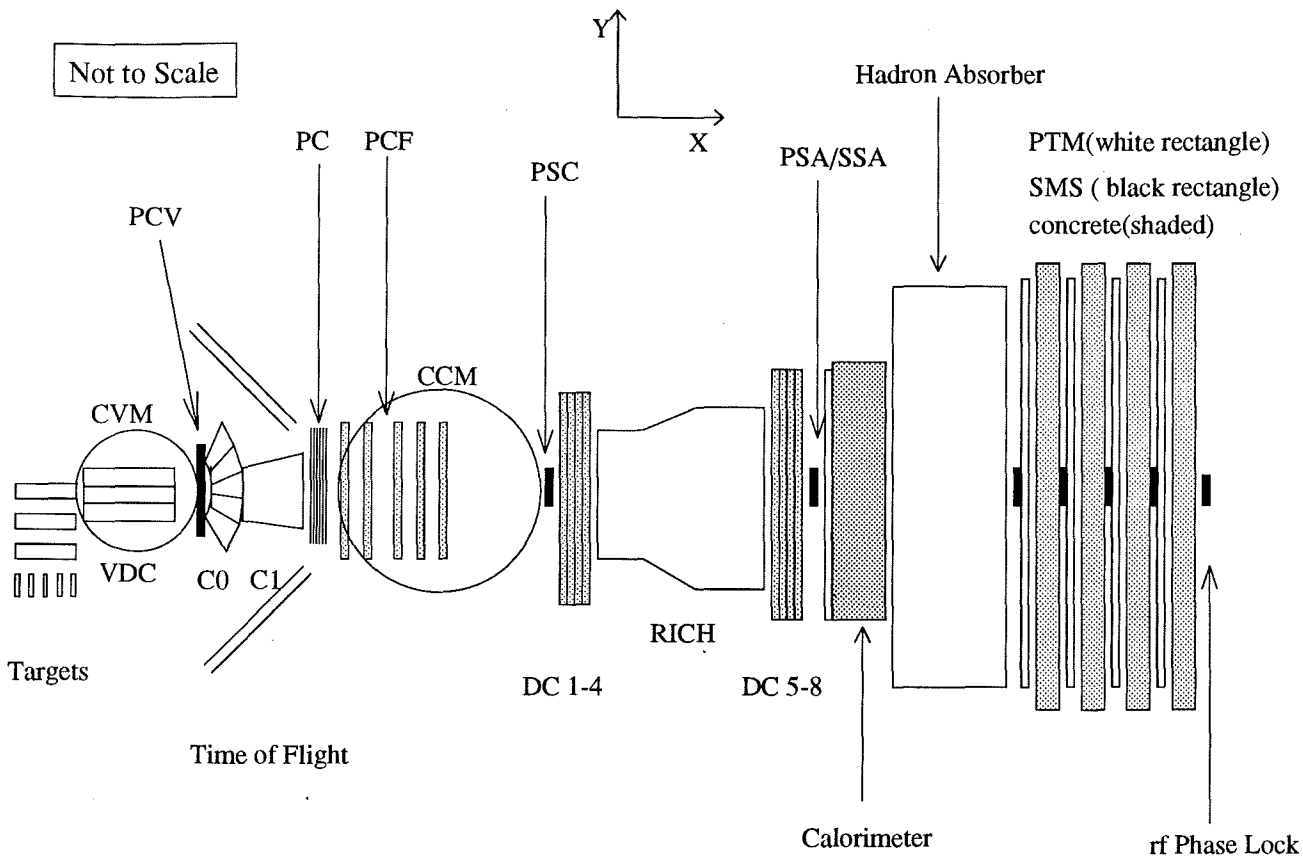

Figure 2.6: Muon Lab Floor Plan

with an aperture of 2.8(Y) meters by 1.0(Z) meter. Downstream of the PCVs were the PC chambers. The PCs were 3 packages of 4 planes each. Each package contained a Y,Z, U(+28°) and V(-28°) wire plane. The PCs had 3 mm wire spacing and a 2 meter by 2 meter aperture. Inside the CCM field 15 planes of chambers, the PCFs were used to measure the curvature of charged tracks. The PCFs were split into 5 sets of 3 chambers with U(+15°), V(-15°) and Z orientations. PCFs had wire spacing of 2 mm and covered a 2 meter by 1 meter aperture.

Downstream of the CCM magnet were two sets of 4 large aperture drift chambers(DC) which were used to reconstruct tracks which emerged from the interaction vertex at large angles. The

first set of drift chambers was located at the downstream edge of the CCM. The active area of these four chambers was 2 meters by 2 meters (42). Each chamber had two planes of wires offset by half a wire spacing, so there were effectively 4 sets of 2 wire planes, Z, Z', U, U', V, V', Z and Z'. The slant planes, U and V contained wires of slopes +5.758° and -5.785° to the vertical, respectively. The Z(horizontal) chambers were split vertically by a G10 septum. The two halves of the Z chambers were read out separately in order to distinguish multiple tracks which shared a common horizontal elevation. The second set of drift chambers, DC 5-8 were located approximately 8 meters farther downstream behind a ring imaging Cherenkov counter. These were a larger copy of DC 1-4, having an active area of 2 meters in Z by 6 meters in Y. All the drift chambers were intentionally deadened in the beam region in order to make them insensitive the the high particle flux associated with the beam.

In order to cover the beam region where the drift chambers were deadened, two high resolution MWPCs were used. Upstream of DC1 was the PSC chamber. The PSC was needed to cover only the beam region therefore had a small active area which was roughly circular with a total active area of 172 cm^2 (43). Each PSC plane had 144 sense wires which were separated by 1.016 mm. A total of 8 PSC planes, each rotated with respect to the next by 45 degrees, provided spatial resolution of approximately 145 μm. Downstream of the drift chambers was a set of eight chambers of eight Fermilab Fenker chambers, identical to those used in the beam spectrometer. The downstream beam region chamber (PSA) had views of Y, Y', Z, Z' similar

to the beam stations. Rather than use slant plane chambers which contained only 64 wires, the PSA used a 128 wire, Y-Z package, rotated by 45° as slant planes, for a total of 4 Y-Z planes and 4 slant planes.

Mounted to the back of the PSA was a hodoscope which did not exist during run87 data taking period(see figure 2.7). Studies of the 1987 version of the small angle trigger(SAT) showed that a large number of events which caused the SAT to fire were due to muons unscattered in the target which underwent large deflections(scatters)in the 3 meter hadron absorber. In order to improve the triggering efficiency, the small angle scintillator(SSA) was built. The SSA provided a triggering plane in front of the steel to remove "steel scatters" and muons which had decayed in the forward spectrometer from the data. The SSA was a two plane hodoscope, Y and Z views which were bevelled in order to provide a .254 mm overlap (see figure 2.8). Unlike the beam hodoscopes which were actually 2 overlapping planes of scintillators, the SSA counters were beveled and laid in a single plane, with the idea that the beveling of the counters would provide enough overlap to completely cover the beam region without cracks.

Both views contained 12 counters which were 132 mm long, 11 mm wide and 12.7 mm thick (50). Each SSA counter was wrapped in aluminum foil(18 microns), leaving one surface exposed. The exposed edge was coupled via an air gap to a fiber optic light guide(see figure 2.9). SSA counters were mounted in a light tight box made of phenolic. The SSA box was constructed with grooves which allowed the fiber optic cables to be epoxied into the box. The

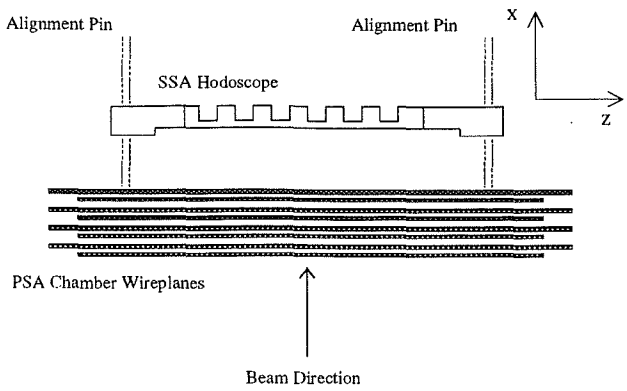

Figure 2.7: PSA-SSA Orientation

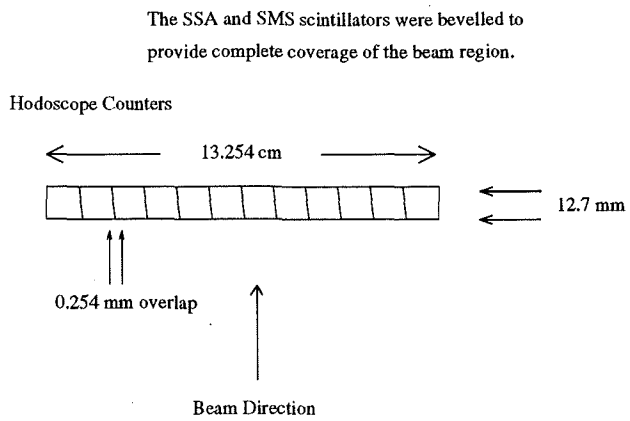

Figure 2.8: SSA Hodoscope Counters

groove arrangement required the SSA counters to be read out in alternating direction. Counters 0,2,4,6 etc were read out from one side of the box and 1,3,5 etc were read out from the other. Because the SSA hodoscope was located directly in front of an electromagnetic calorimeter, it was desirable to minimize the amount of material used in the SSA. The fiber optic light guides were used to transport light from the SSA hodoscope to photomultiplier tubes which were mounted outside the calorimeter active area (see figure 2.9). The SSA fiber optic cables were made of either SK-20 or SK-40 Mitsubishi plastic optical fiber. The SK-40 fibers were 1 mm in diameter compared to 0.5 mm diameter SK-20 fibers. The fiber optic cable lengths varied, depending how the ends were cut during construction and ranged from 1.78 meters to 1.82 meters. The scintillator end of the light guides was 12.7 mm by 12.7 mm square which matched the SSA scintillator. The tube ends were held in a cyndrical lucite sleeve which fit snugly into a μ-metal shield and served to hold a circular cross section of fibers on the phototube face. The photomultiplier tubes were Hamamatsu types R3082 and R1398. Bench tests of the fiber optics and hodoscope estimated efficiency of $> 99\%$ for the SSA (50). The SSA introduced

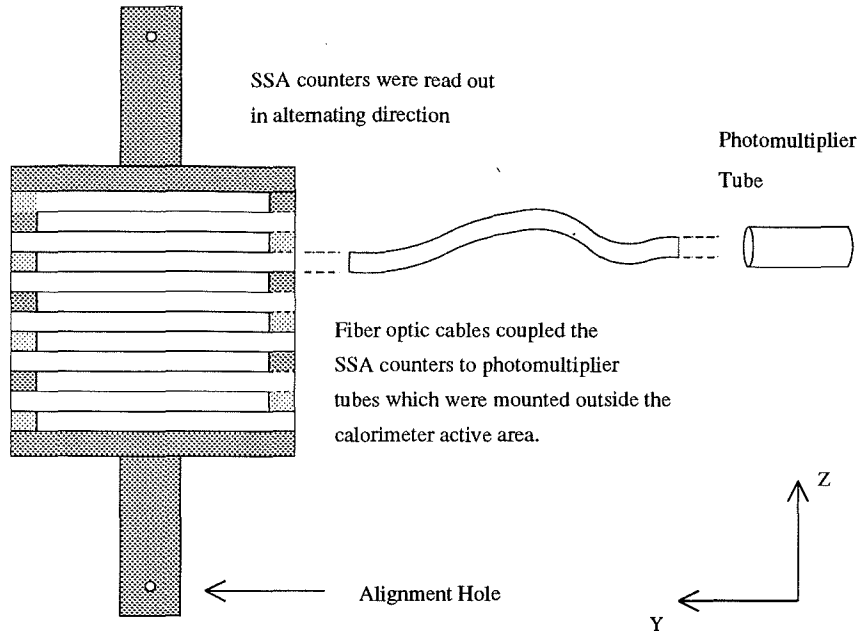

Figure 2.9: SSA Scintillator and Fiber Optics Arrangement

0.62 radiation lengths of material 0.81 meters in front of the calorimeter, with dimensions listed above, centered on the beam.

Also new to the spectrometer in run90 were the vertex drift chambers (VDC). The VDCs were high resolution drift chambers which achieved 300 μm resolution. These gave E665 acceptance for hadron tracks which emerged from the fragmentation process in the center of momentum backward hemisphere. These were low energy tracks, with momenta as low as 2.5 GeV/c (51). The VDCs were built in three types of chambers: wide angle chambers(VCA), beam chambers(VCB) and Z chambers(VCZ). VCA and VCB chambers came in U(+72.5 mr), V(-72.5 mr) and Z views. VCAs were use to measure tracks which emerged at large angles or had large curvature. The VCA's were made of 14 cells of 73 mm width which gave a total active area of 1.02

TABLE III: SSA Hodoscope Components

Counter	Tube Type	Cable Length(m)	Fiber Type	No. of Fibers	Counter	Tube Type	Cable Length(m)	Fiber Type	No. of Fibers
Z0	R3082	1.80	SK20	400	Y0	R3082	1.80	SK20	404
Z1	R1398	1.80	SK20	401	Y1	R3082	1.80	SK40	121
Z2	R3082	1.81	SK20	402	Y2	R1398	1.78	SK40	120
Z3	R1398	1.78	SK20	402	Y3	R3082	1.80	SK40	120
Z4	R1398	1.80	SK20	402	Y4	R3082	1.81	SK40	120
Z5	R3082	1.78	SK20	403	Y5	R3082	1.82	SK40	120
Z6	R3082	1.80	SK20	403	Y6	R3082	1.80	SK40	120
Z7	R1398	1.80	SK20	401	Y7	R3082	1.80	SK40	120
Z8	R3082	1.81	SK20	401	Y8	R1398	1.80	SK40	120
Z9	R1398	1.78	SK20	402	Y9	R3082	1.81	SK40	120
Z10	R3082	1.80	SK20	399	Y10	R3082	1.80	SK40	120
Z11	R3082	1.78	SK20	402	Y11	R3082	1.80	SK40	120

meters. The wire spacing of the VCAs was 9.53 mm between sense wires, they were deadened in the beam region. The chambers which covered the VCA beam region were the VCBs. VCBs had 16 12.7 mm cells which gave a 20 cm active area, with 9.53 mm wire spacing. The Z chambers had no dead region, instead Z chambers had a 10 cm central region which had 8 half inch cells with 9.53 mm wire spacing and an outer region with 12.7 mm wire spacing in 0.55 meter outer active area. The VDC's were placed inside the CVM's 1.5 Telsa magnetic field and were arranged along the beam direction as: VCB(U),VCB(V), VCZ(Z),VCA(U),VCA(V),VCZ(Z), VCB(U),VCZ(Z),VCA(V),VCA(U),VCZ(Z),VCB(V),VCB(U).

2.6 Electromagnetic Calorimeter

Downstream of the tracking chambers was a gas sampling electromagnetic calorimeter. The calorimeter was originally intended for measuring low energy photons which were produced from the decay of π^0's (44). It has also proved useful in identifying high energy photons resulting from muon bremsstrahlung and electrons from elastic muon electron scatters (8), (19).

The calorimeter was made of 20 0.5 cm thick sheets of lead interleaved with proportional chambers. Each sheet of lead was glued to a plate of aluminum(0.2 cm), which provided structural support, the total thickness of lead and aluminum constituted approximately one radiation length, X_0, and 0.5 % of a nuclear interaction length (45), for a total of 20 radiation lengths and 10% of an interaction length. Since the number of nuclear interaction lengths was non-zero, it was not uncommon for hadrons to produce a signal in the calorimeter, but the signal produced had very little to do with the energy of the incident hadron. Methods of distinguishing between hadronic and electromagnetic signals will be discussed in Chapter 4.

High energy photons and electrons induced electromagnetic showers in the lead and the proportional chambers measured the size of the shower by collecting the ions created when the low energy electrons in the shower ionized the gas inside the proportional tubes. The walls of the tubes were coated with a thin carbon film which was held at negative high voltage and served as the cathode plane for the tube. The calorimeter wires were anodes which where held

at ground potential. Complementary to the proportional tube read out, was an array of cathode pads. The cathode pads were squares of copper tape placed on the outside of the proportional tubes. These squares, which were glued on the front and back of each tube were connected by thin copper wire and measured the size of the shower by induction. The avalanche of electrons toward the anode wire was a current which induced charge in the copper pads. Cathode pads of a common Y-Z coordinate were passively summed along the beam direction. The 40 plane sum from a set of Y-Z pads was termed a "tower".

Since the calorimeter used gas-filled proportional chambers, the calorimeter response depended on the temperature and pressure of the gas. Changes in gas gain from temperature and pressure changes were calculated and compared with the change in gain as measured in the calorimeter gas gain monitor(GGM) (48). The gas gain monitor was a small proportional chamber instrumented with an Fe^{55} radioactive source. Gas flowed through the GGM before the calorimeter, and pulse height information from the GGM was accumulated and recorded to tape every few spills throughout the run. Comparison revealed that temperature and pressure corrections were insufficient to track changes in gas gain. It was hypothesized that the composition of the gas was changing throughout the run, so the final gas gain correction was a combination of pressure, temperature and GGM pulse height spectra.

The response of the calorimeter was calibrated during special runs in which normal data taking was suspended. During calibration, an electron beam was transported to the muon lab

and swept across the face of calorimeter in order to measure the calorimeter response to electrons of known energy (49). It was found that for electrons of momenta below 80 GeV/c, the response of calorimeter was linear, that is the measured energy was proportional to the the energy of the incident electron. Above 80 GeV/c, the size of the electromagnetic shower produced in the calorimeter became so intense that it distorted the electric field which accelerating charges toward the sense wires. As a result of the temporary degradation of the accelerating field, the response of the calorimeter became non-linear. The energy reported was much less than the energy of the incident particle. This effect is known as "saturation", and will be discussed in greater detail in the analysis section. The non-linearity for high energy photons was not a design flaw. As mentioned previously the calorimeter was intended for identification of low energy photons from the decay of π^0's, which are typically ($> 99\%$) less than 75 GeV (46).

In the energy range where the calorimeter response was linear, the energy resolution of a cluster was related to the energy of the incident electron by (49):

$$\frac{\sigma(\text{Cluster Energy})}{\text{Cluster Energy}} = a + \frac{b}{\sqrt{\text{Electron energy}}} \tag{2.1}$$

where $a = 0$ and $b = 0.38 \pm 0.11$. The resolution was dominated by stochastic fluctuations in the number of particles sampled in the cascade, and therefore scales as the square root of the energy of the shower.

2.7 Muon Identification

In order to determine the kinematics of muon scattering, it is necessary to measure energy and trajectory of both the incident and the scattered muon. In interactions which may contain in excess of 10 final state hadrons, one has to devise a scheme for separating muon tracks from hadrons. E665 exploited the fact that the mean free path for muons in steel is large compared to hadrons. The E665 forward spectrometer had a 3.0 meter thick steel wall between the tracking chambers and the muon identification chambers. Muons penetrated the steel which served to absorb hadrons, (electrons and photons had already been stopped by the calorimeter). Once the muons had emerged from the back of the steel they formed tracks in large aperture proportional chambers, the PTM's. The PTM's had an active aperture of 3.6 x 7.2 meters and were organized in 4 sets of Y-Z stations. Each station contained two planes of 25.4 mm width proportional tubes offset relative to each other by one half cell so as to give an effective wire spacing of 12.7 mm (37). Between each successive PTM station was 0.9 meters of concrete, which suppressed delta rays generated as the muon passed through the steel.

The PTM's were deadened in the beam region. In order to track muons in the dead region 8 hodoscope planes were mounted directly in front of the PTM planes. These hodoscopes, called SMS's served a dual purpose. They were used to track low-Q^2 scattered muons which remained in the nominal beam and they provided fast signals to the small angle trigger processor. Each SMS station(1-4) contained a Y and Z view hodoscope, each hodoscope was segmented into 16

counters which were wrapped in 1 mil thick plastic to eliminate cross talk. The SMS counters were 13.2 mm wide and bevelled to provided an effective overlap of 0.3 mm (37). The active aperture of the SMS hodoscopes was 20 x 20 cm.

Behind the muon identification system, directly in the beam region, was the RF phase-locking detector. Muons which were delivered to the muon lab were synchronized to the accelerator RF. It was advantageous to have the detector electronics synchronized to the same RF. The phase-locking RF system used beam muons which passed through 4 overlapping photoscintillator planes to synchronize a reference RF signal to the phase of the accelerator. The 4 fold coincidence eliminated time jitter and determined the time the phase of the muon to within 1.05 ns (37). The time the muon passed was used to adjust the phase of the reference RF signal. The phase of the reference RF could be tracked at a 300 ps rate. The phase-locked RF was fanned out using electronic logic modules and used to synchronize detector sub systems to the passage of muons.

2.8 Scalers

Two types of scalers were installed in order to measure beam flux. One set of scalers measured the accumulated beam flux during one spill. The other measured the beam flux accumulated between events.

2.8.1 Spill Scalers

At the end of a spill a special "event" was written which contained the information from the end-of-spill scalers. The end-of-spill scalers, sometimes called "spill scalers", were zeroed at the end of the spill and monitored throughout the run by the shift crew in order to validate their contents. Special care was taken to preserve the end-of-spill event through data splitting, in order to cross check beam flux measurements as made with randomly prescaled beam triggers. In this analysis spill scaler results were used primarily to validate other methods of normalizing cross section ratios.

2.8.2 Event Scalers

Complementary to the end of spill scalers were the once-per-event event scalers, called "event scalers". Event scalers were read and written to tape for every event. These scalers were never reset, instead they were allowed to continuously count throughout the entire run. In run87 since the target assembly was static, the accumulated beam flux could be trivially associated with the proper target. In run90 special software was implemented to account for the fact that the target was changed every spill (54).

Unlike the spill scalers, the event scalers were not monitored throughout the run. In run90 there were three undetected errors in the event scaler hardware. The first was that several inputs

to the event scalers were fanned out from a single cable which was found to be inoperable (52). The bad cable was fanning out the signal which counted the muons available to the large angle trigger and did not affect the measurement of the small angle trigger beam(see small angle trigger section).

The second error was more subtle. The scalers used were 24 bit scalers, meaning they overflowed when the value of the scaler reached $2^{24} - 1$. Occasionally a bit was incorrectly set in the electronics of the scaler, resulting in the beam flux counted being unphysically large. The bit set was the 18 bit, and this error had been discovered in run87 analysis of the event scalers but never fixed. There was, however a fix implemented in software to correct these anomalously high scaler values. The "bad bit" affected all the event scalers, including those which counted the small angle trigger beam. Other methods of identifying these bad scaler counts were developed and shown to measure the beam flux with limited accuracy of 15% (53).

The third, more serious error was related to the gating of the event scalers. An electronic signal was generated by the data acquisition system which served to gate the event scalers, that is to electronically turn them off, when the data acquisition was writing an event to tape. During this dead time, since no triggers were live, the scaled beam should not have been recorded for beam flux measurements. The gating of these scalers was found to be incorrect (54), as a result the measured beam flux was a function of the experimental live time. Since the live time depended on how many triggers were written to tape during a spill, and the number of triggers

written depended on the amount of material exposed to the beam, beam flux, as measured by the event scalers, was implicitly biased by the target material. Despite the gating error the event scalers measured beam flux to within 6% (54) which allowed for identification of gross errors in other methods of normalization.

2.9 Triggers

In run90 several experimental triggers existed, of these, three were designed to determine when a muon underwent an inelastic scatter. Other triggers wrote "halo" muon events to tape for alignment of wide angle chambers, randomly prescaled beam events for normalization, and a variety of calibration triggers. This analysis will be concerned with the small angle physics trigger only.

2.9.1 Small Angle Trigger

The Small Angle Trigger, SAT, was a "veto" trigger meaning it determined when a muon did *not* scatter and supressed the writing of these events. There was no positive muon signal required in the trigger elements located downstream of the analysis target. Because Q^2 is related to the scattering angle θ by:

$$Q^2 = 4\mathrm{EE}'\sin^2(\theta/2) \tag{2.2}$$

the ability to trigger on scatters which occurred at small scattering angles was equivalent to triggering on low Q^2 events(see figure 2.10).

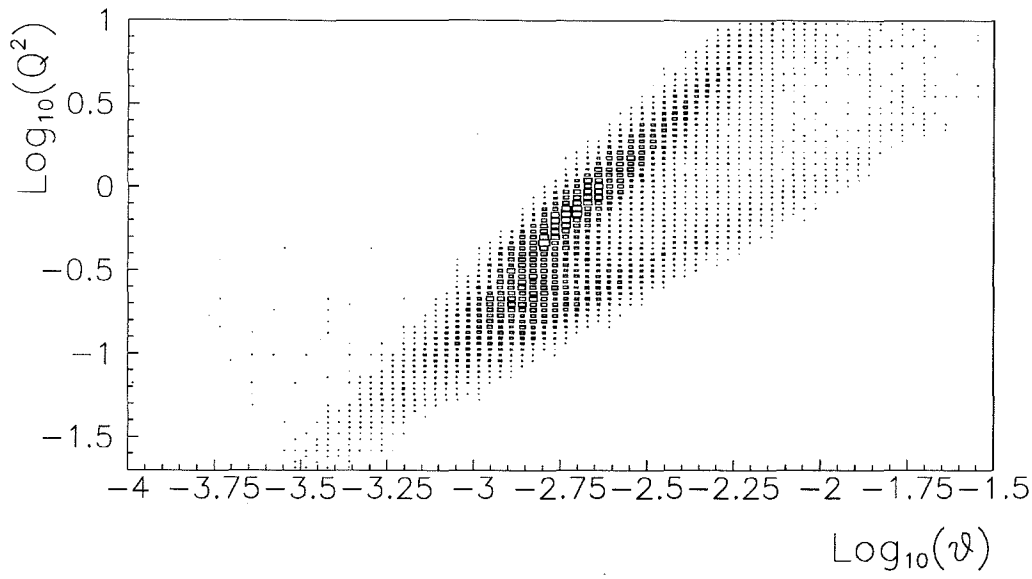

Figure 2.10: $\mathrm{Log}_{10}(Q^2)$ v $\mathrm{Log}_{10}(\theta)$ For Sat Triggers

Typically, at the forward spectrometer focal plane PTM1Y, low Q^2 scatters remained inside the nominal beam region. Figures 2.11 and 2.12 show the distribution of beam and scattered muons at the muon detection chambers.

The overlap of the two distributions is predominantly due to low Q^2 triggers. So that triggering at small scattering angles required the ability to define a veto inside the nominal beam region. The SAT was designed to define a veto aperture which would "float" inside the beam region depending on the trajectory of the beam muon.

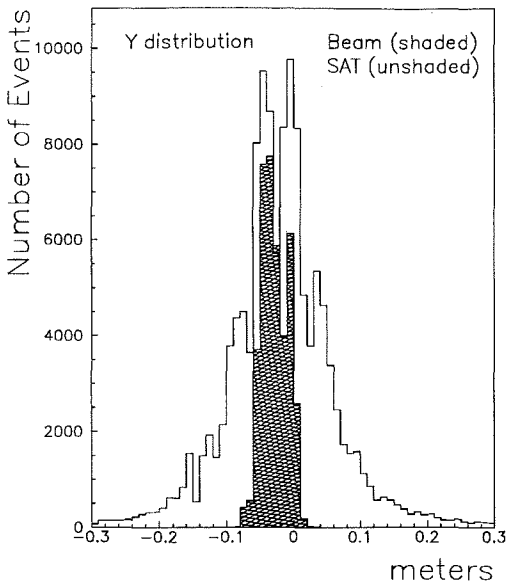

Figure 2.11: Muon Position at PTM1Y(Y)

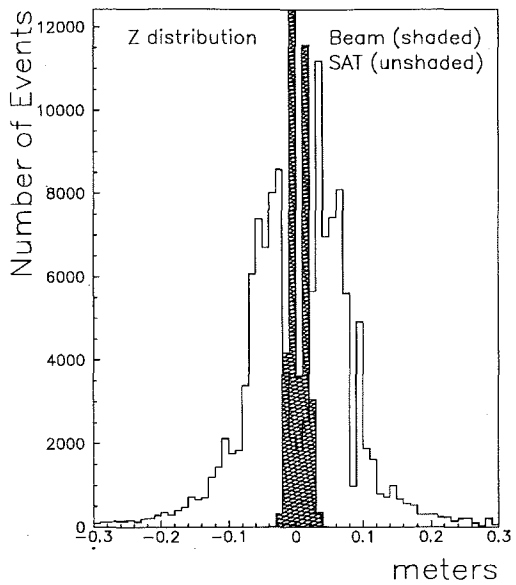

Figure 2.12: Muon Position at PTM1Y(Z)

The SAT used high speed electronics and hodoscopes —-which had time resolution of 1 ns of , so it was possible to re-define the trigger *for every single muon.* Each beam muon had a different trajectory, so to trigger at low Q^2 it was necessary to re-define the veto window on an event by event basis. By allowing the veto window to "float" around inside the beam region, the SAT triggered at angles as low as 0.5 mr, which give the SAT acceptance at values of Q^2 down to 0.1 GeV^2.

Since $x_{Bj} = Q^2/2\mathrm{m}\nu$ the ability to trigger at low values of Q^2 increased E665's ability to collect data at low values of x_{Bj}, including the region where the saturation of shadowing was expected. This kinematic regime was inaccessible to many of the experiments mentioned in Chapter 1. Low Q^2 data is also needed if extrapolations to the region of real photon($Q^2 = 0$)

shadowing are to be made. This region, between $Q^2 = 0$ and high Q^2 will ultimately be important in understanding perturbative QCD effects as they "turn on", that is to say, when the approximations in perturbative QCD become valid.

For a veto to be defined for every beam muon, the trajectory of the muon must be determined to some tolerance in space and time. The SAT used the SBT hodoscopes, which had single bucket time resolution but coarse spatial resolution, in order to define an acceptable beam. The beam signal was also used to define a dynamic veto region in the downstream triggering hodoscopes, SMS and SSA. The SBT's hodoscope's signals were discriminated in Lecroy 4413 discriminators, one output was sent to a second trigger, the large angle trigger(LAT), which was intended to be independent of the SAT. In fact, the LAT and SAT beam definitions became interdependent because one component of the SAT was the "clean" requirement which was formed from the beam signals used in the LAT electronics. The second discriminator output was fed into the SAT trigger matrix modules. The trigger matrix modules used Fujitsu MB7072 random access memory chips(RAM) as fast look up tables to determine if the hodoscope counters through which the muon passed satisfied a pre-determined three hit combination. The access time of these RAMs was 12 ns, as compared to a 18 ns RF bucket structure provided by the accelerator, so that triggering with single bucket resolution was possible.

The trigger matrix modules RAMs were down-loaded with acceptable trigger solutions. Trigger solutions were represented in a three dimensional space called a "trigger matrix". A trigger

matrix was a 16 x 16 x 16 array, each dimension of the array corresponded to a different hodoscope plane and each element to a hodoscope counter. The SAT used 6 of the 7 SBT hodoscopes, 2 SSA hodoscopes and 4 of the SMS hodoscopes as inputs; these planes will be referred to as "trigger planes".

The trigger matrix modules used the hits in 2 hodoscope planes to access the information stored in the trigger matrix module RAM. The RAM contents were bit masks of acceptable hits in the third hodoscope plane. Next the RAM contents were compared to the hodoscope hits caused by the passing muon in the third plane. If the RAM contents and trigger plane hits agreed, the logical signal "1" was sent to a second layer of trigger electronics.

For example, the trigger matrix which was used to determine if the beam condition was met in the Y view was called BY, and used trigger planes SBT2Y, SBT3Y and SBT4Y as its dimensions: $BY(i,j,k) \rightarrow BY(SBT2Y, SBT3Y, SBT4Y)$. Each element within the array corresponded to an SBT counter. For example, a beam trajectory which passed through the 8th counter,"i", in SBT2Y the 6th counter,"j", in SBT3Y and the 5th counter,"k", in SBT4Y, corresponded to the trigger matrix element BY(8,6,5). If that beam was defined as an acceptable trigger solution the element BY(8,6,5) was set to 1, otherwise 0, and loaded into the trigger electronics RAM.

The patterns which were used to define trigger matrices were determined offline, using a Monte Carlo simulation of the experiment. Data taken with a trigger which randomly prescaled

all beam muons were used to simulate the beam. The intention was to use a sample of beam which was as unbiased as possible. A subset of random beams was selected as the nominal SAT beam, trajectories which existed at large angles or passed through the large (1") SBT counters were removed from the SAT beam definition. Approximately 70% of the raw muon beam satisfied the SAT beam requirement in run90 as compared with 17% in run87.

Once the beam distribution was chosen it was used as input to E665 Monte Carlo program. The Q^2 and ν of the scattered muon was used to define the kinematic region which was desirable for analysis; the remaining sample was defined as "beam". The trajectories of all muons in the forward spectrometer were determined at the trigger veto planes, SSAY, SSAZ and SMS planes 1 and 2 in both the Y and Z views. Depending on the position and slope of the tracks at the veto planes, a veto window was defined. A veto window was an aperture into which an unscattered muon would pass. The veto window was projected onto the veto plane and the counters which overlapped with the veto window were used to make the trigger veto matrices, one per veto plane. Since the initial muon trajectory was needed to determine where the muon would intercept a veto plane, veto matrices had SBT planes as 2 of their dimensions. A veto window was typically 4-5 counters wide which corresponds to approximately 5-6.3 cm in the SMS's. In order to increase vetoing efficiency, SMS veto planes were combined to form a single trigger plane. An SMS trigger plane was the logical "or" of two hodoscope planes in the same view, so for example, the SMS Y view vetoed muons based on its position at both SMS1Y and

SMS2Y. The number of counters in beam matrices and the size of the veto windows are listed in table IV.

TABLE IV: Small Angle Trigger Matrix Hardware Map.

Trigger Matrix	Description	Trigger Planes	Counters - Veto Width
BY	Beam - bend view	SBT3Y,SBT4Y,SBT2Y	8, 8, 7
BZ	Beam - non-bend view	SBT1Z,SBT4Z,SBT3Z	9, 13, 8
VY	SMS veto bend view	SBT3Y,SBT4Y,SMS(1Y+2Y)	4-5 counters
VZ	SMS veto non-bend view	SBT1Z,SBT4Z,SMS(1Z+2Z)	4-5 counters
AY	Upstream veto bend view	SBT3Y,SBT4Y,SSA1Y	4-5 counters
AZ	Upstream veto non-bend view	SBT1Z,SBT4Z,SSA1Z	4-5 counters

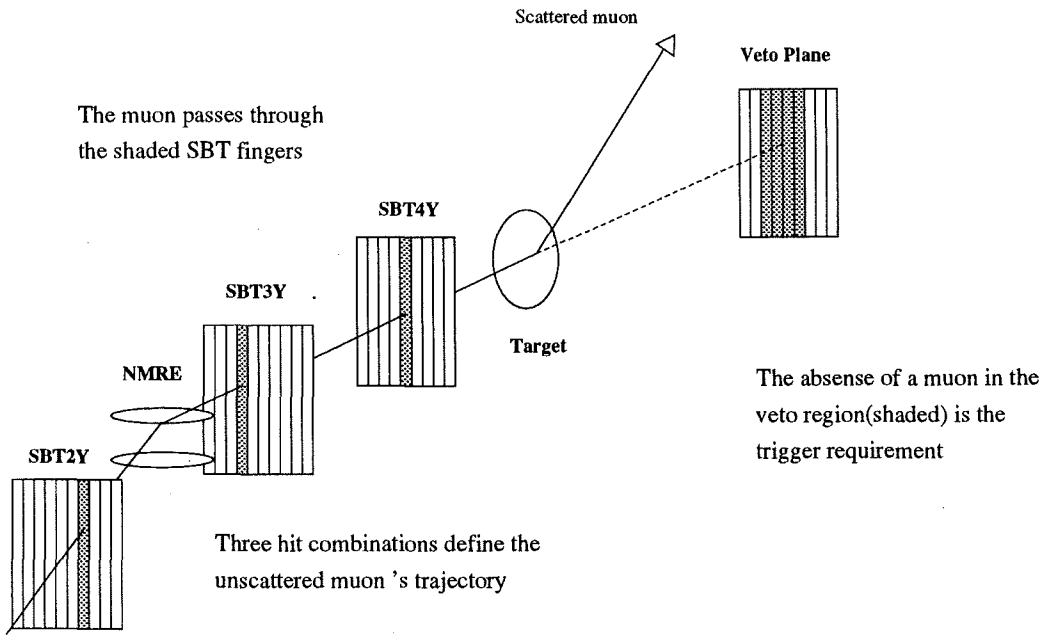

Figure 2.13: Schematic Representation of the SAT Trigger.

Once the array of matrix solutions was determined(BY,BZ etc.) these solutions were fed into Lecroy 2365 programmable octal logic modules. The 2365s had the ability to form logical OR's and NOR's and were used to determine the SAT solutions(see equations 2.5,2.6,2.7). Two such modules were used in the SAT trigger electronics, one located at the end of the beam spectrometer, which determined if the SAT beam requirement was satisfied, and one located on top of the hadron absorber which formed the final trigger configurations. The beam solution as well as beam hodoscope hit patterns were transported to several racks of electronics located on top of the steel, via high speed cables, in order to form the final trigger signals.

One of these modules was incorrectly programmed during run90. The datafiles which were used to program the 2365's were stored on a PDP-11 computer which suffered a disk failure near the beginning of the run. In order to recover from the crash, an older backup of the disk was used to restore the 2365 program. Unfortunately the version which was restored had been altered between the last backup and the disk failure. As a result one of the SAT monitor triggers, the SATPS, was improperly encoded in run90. The SAT and RSAT triggers were completely unaffected by the error.

This mistake was rectified by installing all the run90 targets for a short period of time in the 1991 run. The run91 data were used to study the effect of having a trigger veto element("AZ") upstream of the hadron absorber. The version of the trigger in equation 2.7 is the version which was intended to be used, that is, the run91 version of SATPS.

To summarize, the SAT used a Monte Carlo simulation of the detector to determine where an unscattered muon would end up in the forward spectrometer. An unscattered muon's position was approximated by a 5.0-6.3 cm window. The position of the window was turned into a binary representation which was loaded into some high speed electronics. When a muon passed through the triggering hodoscopes, the electronics regurgitated its approximate trajectory and compared it with the hits registered in the veto trigger planes. If the muon left hits inside the pre-determined window, the event was not written to tape.

2.9.2 The SAT "Clean" Signals: Cluster and No Neighbor

The Cluster Module

Now that the SAT is understood at a very basic level I would like to discuss two components of the trigger that were needed in order to refine, or "clean up" the data which were written to tape. The first was anticipated, it was an electronic signal that was generated whenever an RF bucket was occupied by more than one muon. This bit of electronics searched the beam hodoscope hits from a given bucket and determined if, within a trigger plane, the hit patterns were consistent with a single muon passing through the beam spectrometer. It required single hits in a trigger plane, or 2 hits only if the 2 hits were generated in adjacent hodoscope counters which would occur if the muon passed through the overlap region of two counters. The "cluster module" as it was called used a 16 bit programmable logic unit which was strobed with the

RF and generated a signal which would veto multiple beam trigger signals. The cluster signal was formed independently in the Y and Z views. In the Y view the cluster requirement(CY) was satisfied if a single cluster existed in the trigger planes SBT3Y and SBT4Y. In the Z view SBT1Z and SBT4Z formed CZ.

No Neighbor

The second component was introduced in the trigger because, while the hodoscopes should have been able to re-fire within the pre-described 18 ns time window, it was discovered that the photomultiplier bases which were used to amplify the output of the SMS hodoscope would occasionally "sag". Tube sagging was caused when an unusually large amount of charge was generated inside a photomultiplier tube, and, as a result, the acceleration field between the dynodes became distorted and the drift time inside the tube became large. The result was that a veto counter which sagged was unable to re-fire if a muon passed through it in the next RF bucket. The fix which was devised in order to remove this background was to build a circuit that would identify an RF bucket which had a muon immediately preceding it. Effectively this circuit set an upper limit on the instantaneous beam intensity which allowed the SMS photomultiplier tubes to recover between vetoes. If an RF bucket had a muon in the preceding(neighboring) bucket, the "No Neighbor"(NN) signal would veto that event. In the final configuration the NN determined when a muon passed through the beam spectrometer and vetoed any beam which came in the next RF bucket. Since the SAT used a restricted beam definition, the SAT beam

signal could not be used to define a beam in the preceding bucket. Instead, each SBT plane was logically OR-ed in a Lecroy 4564 logic module, if any counter was hit in plane "I" then the logical level for plane "I" was set to 1 otherwise zero. These ORs were used to form the NN beam signal which was defined as:

$$\mathrm{NN_{beam}} = (\mathrm{SBT1Z} + \mathrm{SBT3Z} + \mathrm{SBT4Z}) \bullet (\mathrm{SBT1Y} + \mathrm{SBT2Y}) \bullet (\mathrm{SBT3Y} + \mathrm{SBT4Y}) \tag{2.3}$$

$$\mathrm{NN_{beam}} = (\Sigma\mathrm{SBTZ}) \bullet (\Sigma\mathrm{SBTY}) \tag{2.4}$$

The NN beam signal was delayed by 1 RF bucket and required to be in anti-coincidence with the NN beam in the preceeding RF bucket (see figure 2.14).

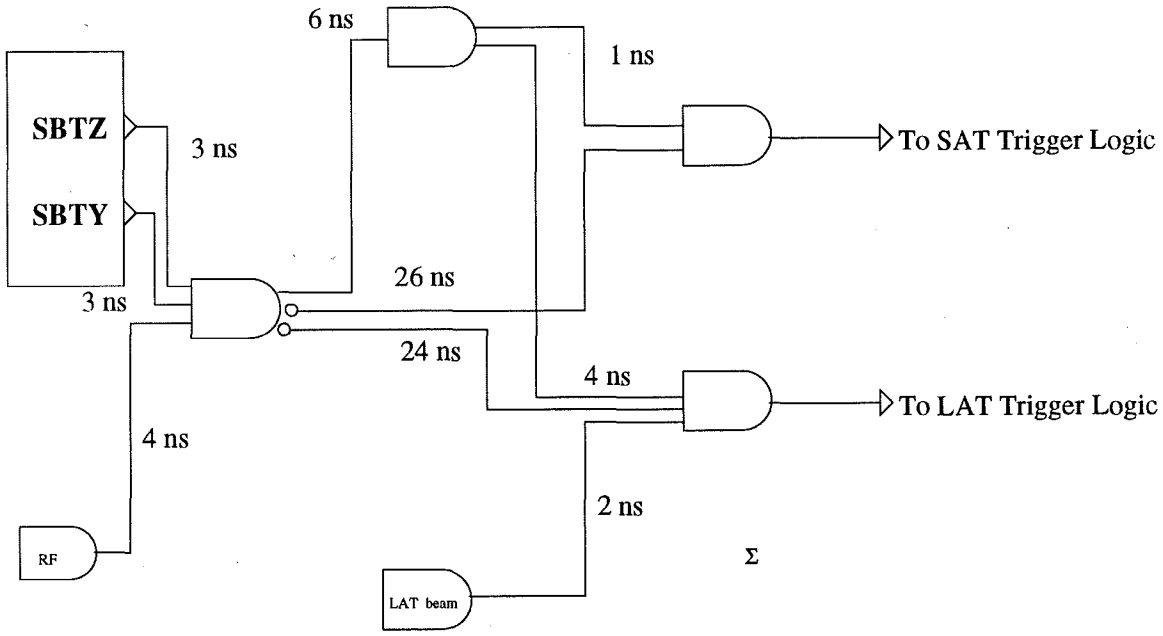

Figure 2.14: SAT No Neighbor Logic Diagram

The Final SAT Definition

In the final configuration of the SAT, SMS veto signals in both views were used but only the upstream AZ was incorporated. The SAT trigger definition was:

$$\mathrm{SAT} \equiv \mathrm{BY} \bullet \mathrm{BZ} \bullet \mathrm{CY} \bullet \mathrm{CZ} \bullet \overline{(\mathrm{VY} \bullet \mathrm{VZ})} \bullet \overline{\mathrm{AZ}} \bullet \mathrm{NN} \tag{2.5}$$

2.9.3 SATPS and RSAT Triggers

The danger with using any method of selecting a sample for scientific analysis is that by selecting a sample, a bias is introduced. This is a particularly important consideration when designing a trigger. In order to understand the data written to tape, one must also look at the data which was *not* written. The small angle trigger was only one of a complement of small angle triggers. Other triggers included: a randomly prescaled beam trigger(RSAT); a trigger which didn't rely on the veto element upstream of the steel, the small angle prescaled trigger(SATPS); and a trigger which used a very tight beam definition and required a positive muon signal in the SMS counters, the small angle limited phase space trigger(SAL). Equations 2.6 and 2.7 show the logical definition of the RSAT and SATPS. Both have as one component a randomly pre-scaled RF signal.

$$\mathrm{RSAT} \equiv \mathrm{BY} \bullet \mathrm{BZ} \bullet \mathrm{CY} \bullet \mathrm{CZ} \bullet \mathrm{NN} \bullet \text{ Randomly Prescaled RF} \tag{2.6}$$

As mentioned above, the triggers were synchronized to the passage of muons by using the

phase locked RF. This allowed E665 to prescale triggers by requireing a coincidence with a prescaled RF signal. In order to get a trigger which was unbiased as possible, events which satisfied the SAT beam definition were prescaled and written to tape. Ideally one would write every beam event to tape and examine each one in order to understand the biases introduced by the trigger, this was completely impossible. Instead a beam was required to coincide with a RF signal which was pre-scaled by roughly $1/2^{18}$. Actually the factor of 2^{18} was adjustable and changed throughout the run. Table IV shows the pre-scale factor as a function of run number. The number of RSAT's written to tape depended not only on the pre-scale factor but also the beam definition, beam intensity and to a smaller extent the percentage of time the experiment was "dead" while the data acquisition wrote an event to tape (dead time). This is the reason that even though at one point the amount of pre-scaling doubled, the number of RSATs written to tape remained roughly constant.

TABLE V: Small Angle Trigger Prescale Factors.

Begin Run	End Run	Prescale Factor	RSAT's Per Spill
12052	12069	2^{17}	30 - 50
12070	12611	2^{18}	30 - 50
12612	13267	2^{19}	10 - 30

The SATPS was implemented in order the measure the effect of having a veto plane in front of the hadron absorber. The SSA veto plane would veto any unscattered muons which scattered

outside of the SMS veto region in the steel. Unfortunately, because the SSA was in front of the steel, which protected the SMS veto from hadrons produced in DIS events, the SSA was subject to "self-vetoes". A self veto could occur when a valid DIS event, which were typically high multiplicity, produced a hadron which hit the SSA veto. Since high multiplicity events occurred at high energy transfers, one would naively expect the self veto effect to occur at high ν or equivalently at low x_{Bj}. Clearly the self veto effect must be understood in order to make any definitive statements on shadowing at low x_{Bj}. The SATPS was pre-scaled by a separate prescaler than the RSAT and the value was set to 1/32. In the 1991 self-veto calibreation run no pre-scaling of the SATPS trigger was implimented.

$$\text{SATPS} \equiv \text{BY} \bullet \text{BZ} \bullet \text{CY} \bullet \text{CZ} \bullet \text{NN} \bullet \overline{(\text{VY} \bullet \text{VZ})} \bullet \text{ Randomly Prescaled RF} \tag{2.7}$$

2.10 Data Acquisition

The data acquisition(DA) system consisted of 3 PDP-11 computers as well as two fastbus crates which were used for reading the calorimeter and VDC sub-events. CAMAC crates were used to provide an interface between detector components and the PDP11s. The PDP's were also used for online monitoring of several detectors. The bulk of the data acquisition was run on a μVax. The DA software was responsible for reading the event from the PDPs and fastbus, verifying the event which was being read was synchronized between the three PDPs and writing the event to tape. In addition to the DA the Vax was also used to run several online monitoring programs.

For example scaler monitoring, and wiremaps, which were inspected by shift crews were run on the Vax.

Data were recorded on 8 mm Exabyte video tapes and approximately one file out of every 100 was immediately run through the full offline reconstruction. The offline reconstruction program used "untuned" calibration and alignment files but nevertheless provide results which could be used in finding hardware errors. For example, the beam spectrometer reconstruction efficiency dropped sharply at one point in the run. The problem was traced to a low voltage power supply which was replaced.

2.11 Summary

The run90 version of the E665 spectrometer used an upgraded version of the run87 experiment. Two spectrometers, a beam spectrometer and double dipole open geometry forward spectrometer were used to determine the energy and scattering angle of scattered muons. Targets of various atomic numbers were rotated into the muon beam in order to minimize time dependent corrections to the data. High resolution vertex chambers and small angle beam chambers were installed to improve vertex resolution and reconstruction of scatters which occurred at small angles. An upgraded version of the small angle trigger accepted approximately 70% of the raw muon beam and triggered on muon which scattered at values of Q^2 as low as 0.1 GeV^2.

3. OFFLINE RECONSTRUCTION

In this chapter the software which was used to create the database for this analysis will be discussed. After data were written to tape, they were converted into a form which was useable by physicists. The digitized detector information needed to be converted into physically meaningful quantities like energy and scattering angles; this was the job of the E665 offline reconstruction program PTMVE. PTMVE stands for Pattern recognition, Track fitting, Muon matching, Vertex finding and Electromagnetic calorimeter. The output of the PTMVE program was stored in a ZEBRA based memory management structure (55). The ZEBRA structure stored logically associated information in "banks" which were identified by 4 letter acronyms. Throughout this thesis these banks will be referring to by their 4 letter bank identifiers. In addition to reconstructing raw data the PTMVE program applied a loose set of cuts to insure that data written out was of high quality.

Since the E665 spectrometer was a multipurpose spectrometer the PTMVE/Data Reduction

code was written with a variety of physics goals in mind. In order to address the issues important to shadowing analysis, a second program called LOX was written to further reduce the data. The output of the LOX program was PAW Ntuples which were used as pseudo-data summary tapes (DST's) for the shadowing analysis.

3.1 Decoding and Translation

The first step in the PTMVE program was decoding the data. Decoding turned packed binary words either into wire hits, or ADC/TDC values. Decoder results were stored as part of the E665 ZEBRA based bank structure as LDEC banks. If an error occurred during decoding or translation, an error code was stored as part of the ZEBRA structure of the event. Decoding errors were not sufficient reason to drop the event from analysis, but did affect the quality of the reconstruction.

Translation converted the wire hits, which were stored in LDEC banks, into the physical position of the hit wire in real space coordinates. Obviously translation relied on knowledge of the physical position of a given detector. The positions of all detectors were determined roughly by survey crews, who measured their positions relative to monuments mounted on the experimental floor. In order to refine the alignment constants, special calibration runs were made. Alignment runs were taken throughout run90 during which normal data taking was suspended. These runs used various analysis magnet configurations in order to project straight

line tracks from one chamber to another for measurement of the orientation of chambers with respect to each other. The results of the alignment runs were stored constants files which were read by the PTMVE program. Translation used wire hits and alignment constants to form the space coordinate of wire hits and stored the results in LCOR banks. The wire positions stored in LCOR banks were used as input to the pattern recognition program.

3.2 Pattern Recognition

The pattern recognition program (PR), grouped wire chambers hits from LCOR banks into patterns which were consistent with charged particle trajectories. The E665 pattern recognition program has been extensively documented elsewhere (56), (44), (57), The following discussion will be limited to those parts of the reconstruction which determined the event kinematics. Pattern recognition used two complementary methods of grouping hits: projection finding and space-point finding. The projection finding algorithm formed lines using the CERNLIB routine PTRACK. The space-point finding algorithm determined the intersection of wires which overlapped in Y and Z. Space-point finding combined wires from non-parallel views and was restricted to chambers which were closely spaced along the beam direction. Pattern recognition was run in three phases: beam, forward spectrometer muon phase and forward spectrometer hadron phase.

3.2.1 Beam Pattern Recognition

The beam phase of pattern recognition used the space-point finding algorithm to form lines in the PBT chambers. First, three hit combinations of non-parallel wires within a six plane PBT package were grouped together to form space-points. Next, two wire combinations were formed from the unused PBT hits. The beam pattern recognition searched for space-point combinations which satisfied the equation of a straight line in the X-Z (non-bend) plane. Separate line segments were formed upstream and downstream of the NMRE analysis magnet. These lines were required to join, in the bend view, at the center of the magnet.

Since the PBT chambers had relatively coarse time resolution, approximately 100 ns, more information was needed in order to determine if the reconstructed track was associated with the muon which caused the trigger to fire. Timing information from the beam scintillating hodoscopes was used to identify beam tracks formed by muons in previous RF buckets. After PBT lines were found, correlations between line projections and beam hodoscope hits were made. If a SBT finger through which the beam passed registered a hit this indicated that the muon track was a candidate for being an "in time" muon. Since it was possible for tracks to overlap, the final requirement to define an "in time" beam was that every SBT finger through which the beam muon had passed recorded a hit. If any SBT finger did not have a hit, the beam was said to be "out of time". Results were saved in LHOD banks.

3.2.2 Forward Spectrometer Muon Phase

The forward spectrometer muon phase of pattern (PR) was run to reconstruct tracks which were most probably associated with the scattered muon. Scattered muons were hypothesised to be higher momentum than hadronic secondaries. Muon phase PR searched for "stiff" lines which pointed in the vicinity of the target. Lines were formed in the large muon identification chambers behind the steel and stored as LPRO banks. Next the drift chambers were searched for track segments which were matched with segments formed in the PC chambers by linking the two with segments found in the PCFs. The formed tracks were further constrained by searching for hits in the PCV chambers. In the small angle region, unmatched PC-PCF lines were projected to the PSC chamber where space-points were used to constrain the line at the downstream edge of the CCM. Finally the PC-PCF-PSC lines were projected into the PSA chamber and linked with space-points there.

3.2.3 Forward Spectrometer Hadron Phase

The hadron phase of the forward spectrometer pattern recognition was analogous to the muon phase, the only difference being that tracks with large curvature were reconstructed. In this phase of PR the requirements on the quality of the reconstructed tracks were "looser" than in the muon phase. Again target pointing was required of these tracks. It should be mentioned that the names "hadron" and "muon" phase did not preclude the scattered muon being identified in

the hadron phase PR. Final determination of which line belonged to the scattered muon was made after a track's momentum had been determined.

3.3 Track Fitting

Track fitting used the tracks created in PR and used a quintic spline fitting routine to determine the track parameters. All tracks were parametrized by 6 numbers, x, y, z, dy/dx, dz/dx and momentum, which completely determine a particle's trajectory through the spectrometer. Along with the tracking parameters, the full error matrix of tracks was stored in the LSTF banks. The track error matrix took into account effects due to multiple scattering in the detector materials (58). Track fitting of beam tracks used the size of the deflection caused by the NMRE magnet to determine the beam momentum. Track curvature in the field of the CCM magnet determined the momentum of forward spectrometer tracks. The error and χ^2 probability of these tracks was used as measure of track quality during this analysis.

3.4 Muon Matching

After the forward spectrometer tracks had been fit, and the momentum of these tracks had been determined, it was the job of the muon matching processor to determine which tracks were muons. The muon match processor matched forward spectrometer tracks with lines in the muon identification chambers, PTMs and the scintillation counters, SMSs. The match processor had

three different modes of operation: multiple-scattering matching, intersection matching and ray trace matching. Multiple-scatter matching was always run and more that 80% of all matched muons were found using this method. Intersection matching searched for those muons which underwent large angle scatters in the steel and thus were missed by the multiple scattering match. Ray trace matching was an attempt to "rescue" tracks which were not fully reconstructed in the forward spectrometer. Ray trace matching was only run if the other attempts at matching had failed.

3.4.1 Multiple Scatter Matching

The muon match processor used as input all forward spectrometer tracks which contained line segments reconstructed downstream of the CCM's magnetic field. These tracks were projected as straight lines to the back of the hadron absorber along with their propagated error matrix. The propagated track error,σ_{forward}, was added in quadrature with the error due to multiple coulomb scattering, $\sigma_{\text{multiple scattering}}$, see equation 3.3. The multiple scattering errors used in equation 3.3 have been assumed to be gaussian distributed. Since lines in the PTM and SMS chambers are constrained by geometry to lie in either the Y or Z view, the multiple scattering error in angle was projected into the Y and Z planes seperately and calculated as

$$\sigma(\text{angle}_{\text{plane}}) = \frac{0.041\text{GeV/c}}{\text{p}}\sqrt{\text{L/L}_{\text{R}}}\left[1 + \frac{1}{9}\log_{10}(\text{L/L}_{\text{R}})\right]. \tag{3.1}$$

Here L/L_R is the number of radiation lengths of scattering material, which for the combination of calorimeter lead and steel is approximately 190. The error in displacement caused by multiple scattering, projected into a plane is related to the angular error by:

$$\sigma(\text{space}) = \frac{L}{\sqrt{3}}\sigma(\text{angle}_{\text{plane}}) \tag{3.2}$$

Lines which were formed in the muon identification chambers, PTM's and SMS's (LPRO lines) were refit to the same X position at the back of the steel as the forward track. These projections were fit in Y and Z separately and a χ^2 was formed for both position and slope:

$$\chi^2 = \frac{(\xi_{\text{forward}} - \xi_{\text{back}})^2}{\sigma^2_{\text{forward}} + \sigma^2_{\text{back}} + \sigma^2_{\text{multiple scattering}}} \tag{3.3}$$

where ξ is either slope or position of the track at the back of the steel and $\sigma_{\text{multiple scattering}}$ is given by 3.1 or 3.2. "Forward" refers to the tracks projected from the front of the steel, LSTF tracks, "back" refers to lines formed in the back of the steel, LPRO lines. The correlation between the error in position and slope was not included in the determination of χ^2s.

The match processor used the χ^2s (equation3.3) to determine the "goodness" of the match. If an a LSTF-LPRO match satisfied an adjustable cut, it was considered a muon candidate. In the run90 analysis, the criterion was:

$$\chi^2(\text{angle}) + \chi^2(\text{displacement}) < 40. \tag{3.4}$$

If an LSTF track had a matched LPRO in both views, it was tagged as being a muon. If more than one LSTF-LPRO combination satisfied the match requirement, the LPRO-LSTF

combination which had the smaller match χ^2 was identified as the muon.

3.4.2 Intersection Match

The intersection match code searched for tracks which intersected in both Y and Z views in the steel, but because they had undergone large scatters fell in the large χ^2 tails of the multiple coulomb scattering distribution. Because the χ^2 cut for an acceptable multiple scattering match was loose, most large angle scatters (>98%) were found by the multiple scatter matching.

3.4.3 Ray Trace Matching

The ray trace match processor was run after the multiple scatter matching had failed to match forward spectrometer tracks which were reconstructed downstream of the CCM field. The ray trace matching attempted to rescue an event which had no identified muon by considering previously ignored forward tracks. Tracks which were reconstructed up to the PCF chamber PCF3V, but had no associated drift chamber hits were used as input. An additional cut was imposed on these tracks which restricted candidates to have a χ^2 probability of fit to be better than 1%. These tracks were traced, using the track momentum and knowledge of the CCM field, through the magnet to the back of the steel. Figure 3.1 compares the ray trace algorithm to the multiple scatter matching. The multiple scatter matching performed a straight line projection of tracks which had been reconstructed downstream of the CCM field, an example is labelled a

"A" figure 3.1. The ray tracing match, track "B", projected tracks which had no corresponding hits downstream of the CCM. Once these tracks were projected, with their associated error

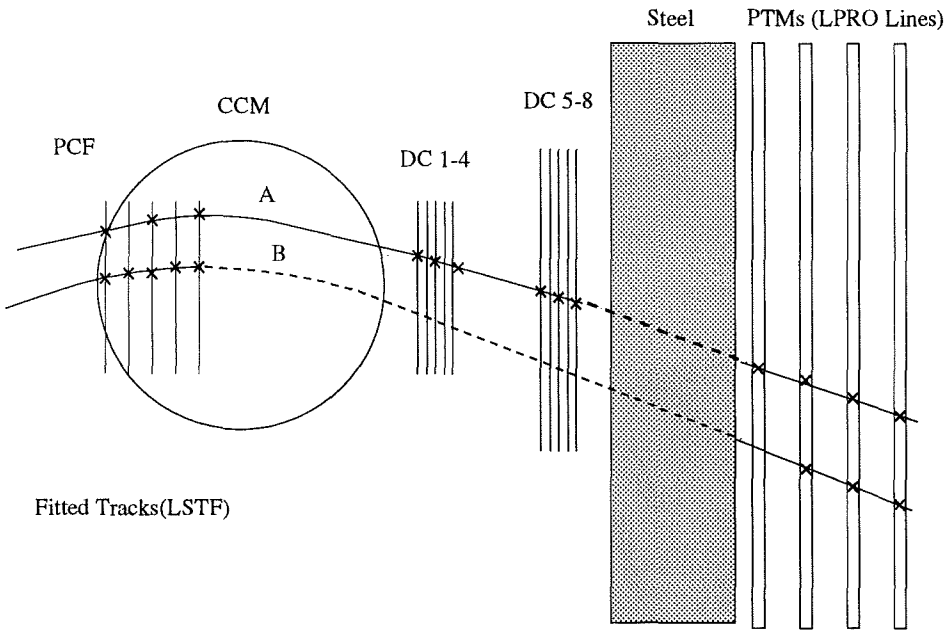

Figure 3.1: Muon Match Schematic

matricies, the algorithm was identical to the multiple scattering match. Approximately 20% of all found muons were found with the ray trace method.

3.5 Vertexing

The vertex processor used beam and identified muon tracks in order to find the interaction vertex, the point at which the muon had scattered. A vertex was defined as the point of closest approach of two tracks, and for muon-muon vertices these were required to be within 5 cm of each other and have a χ^2 probability of better than 0.0001. The vertex processor first formed

the muon-muon vertex, then attempted to attach remaining hadron tracks to the muon-muon vertex by examining the distance to the vertex divided by the error on the track. Once the hadrons were attached, a "primary" vertex was calculated by including all the hadron tracks which were attached to the muon-muon vertex, and the position and χ^2 of the new vertex was reported. Since tracks were not refit or constrained to pass through the vertex, refitting a vertex with additional hadrons did not alter the event kinematics, which were completely determined by the incident and scattered muons. As a final pass the vertex processor attempted to form secondary vertices from hadrons which would have come from the decay of long lived particles such as K°'s. All vertices were stored in LVTX banks. Track information from the incident and scattered muons was used by the vertex processor in order to determine the kinematics of the event: Q^2 ,ν ,$\theta_{scatter}$ and hence x_{Bj}, W^2 and y_{Bj}. For those events which had more than one reconstructed muon, the highest energy muon which was positively charged was defined to be the scattered muon. If no positively charge muons were reconstructed the highest energy negative muon negative muon was used to determine the event kinematics. Kinematic quantities were stored in the event's LEVF bank.

3.6 VDC Pattern Recognition

After the PTMV program had been run, a separate pattern recognition was run for the hits in the high resolution vertex chambers (VDCs). VDC pattern recognition was run in order

to pick up hits which could be used to constrain tracks which had been already been formed in the rest of the forward spectrometer. After tracks had been refit, the vertex processor was rerun. In figure 3.2 vertex resolution before and after the VDC pattern recognition was run is compared. The fractional error and vertex position along the beam direction are shown for the segmented(solid) targets only. Even though the changes introduced in kinematic resolution are not pronounced, the gain in vertex resolution is quite obvious.

3.7 Electromagnetic Calorimeter

The electromagnetic calorimeter analysis was run as a final step in the reconstruction. Calorimeter information was stored in a fastbus buffer which contained run, event and calorimeter ADC information (44). Event decoding of the calorimeter data involved checking run and event information as well as validation of the event by checking various fastbus separator words. Decoded calorimeter ADC values were stored in LDEC banks. Calorimeter LDEC banks were refilled with bitube and pad ADC values which were pedestal-subtracted, and noise-suppressed. Next, calorimeter translation used information in the LDEC banks and applied temperature, pressure, gas composition and electronics calibration corrections to produce LCOR banks. Data in the LCOR banks from bitubes and pad towers were stored separately and reported in units of GeV.

The data stored in the pad tower LCOR banks were used as input to the calorimeter clustering routine which grouped "globs" of energy which were induced by the same electromagnetic

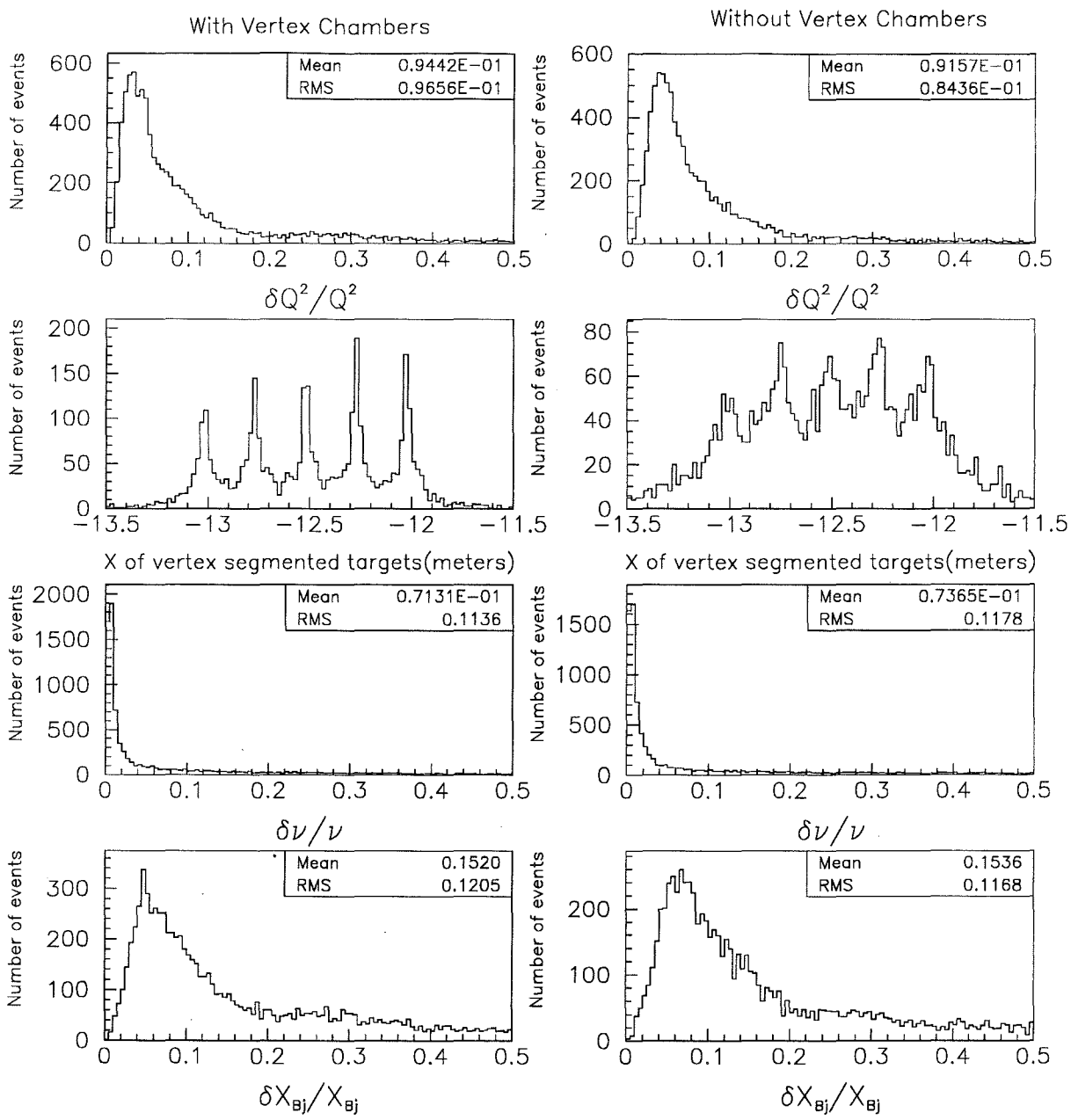

Figure 3.2: Vertex Chamber Resolution

shower into clusters. The clustering algorithm used seed pads and searched for local maxima to determined which pads were associated with a given maxima. If two clusters overlapped, the energy contained in the overlapping pads was apportioned between the two clusters (60) based upon an exponential function of the pad energy times the distance from a pad to the center of the cluster. After arbitration the energy and positions of all clusters were stored in LGLB banks. If no clusters were found, the LGLB bank contained a calorimeter error status word which was used to identify events which failed during some part of the calorimeter analysis and thus lost the calorimeter information.

3.8 Run90 Filter

The run90 filter was used to remove errors in triggering and non-reconstructable data from the offline reconstruction program. The filter examined the data from an event and if that data satisfied the filter criterion, they were written to an output tape. The filter was flexible and treated physics triggers differently from normalization triggers. There was also a class of events in which the muon had scattered in a downstream component of the detector, the PC chambers for example. These "off target" events fired one or all of the physics triggers, but because these scatters did not originate in the target material they were removed from this analysis. Off target scatters could be used to check normalization, therefore, these scatters were saved by the filter.

In the final configuration, an event was saved if it had a scattering angle greater than 0.3

mrad or energy transfer, ν, greater than 20 GeV/c, irrespective of the position of the vertex. Any event without a vertex was eliminated, unless the event was a randomly pre-scaled beam trigger, RSAT, for example. This filter was not applied to the output of every tape. During reconstruction of the data, one tape out of every nine was run with the filter turned off. In this case every event on the input tape was written to the output. The end of spill events which contained spill scaler LDEC banks were also preserved through the filter.

The run90 filter significantly reduced the number of events written to the output, typically only 36% of the events written to the raw data tapes survive to the output. The remaining events were either non-reconstructable or spurious triggers. Even after filtering the run90 data sample filled 414 Exabyte tapes.

3.9 Data Reduction and Splitting

In order to make the data set tractable, further cuts were applied to the data. The data reduction and data splitting programs were run in separate passes of the data. In the first pass, the data reduction program was run (DR90). DR90 wrote the highest quality data to a manageable number of tapes. All events which scattered outside the analysis target region were removed, all normalization triggers were removed and quality cuts were applied to the "in target" scatters. Quality cuts removed events in which the resolution on the important kinematic quantities was poor, or the calculated value unphysical. In order to pass the DR90 cuts, an event had to satisfy

every cut listed in table VI. Even though the cuts applied by DR90 were loose, for example

TABLE VI: Run90 Data Reduction Cuts

value	minimum	maximum
beam energy	0. GeV	1000. GeV
Q^2	0. GeV^2	1000. GeV^2
x_{Bj}	0.	100.
ν	0. GeV	1000. GeV
y_{Bj}	0.	10.
X of Vertex	-13.5 meters	-11.5 meters
$\delta Q^2/Q^2$	0.	1.
$\delta x_{Bj}/x_{Bj}$	0.	1.
$\delta\nu/\nu$	0.	1.

y_{Bj} is kinematically restricted to the range 0 to 1 and an upper limit of 10 was allowed, the DR90 program reduced the size of the data sample by approximately a factor of ten. DR90 was applied to all of the PTMVE tapes, including those run with the "no filter" option; the output was a set of 51 tapes which will be referred to DR90 tapes.

In a second pass, the normalization triggers were split onto a separate set of tapes. Normalization triggers were defined as all randomly prescaled beam triggers or end of spill events which contained the spill scalers which were need for beam flux measurements. These tapes will be referred to as "splitbeam tapes", 36 in all, and were used to deterimine beam flux. The combine DR90-Splitbeam sample amounted to approximately 150 Gigabytes of data; clearly

further selection was required.

3.10 The LOX Program: PAW DST Generation

Cross section ratio analysis, upon which this thesis is based, needed further selection of events. The physics and splitbeam tapes included events which were of interest to the entire E665 collaboration; this analysis requires only SAT and the associated normalization and monitor triggers. As a final pass on the data, a program called LOX was run on the DR90 and splitbeam tapes. Rather than write every word associated with an event, a subset of the available ZEBRA bank information was written out as a PAW Ntuple and saved on disk. A stricter set of quality cuts was imposed on the events before a Ntuple entry was filled; these cuts will be described below.

3.10.1 Beam Quality Requirements

Beam quality requirements were imposed on physics triggers as well as normalization triggers. The cuts were derived in order to save only the cleanest events for further analysis. Since event kinematics in inelastic scattering are completely determined by the muon, the LOX program rejected events with more than one beam muon. Figure 3.3 shows the beam multiplicity distribution for combined intime and out of time beam tracks.

Out of time muons were removed because they were a source of fake triggers. As mentioned

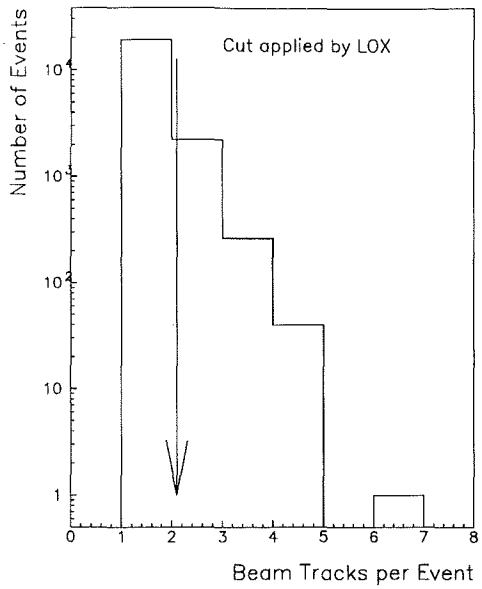

Figure 3.3: Beam Multiplicity Distribution

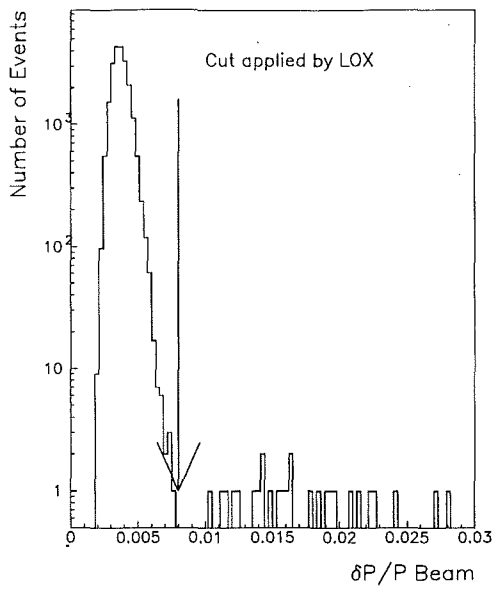

Figure 3.4: Beam Momentum Resolution

in Chapter 2, the SBT signals were routed through a splitter panel. The splitter panel was a resistor bridge which sent SBT signals to analog to digital converters (ADC) and pulse height discriminators. Due to mismatched impedances, the splitter panel introduced ringing in the cable. These reflected signals were rediscriminated and sent to the SAT electronics approximately 60 ns after the passage of the muon(see figure 3.5). False triggers were generated when an out of time muon, which would normally not have fired the trigger, coincided with a reflection which provided the SBT station 4 contribution to the trigger matrix. Since the reflection was generated from a different beam track, the veto window which was defined for this out of time-misprojected beam combination was incorrect, and since no muon showed up in the veto window these events were written to tape. The LHOD bank information provided a simple way of identifying these out of time beam events and removing them from any analysis. The LHOD

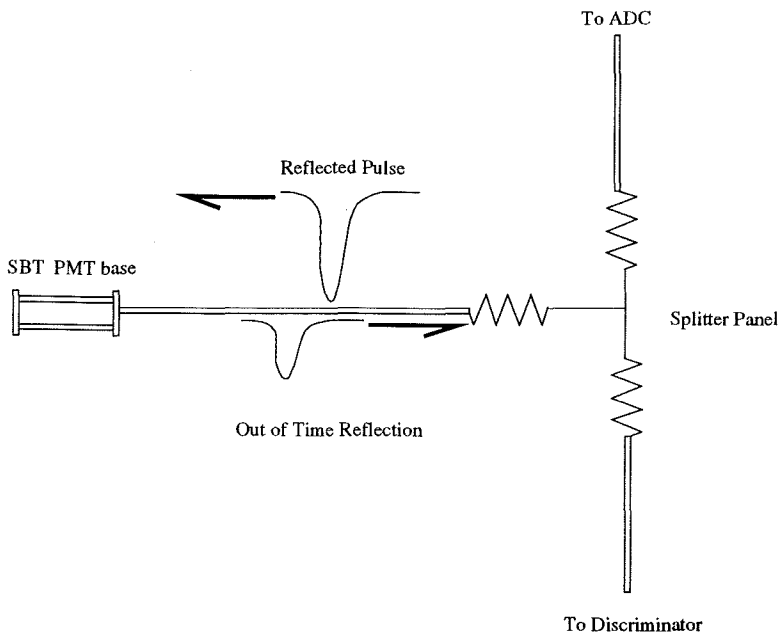

Figure 3.5: The SBT Reflection

bank of the reconstructed beam was examined and if it satisfied the in-time requirement, the hodoscope fingers which it had passed through were compared with the SAT trigger matrix arrays. If an intime beam didn't satisfy the SAT BY and BZ beam conditions simultaneously, the event was rejected from further analysis.

The last condition imposed was on the quality of the reconstructed beam track. The incident beam was required to have energy greater than 0. but less than 1000 GeV. These cuts were complemented by rejecting any events which had a fractional error in beam momentum, $\delta p/p$, greater than 0.8%. Figure 3.4 shows the distribution of fractional error in beam momentum. In addition, events which contained more than one forward spectrometer track which was identified as a muon were rejected. The beam quality requirements are summarized in table VII.

TABLE VII: DST Beam Requirements

Beam Quality Cuts (Applied to SAT, RSAT AND SATPS)

i) Not more than 1 incident muon
ii) Not more than 1 forward spectrometer muon
iii) Beam trigger matrix satisfied by an intime muon
iv) $\delta p/p < 0.008$ for the beam muon
v) Beam momentum > 0.
vi) Beam momentum < 1000.

3.10.2 Physics Trigger Requirements

A second set of quality cuts was applied to SAT and SATPS triggers but not to RSATs. In addition to tighter kinematic cuts, the χ^2 of the muon match was required to be less than 10 in the Y and Z projections. Based on a hand scan of events it was determined that any matched muon which had χ^2 greater that 10 was not likely to be a muon. Typically these events were identified as muons because the real muon track was not reconstructed. The χ^2's in position, Y and Z, were checked separately; slope matching was not used. Some very loose cuts were also applied in order to restrict event kinematics to their allowable values. A full list of the additional cuts appear in Table VIII.

Events which satisfied these requirements were passed to the rest of the program which marched through the event picking out relevant information and storing it as a PAW Ntuple entry. The LOX program also saved spill-by-spill statistics on spill scalers, the number of

TABLE VIII: DST Physics Requirements

SAT and SATPS Quality Cuts (Applied after beam requirements)

$$
\begin{aligned}
&i)\ \chi^2_{Y\,\text{displacement}} < 10 \\
&ii)\ \chi^2_{Z\,\text{displacement}} < 10 \\
&iii)\ 0 < Q^2 < 1000 \\
&vi)\ 10 < \nu < 1000 \\
&v)\ 0 < y_{Bj} < 1 \\
&vi)\ 0 < x_{Bj} < 1
\end{aligned}
$$

normalization triggers etc. These spill-by-spill statistics were given one entry per spill and stored as an additional Ntuple. Finally, a text file which was a run-by-run-by-target summary of the number of events which failed each of the LOX cuts was written to disk. The once-per-spill Ntuple and statistics text files were not used in the final physics analysis but were found to be invaluable in identifying bad runs and verifying the normalization of the DR90-Splitbeam streams.

3.11 Data Validation

The splitting off of the RSAT triggers onto separated tapes reduced the size of the DR90 sample considerably. Unfortunately it introduced a possible source of error. If by some unforeseen "glitch" the data written to the splitbeam tapes did not exactly reflect the data written to the PTMVE tapes, the use of the splitbeam tapes for normalization would be in error. The most obvious solution would have been to save all the normalization triggers through the DR90

program, thus eliminating the need for a data split. Alternatively, one could read the pre-DR90/Split tapes which had physics and normalization data intact. A third option, was to split the data and thoroughly validate the results. For run90, split/validation was implemented, in analysis of run91 data, the pre-split data was analysed. The run91 data was used to measure the hadron self vetoing in the SSA.

Figure 3.6 summarizes the full analysis path from raw data tapes to final results. Raw data was first reconstructed and filtered. Next the output of the PTMVE was sent through three separate paths. The leftmost was data reduction which produced a data set reduced by approximately a factor of 10. The splitbeam (rightmost) contained only randomly pre-scaled beam triggers and scaler information. Both of these streams were used in this analysis.

The center stream was run on a subset of all the PTMVE tapes for the sole purpos of validating the DR-Split proceedure. One PTMVE tape was selected from every splitbeam tape. The PTMVE tape was run through the LOX program which produced an Ntuple and text file of per target input - output statistics. Typically every raw data tape contained a single run block, and therefore the PTMVE tape generated from a given raw data tape would span the same run block. Since splitbeam tapes ran across several run blocks, the statistics file reported input-output statistics for every run block separately. The I/O statistics from a PTMVE tape were compared to the corresponding run on the splitbeam tape. The number of RSAT triggers recorded on a PTMVE tape were required to match exactly the number of triggers on the

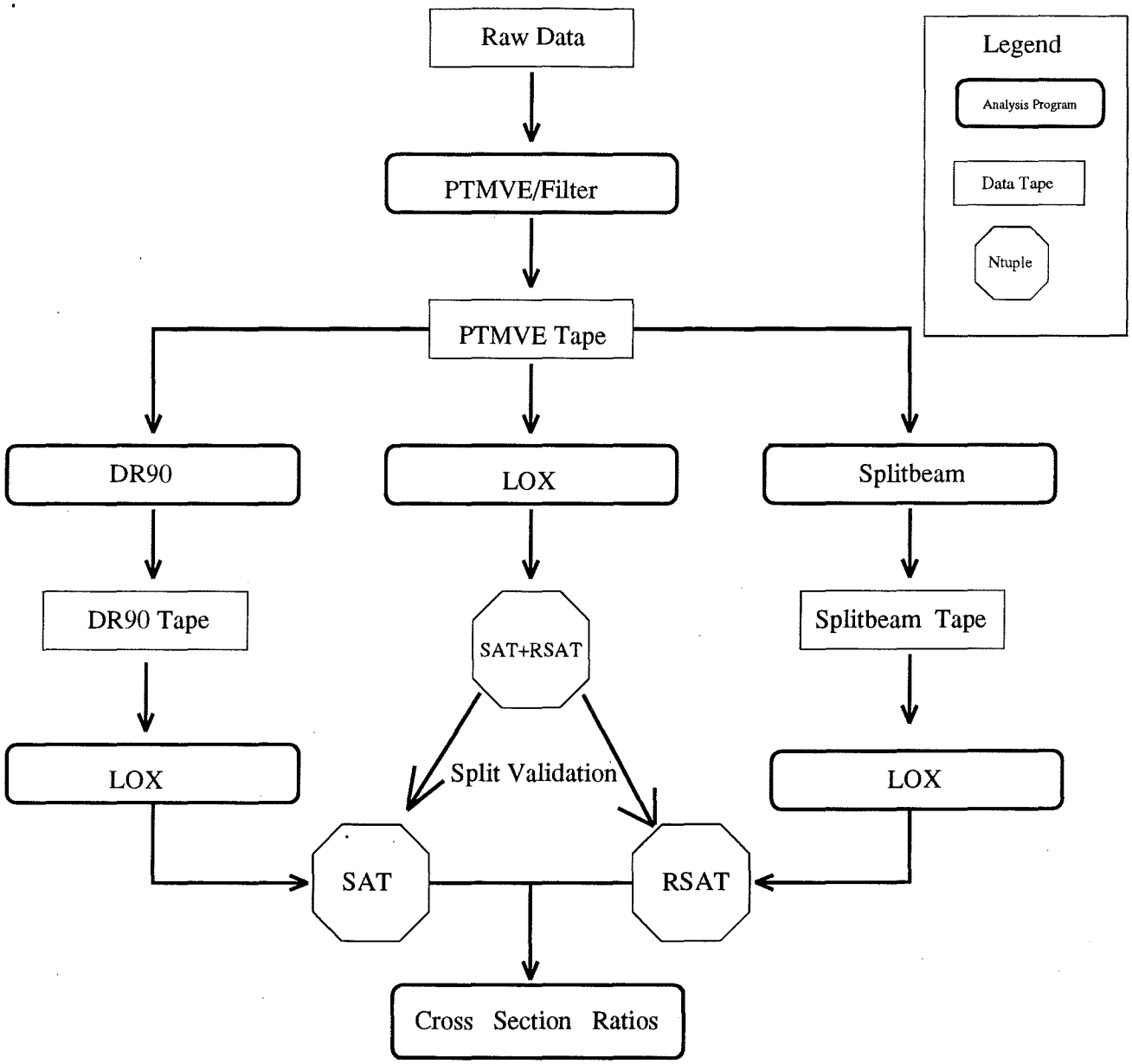

Figure 3.6: Analysis Flowchart

splitbeam tape.

In the first iteration of this validation, several run blocks had discrepancies in the number of triggers. These errors fell into two categories, both of which were attributed to the assumption that each raw data tape contained a single run block. The most obvious problem arose when a tape was chosen which was one of the tapes run with the run90 filter code turned off. The number of data words which described an event was increased, on average by a factor of 2 by the PTMVE program. Thus "no filter" tapes split run blocks onto different PTMVE output tapes, which explains why the number of RSAT triggers on this tape did not agree with the splitbeam tape. When the number of triggers on a PTMVE tape didn't agree with the splitbeam tape, if the PTMVE tape was proven to be a "no filter" tape, a different input tape was chosen for comparison.

A second type of error occurred when a run block was started on one raw data tape and finished on a second tape. This resulted in fragmented run blocks on more than one PTMVE output tape. In this case the second tape which contained the remainder of the run block was analysed and the triggers on both tapes were summed and compared with the splitbeam tape.

Of the initial sample of runs chosen from the splitbeam tapes 25 of 32 tapes agreed with no further investigation. There were 3 tapes which were found to be "no filter" tapes, the remaining 4 tapes sampled runs which had run across tape boundaries. After the 7 tapes which failed the

first pass were rerun with complete run blocks included, the results converged.

In order to check the data reduction path, the Ntuples produced from the LOX program were used. The events which were caused by SAT triggers were selected and the quality cuts imposed in the DR90 program were applied. If a scatter satisfied all the DR90 cuts it was given an entry in a histogram which was binned as a function of target. One such histogram was filled for each run block. An identical set of histograms was produced from the DR90 tapes and the PTMVE tape subset. The results from the two different analysis paths were compared, for an example see figure 3.7. The histogram ID represents the run number sampled and each bin is a separate target. The solid lines are the histogram which measures the number of scatters from the PTMVE tape. Overlayed as solid dots are the number of scatters saved on the DR90 tapes for that run block.

Every run and target was compared and only one run block was found to have a different number of SAT triggers. The run block number was 12323 and this run block had run across *three* PTMVE tapes. To address this problem the tapes which contained the remainder of the run were run and histograms re-generated at which time the results agreed.

3.12 Summary

Raw data was reconstructed and filtered using the E665 PTMVE program. In order to make the run90 data as accessible as possible, E665 split its physics and normalizations triggers onto two separated sets of tapes. To validate the splitting procedure, a subset of runblocks were chosen and compared to the un-split tapes. Both the DR90 and beam split tapes were found to contain the same data as the tapes which were input to the splitting procedure. Any perceived errors were shown to follow from the assumption that each tape contained a single complete run block.

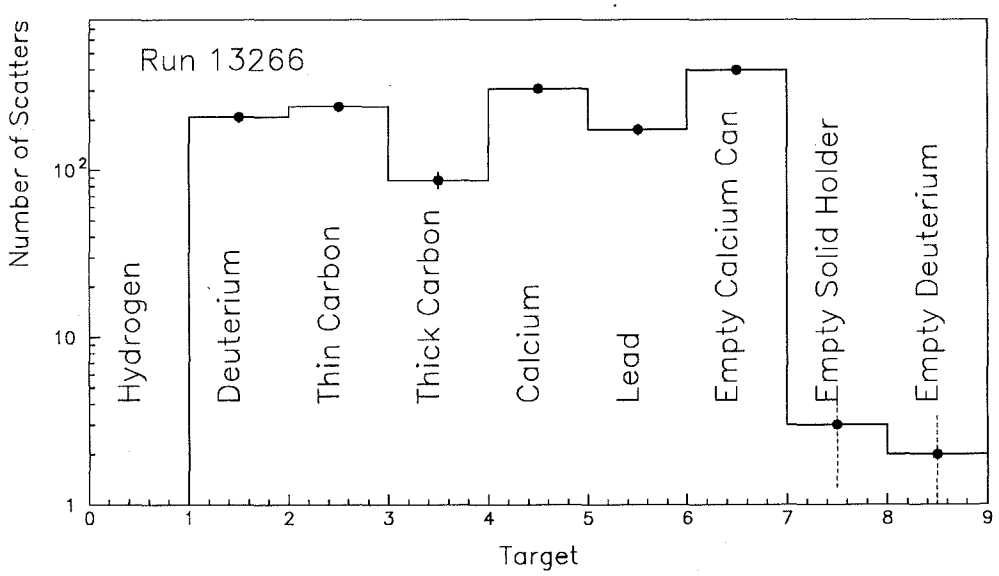

Figure 3.7: Comparison of Scatters from DR90 and PTMV

4. ANALYSIS CUTS

In this chapter the cuts which were applied to the PAW DST Ntuples in order to extract a sample of deep inelastic scatters will be discussed. Although the DST production program was run with the intention of saving only the highest quality data, cuts were chosen to be loose enough so as to allow further study. The resulting sample retained a small number of poorly reconstructed scatters which required more stringent cuts. The DST data also contained a large fraction of background events which mimicked deep inelastic scatters. These background events were identified and removed before final cross section ratios were determined.

4.1 DST Distributions

The DST data consisted of several thousand scatters and normalization triggers. The number of scatters and normalization triggers are listed in Table IX.

TABLE IX: Event Statistics Before Analysis Cuts

	SAT	RSAT Per Prescale Run Period		
Target	Events	I	II	III
^{2}D	227144	7101	70748	38373
^{12}C(Thin)	28990	0	339	9820
^{12}C(Thick)	211802	3365	32177	19767
^{40}Ca	295994	6514	62773	35024
^{208}Pb	287118	11314	101796	102126
Empty Ca	2189	939	9277	20847
Empty Solid	1822	3024	25991	10560
Empty D	2779	3751	34825	9590

4.2 Run Dependence

As mentioned in Chapter 2, run90 data were taken over a period of 3 months. During that time, hardware failures and "fixes" resulted in a detector response which changed throughout the run. Because targets were interchanged every minute or so, effects which could alter cross section ratios were minimized. However, time dependent effects which affected muon reconstruction, calorimeter response and beam flux measurements were examined. These studies will be described below.

4.2.1 Alignment

Normally if a chamber was found to be inoperable, or inefficient during the run, the chamber was removed, fixed and re-installed. After a chamber was replaced, its position was recalibrated with an alignment run. In this section a method for measuring the stability of the alignment constants will be described.

The RSAT beam triggers were used as one method of validating alignment constants. Since muon momentum was measured in both spectrometers, the beam and forward spectrometers were used to cross-calibrated each other. The procedure was straight forward: the muon momentum measured by the beam spectrometer was compared to the momentum as measured by the forward spectrometer. The two values were expected to be equal for an unscattered muon. Figure 4.1 shows the distribution of the measured energy transfer, ν, for unscattered muons. As expected the difference was peaked a zero indicating that beam and forward spectrometers were properly calibrated for this alignment period.

In order to search for run dependence in alignment, the ν distribution for unscattered muons was fitted run-by-run. $< \nu >$ was plotted against run block and and is shown in figure 4.2. Clearly there was a systematic shift in the measured value of ν for the early running periods. Since $x_{Bj} \propto 1/\nu$ this misalignment would cause a miscalculation of x_{Bj}, therefore these run blocks were removed from further analysis.

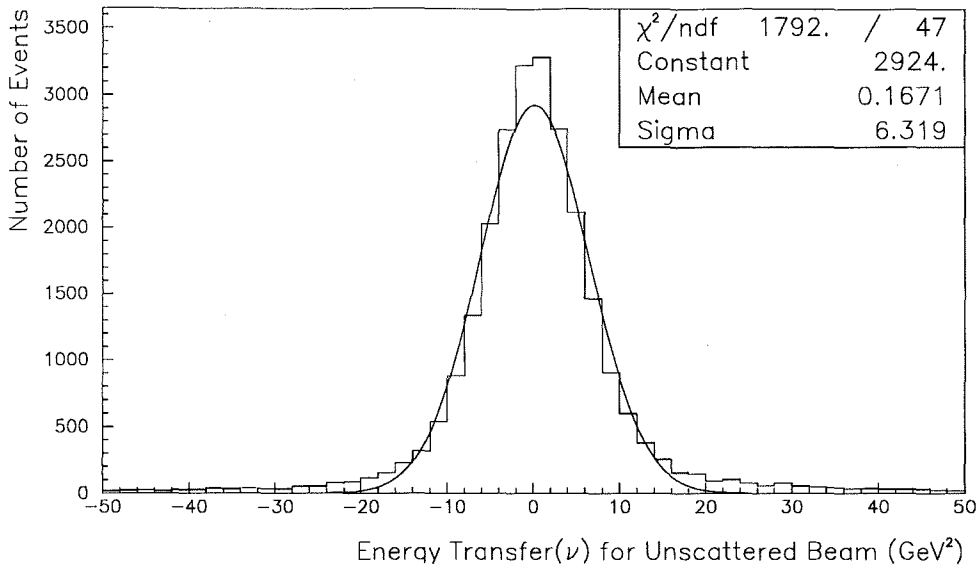

Figure 4.1: ν For Unscattered Beam

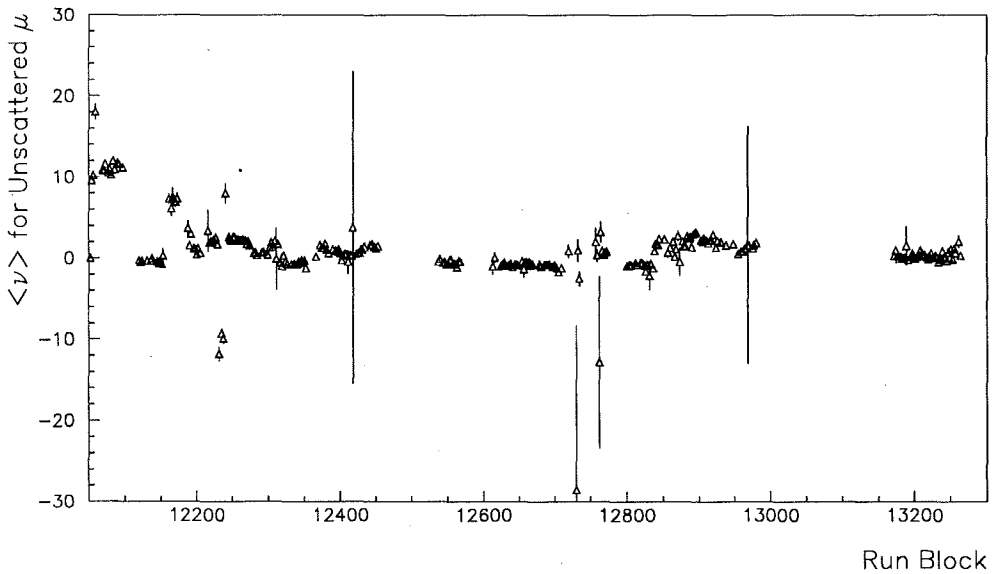

Figure 4.2: $< \nu >$ For Unscattered Muons vs.Run

4.2.2 Scalers

Randomly prescaled beam triggers(RSAT) were used to measure beam flux. The number of RSAT triggers was converted into muon flux using:

$$\text{Beam Flux} = \text{Number of RSAT Triggers} \times \text{Prescale Factor}. \tag{4.1}$$

Before the RSAT triggers could be used as a measurement of the beam flux, it was necessary to prove that the prescaling worked properly. The procedure for checking the prescaling was to find an independent measurement of the beam flux and compare it to what the RSAT triggers had reported. Splitbeam Ntuples contained the RSAT triggers and the spill scaler results. The correspondence between the number of RSAT triggers and the amount of SAT beam recorded by the spill scalers was used to validate the prescale value. In figure 4.3 the ratio

$$\text{Ratio} = \frac{\text{Number of RSAT} \times \text{Prescale Factor}}{\text{SAT Beam from the Spill Scaler}} \tag{4.2}$$

is shown.

If beam prescaling was implemented correctly, this ratio should be unity. The prescale factor was intentionally changed throughout the run and each different prescale factor defined a different running condition. The top three distributions in figure 4.3 show the ratio formed for every spill. The second row represents the sum of triggers and scalers over an entire run. Each column in figure 4.3 corresponds to a different run period which was defined by the loaded prescale factor. The results of a gaussian fit to the peak is superimposed as a smooth curve and

the results reported in the box. Fit results have also been tabulated below.

TABLE X: Fit Parameters for RSAT Prescale Validation

Fit Parameter	Period I	Period II	Period III
Calculated Spill by Spill			
Prescale factor	131072	262144	524288
Rsat per Spill	30-40	20-60	15-30
Mean	1.32	0.99	1.00
σ	0.210	0.170	0.228
Calculated Run by Run			
Prescale factor	131072	262144	524288
Rsat per Run	200-1000	300-600	100-300
Mean	1.32	0.993	0.997
σ	0.042	0.034	0.037

The amount of prescaling required was large. Values of the prescaler ranged from 2^{17}(one trigger per 131072 beams) to 2^{19}(one trigger per 524288 beams). Typically the number of muons delivered during a spill was 18 million so that on average only 30 to 50 RSAT triggers were written per spill. The resulting statistical fluctuations cause the distributions in the top row 4.3 to be broad. When spills from a common run are combined the effect of statistical fluctuations become less pronounced and the width of the peaks becomes smaller.

A systematic shift of the ratio from unity was discovered in the 2^{17} prescaling run period. The shift indicated that there was a discrepancy of 32% between the beam flux as measured

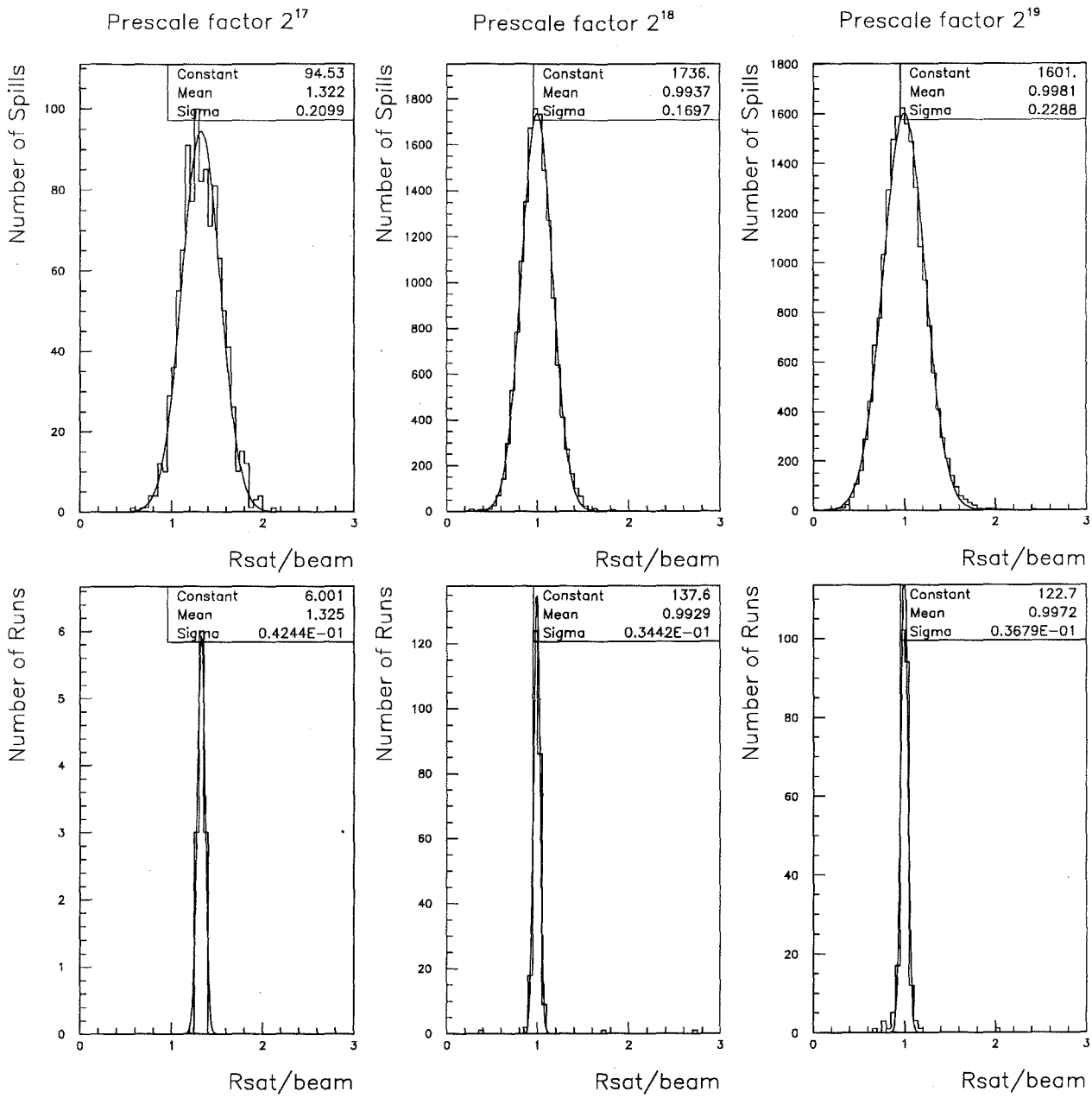

Figure 4.3: Comparison of RSAT to Spill Scalers

using scalers and RSAT triggers. Without any additional information, one could not determine which method of normalization was correct. Since these are the same run blocks which suffered from improper alignment constants, they were eliminated from further analysis.

4.2.3 Interfile Event Loss

One feature of the E665 data aquisition system was that multiple files were written to a common exabyte tape. In order to minimize the dead time introduced by tape writing, data were stored in a buffer between the time they were read from the spectrometer and written onto tape. The exabyte tapes which were used to store data required a relatively long time to open and close files. During this time the buffers which were used to store the incoming data occaisionally overflowed and events were lost from the data stream (61). The events which were lost sometimes included the End of Spill event which contained spill scaler information. Since either the spill scaler information or some portion of the RSAT triggers were lost from a such spills, these spills could not be included in the previously described validation of the RSAT prescaling. These spills were treated as a special case and will be described below. A total of 8.8% of all spills suffered from this "interfile event loss".

The spills which were included in figure 4.3 were restricted to have every RSAT trigger recorded to tape accounted for in the RSAT spill scaler. The interfile event loss spills were identified by comparing the number of RSAT triggers written to tape to the number of triggers

counted in the RSAT spill scaler channel. If it could be shown that the interfile event loss was random with respect to the type of trigger, then this loss will have occurred with equal probability to physics triggers and normalization triggers. Therefore RSAT triggers could still be used to normalize the physics triggers for these spills.

The procedure for quantifying the effect of these losses was to measure some cross section for those spills which suffered interfile event loss. The cross section was compared to an identical measurement made using the complete spills. Since acceptance, efficiency and target were identical for both samples the cross sections could be compared directly. The physics sample chosen for comparison was those events which were low Q^2 and high energy transfer, ν. The low Q^2, high ν region was populated by large number of coherent muon bremsstrahlung($\mu\gamma$) events.

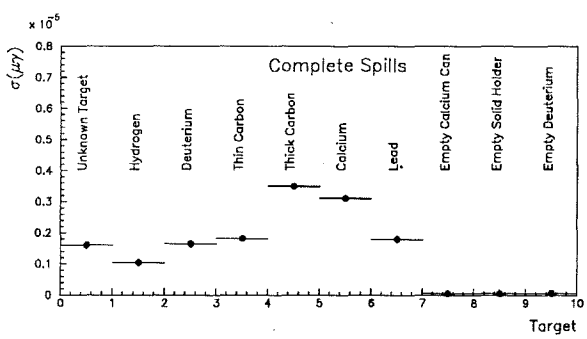

Figure 4.4: $\mu\gamma$/beam

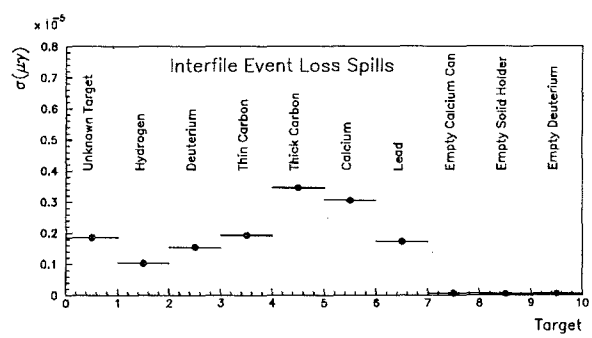

Figure 4.5: $\mu\gamma$/beam Interfile Event Loss

Figure 4.4 shows the pseudo-$\mu\gamma$ cross section defined as:

$$\sigma(\mu\gamma) \equiv \frac{\text{SAT with } (Q^2 < 1.) \text{ and } (\nu > 100)}{\text{RSAT} \times \text{Prescale factor}} \tag{4.3}$$

for those spills which were completely recorded versus target type. The label "Unknown Target" are events which the target identifier word was not properly written to tape. Figure 4.5 are interfile event loss spills. Since the measured cross sections agree, the interfile event loss did not discriminate between trigger or target type, therefore these spills were not removed.

TABLE XI: Interfile Event Loss $\sigma(\mu\gamma)$ Versus Target

	$\sigma(\mu\gamma)$		
Target	Complete Spills	Interfile Event Loss	Diff(%)
^{2}D	1.65×10^{-5}	1.55×10^{-5}	6.06
^{12}C	3.49×10^{-5}	3.46×10^{-5}	0.01
^{40}Ca	3.12×10^{-5}	3.04×10^{-5}	0.03
^{208}Pb	1.79×10^{-5}	1.71×10^{-5}	4.47

4.2.4 Calorimeter Response

The time dependence of the electromagnetic calorimeter (ECAL) response was also examined. As will be discussed later, the calorimeter was used to identify and remove background events from the DIS sample. Muon bremsstrahlung was the dominate background identified using the calorimeter. The robustness of the method of removing background depended on ECAL response and systematic shifts due to gas composition or aging. The calorimeter response was measured for two samples of data. One was chosen which would track its response to high energy clusters over time, the second measured the response to low energy clusters.

ECAL Response to Low Energy Clusters

In order to track the calorimeter response to low energy clusters, the calorimeter energy was examined for high Q^2 events. A lower limit cut of $Q^2 > 1.5$ GeV was applied to the data to remove as much of the $\mu\gamma$ background as possible. The total calorimeter energy for these events was examined for each run; an example of such a distribution is shown in figure 4.6. The mean

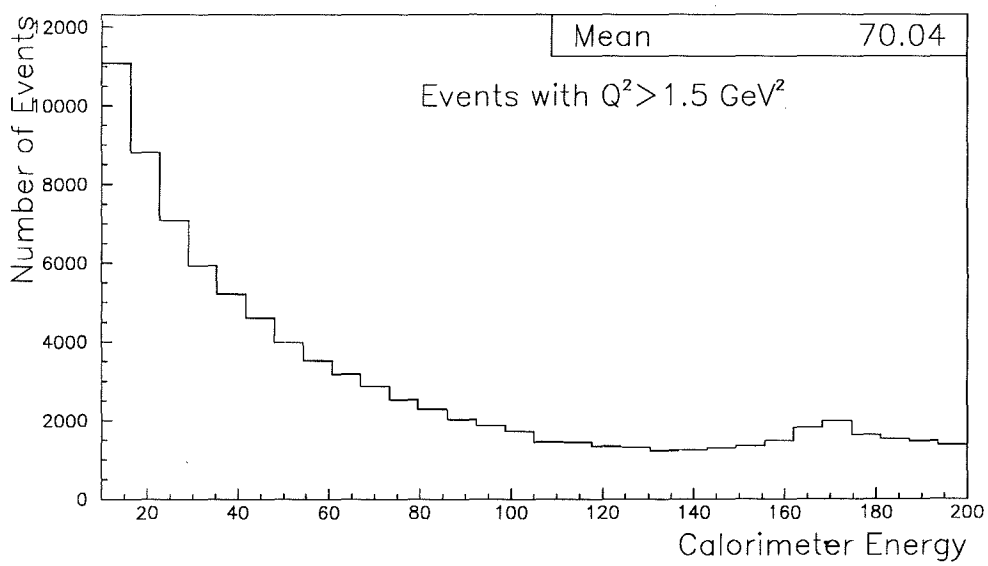

Figure 4.6: Calorimeter Energy For DIS Candidates

and error on the mean of the distribution is plotted against run number in figure 4.7A. Several features are obvious. First, there are large gaps in the data. These were periods during which either alignment or other calibration took place; these gaps should be ignored. In addition, there were a few large fluctuations in the mean calorimeter energy. The most predominant was at approximately run 12300. These were caused by a single, localized, calorimeter pad tower

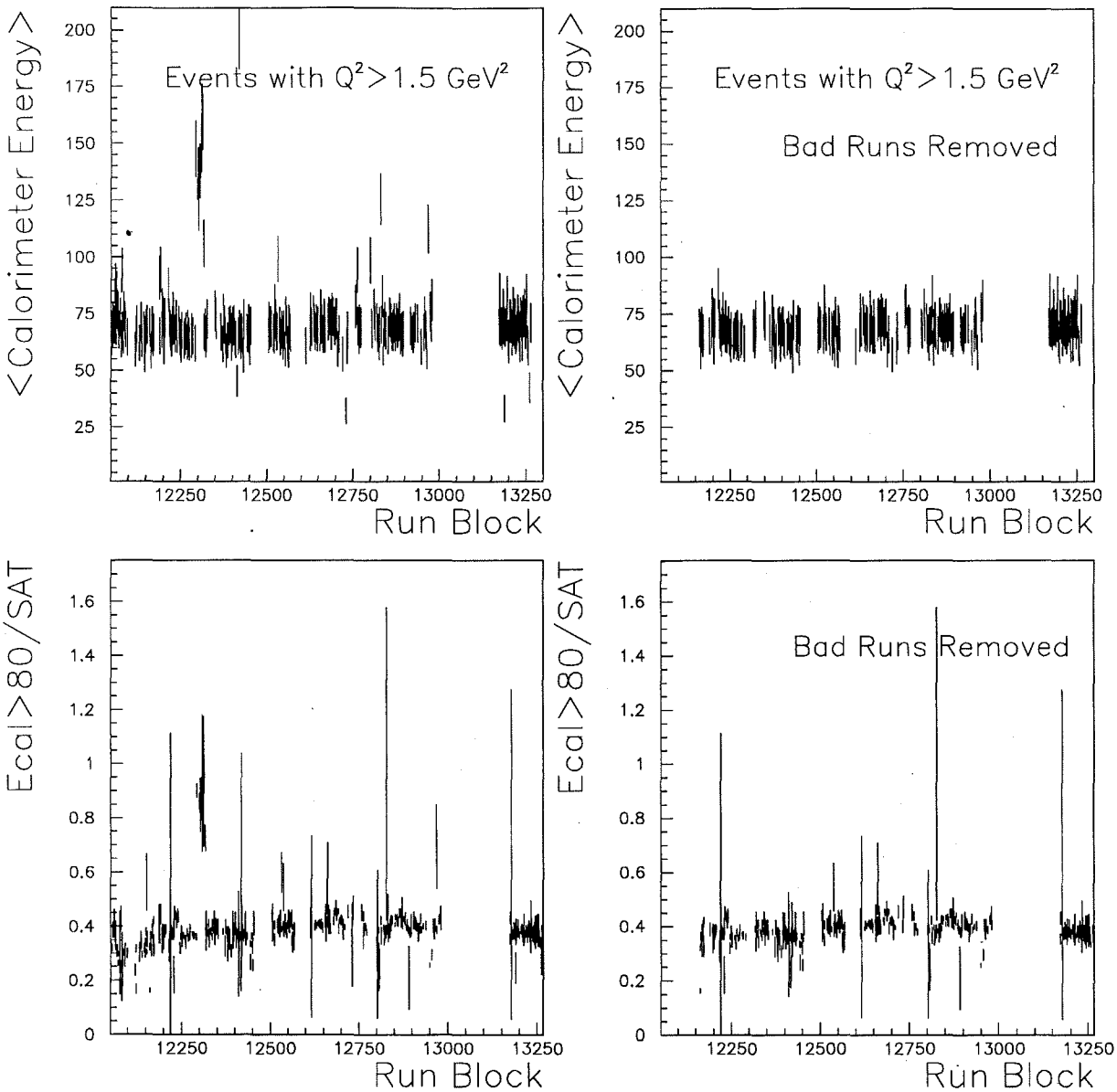

Figure 4.7: Bad Runs Based on Calorimeter Response

which, due to an electronic oscillation, incorrectly reported 170 GeV. These runs along with every run with a mean energy of greater than 90 GeV or less than 50 GeV were removed from this analysis.

ECAL Response to High Energy Clusters

The SAT trigger acceptance was such that only $\mu\gamma$ scatters which involved energy transfers of several tens of GeV fired the trigger. To monitor the calorimeter response to these photons, the number of events in which more than 80 GeV of energy was detected by the ECAL was divided by the number of SAT triggers. Figure 4.7C shows the number of these events per SAT trigger versus run block. The calorimeter oscillation at run 12300 is apparent. In addition there are several points near the beginning of data collection were fewer high energy photons were reconstructed. These runs had already been removed from this analysis. The low energy and high energy cluster time dependence plots after bad runs have been removed are in shown in figures 4.7B and 4.7D.

4.2.5 Target Cycling

As a test of target cycling, each run was checked to verify that all targets were being exposed to the beam. The data from targets which were used in each run were compared in order to insure that targets were being interchanged properly. A period of 10 run blocks was discovered

during which the cryogenic target vessels were under repair. Since no deuterium data were taken during this time these runs were not used in this analysis. There was also a single run block in which several thousand deuterium scatters were recorded without any solid target data; this run was also removed. A small fraction of the runs were missing one or more targets. These runs were well separated in time and typically consisted of only a few spills. This was due to the predetermined target cycle not running to completion before a data aquisition failure. These spill were not removed.

Finally, the number of RSAT triggers were compared to the number of SAT triggers, for each run block, in order to find errors in the Data Reduction/Splitting procedure. One run block was discovered which approximately 200 SAT triggers per target were recorded. For that run block no RSAT triggers existed in the normalization Ntuples. Similarly a different run block had 8×10^9 beam muons but no scatters. These run blocks were unnormalizable; for this reason they were removed from further analysis.

4.3 Kinematics Cuts

After the bad runs had been removed, cuts were determined in order to remove scatters which exhibited poor resolution or resulted from spurious triggers. An additional cut, based on the measured calorimeter energy was also applied to remove non-DIS background events. Table XII shows the numbers of events and beams after removal of bad runs but before kinematic cuts

had been applied.

TABLE XII: Event Statistics Before Kinematic Cuts

	SAT	RSAT Per Prescale Run Period	
Target	Events	II	III
^{2}D	164050	58915	24751
^{12}C(Thin)	17807	0	6090
^{12}C(Thick)	148387	26529	12370
^{40}Ca	207615	51266	22117
^{208}Pb	194108	82898	63521
Empty Ca	1438	7322	13061
Empty Solid	1316	21030	6460
Empty D	2088	28186	6595

4.3.1 Minimum Q^2

All scatters were required to have a minimum Q^2 of 0.1 GeV^2. A Monte Carlo simulation of the detector was used to determine the minimum value of Q^2 which would fire the small angle trigger. For this simulation a sample of RSAT beam triggers from data was used as input. In order to populate the kinematic region where the trigger acceptance varied rapidly, a non-physical cross section was generated. The cross section was chosen to be flat in scattering angles θ and ϕ as well as scattered muon energy. Only the scattered muon existed in the final state of this hypothetical interaction; no hadrons were generated. The scattered muon was then tracked through the forward spectrometer using a Geant simulation of the detector. The true position

of the muon at all the trigger planes was used to determine if the SAT trigger would have fired.

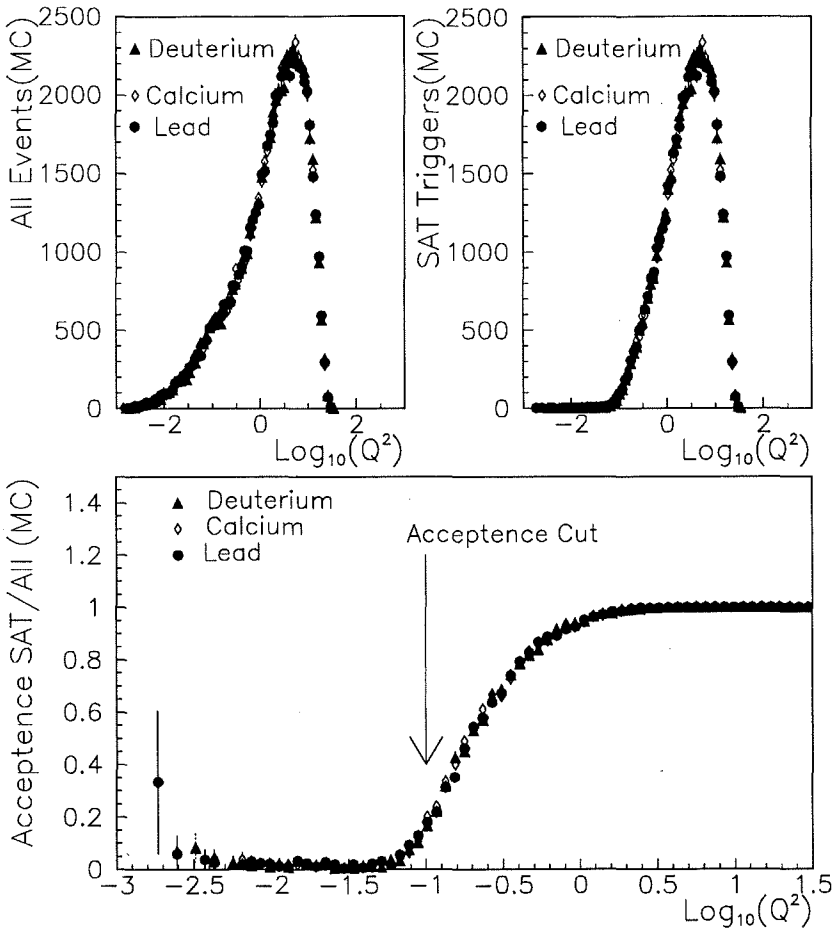

Figure 4.8: Trigger Acceptance for "Bare" Muons vs. Q^2

In figures 4.8 and 4.11 the bare muon Q^2 and y_{Bj} distributions are presented. The generated distributions are shown in 4.8A and 4.11A. Those muons which would have fired the SAT trigger are plotted in figures B and trigger acceptance is plotted in 4.8C and 4.11C. As mentioned in Chapter 2, the deuterium target was a one meter long liquid target and the solid targets were segmented along the beam axis. The deuterium, carbon and lead targets had a common radius of

approximately 5.0 cm, calcium target was slightly smaller, having a radius of 3.5 cm. The results for the three different target geometries are overlaid and denoted by different markers. Figure 4.8C shows the where the minimum Q^2 cut was chosen. The ratio of geometric acceptances are shown for the 3.5 cm (calcium) and 5.0 (lead) target to deuterium. The difference in acceptance between the three target geometries was negligible.

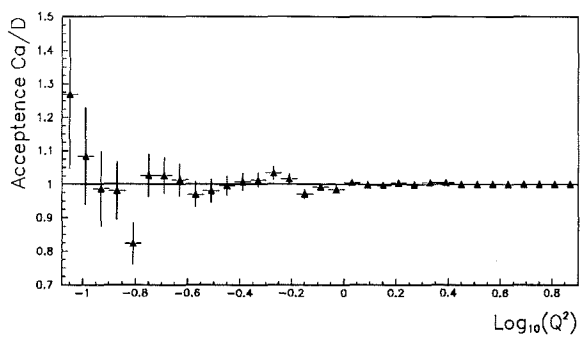

Figure 4.9: Q^2 Acceptance: Ca/D

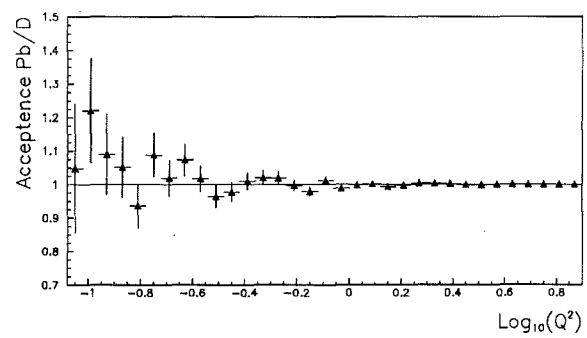

Figure 4.10: Q^2 Acceptance: Pb/D

The acceptance function shows only a weak dependence on y_{Bj}. This is a consequence of the forward spectrometer magnet configuration. The CCM and CVM magnets had their fields adjusted so as to focus muons at the trigger planes independent of the energy of the muon. Since y_{Bj} depended on the scattered muons energy, y_{Bj} acceptance was flat as expected. Figures 4.12 and 4.13 show the ratio of acceptances for the two solid target sizes. No acceptance correction was necessary.

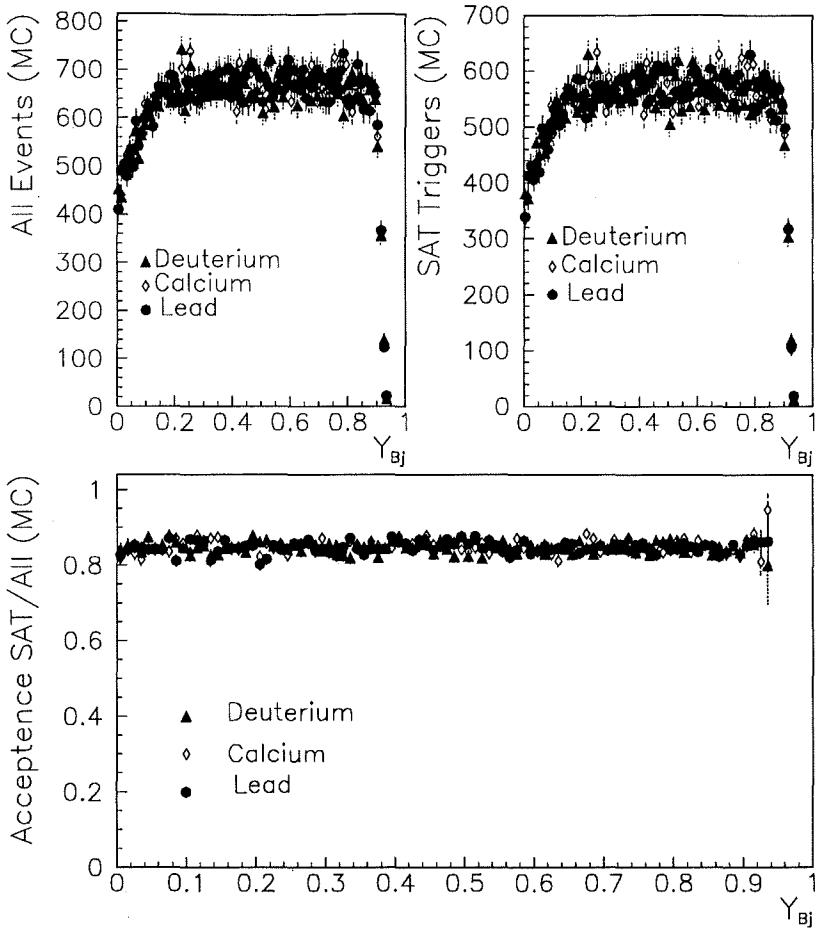

Figure 4.11: Trigger Acceptance for "Bare" Muons vs. y_{Bj}

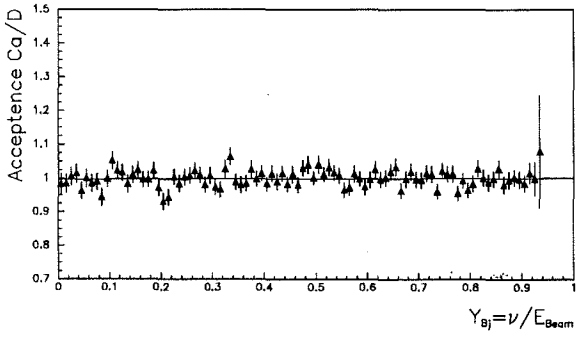

Figure 4.12: y_{Bj} Acceptence: Ca/D

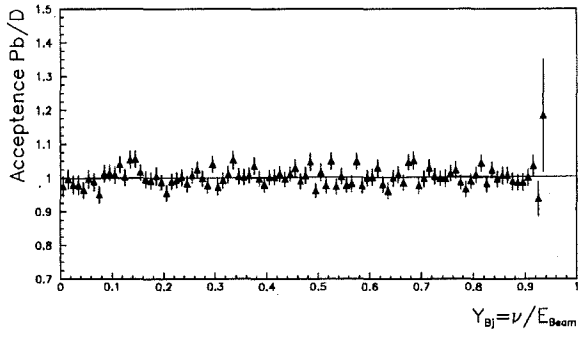

Figure 4.13: y_{Bj} Acceptence: Pb/D

4.3.2 Maximum y_{Bj}

All scatters were required to have a y_{Bj} value less than 0.7. Studies of hadron contamination in the scattered muon sample have shown that approximately 3-4% of all identified muons were actually low energy hadrons which were incorrectly identified as a scattered muon (62). Since these mismatched hadrons were of low energy, they populated only the region of high y_{Bj}. To remove this background ones needs only to restrict the chosen y_{Bj} region. For this reason a upper limit on y_{Bj} was chosen to be 0.7 which removes all but approximately 0.5% of the misidentified hadrons.

4.3.3 Resolution

A cut was imposed to remove poorly reconstructed muons. Events which were reconstructed and found to have a relative error on x_{Bj} greater than 20% were removed from further analysis. These events were found to have a high probability of being assigned to an incorrect x_{Bj} bin. In figure 4.14 the fractional error on x_{Bj} is shown, an arrow indicates the cut imposed on data.

4.4 Calorimeter Cuts

A large fraction of the data which survive the cuts outlined above were not deep inelastic scatters. Two processes which mimicked DIS were elastic muon-electron scattering and coherent muon

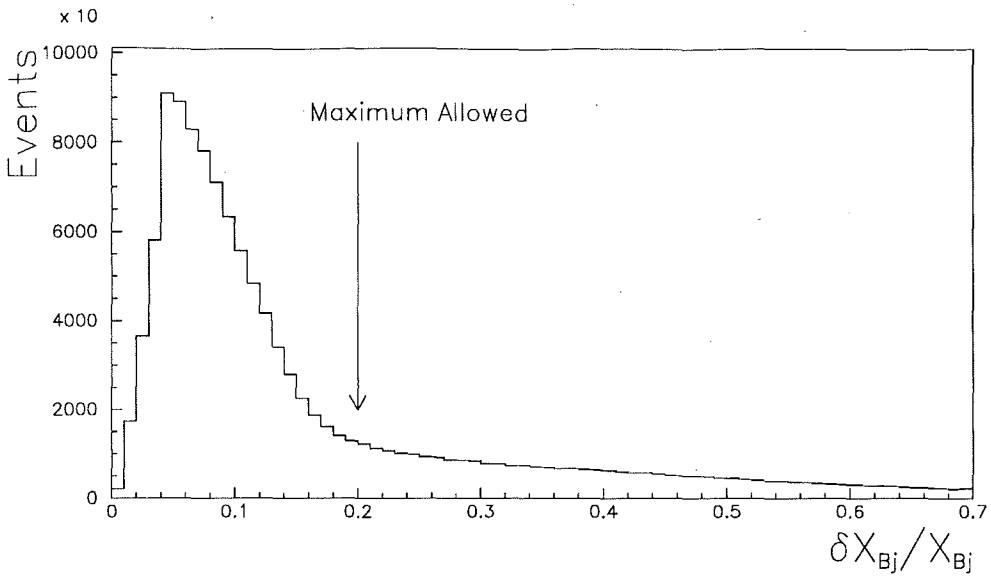

Figure 4.14: Fractional Error on x_{Bj}

bremsstrahlung. In this analysis the electromagnetic calorimeter was used to remove these backgrounds. The following section will describe how these background events were identified.

4.4.1 μe^- and $\mu\gamma$ Backgrounds

Elastic muon-electron scatters (μe^-) were identified by observing a single high energy electron in the final state. Since muon-electron scattering involved an electron which was to good approximation at rest, the kinematics restricted the measured x_{Bj} to be:

$$x_{Bj}(\mu e^-) = \frac{m_e}{m_P}. \tag{4.4}$$

Figure 4.15 shows the x_{Bj} distribution of sample of events in which a single negatively charged track in addition to the scattered muon was reconstructed. The arrow denotes $x_{Bj} = m_e/m_P =$

1/1836.

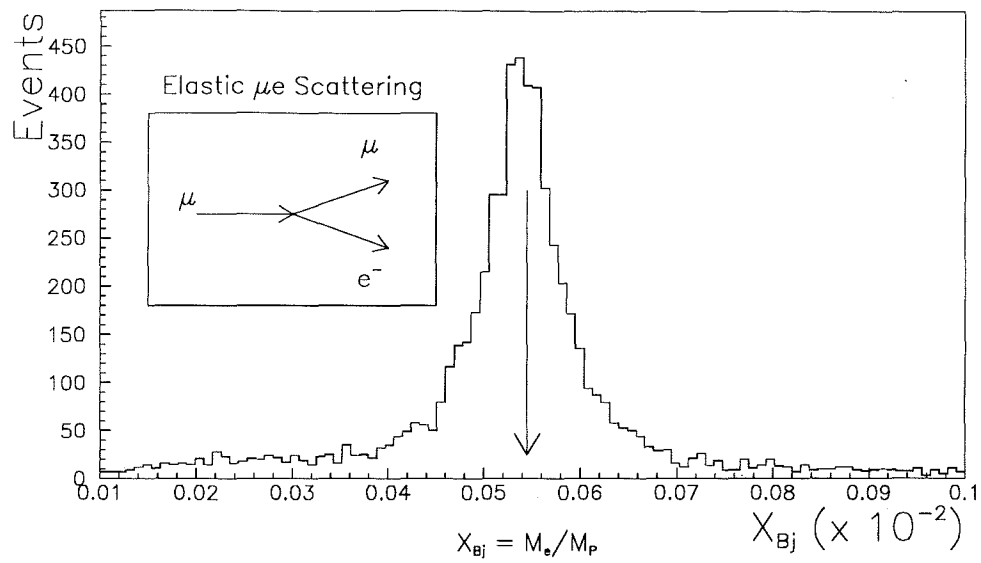

Figure 4.15: The x_{Bj} Distribution of Elastic μe^- Scatters

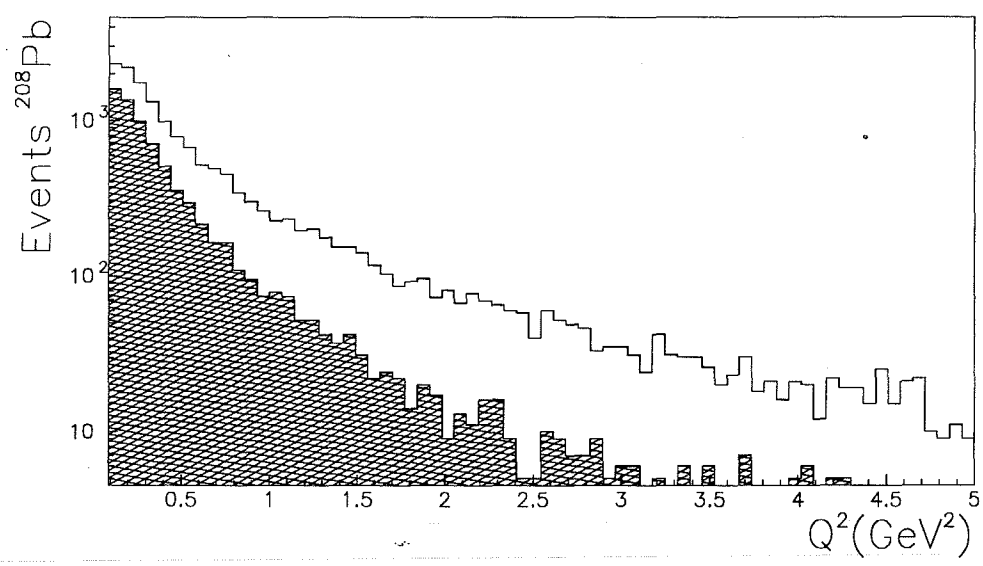

Figure 4.16: The Q^2 Dependence of $\mu\gamma$ Scatters

Muon bremsstrahlung scatters($\mu\gamma$) resulted in a single high energy photon being emitted from the interaction vertex. Since E665 used PWC's for forward tracking, these photons were undetectable by the forward spectrometer. The only method of observing these photons was by detecting them in the calorimeter. The kinematics of these scatters was such that they populated the region of low Q^2 and high energy transfer, ν. Figure 4.16 shows the distribution of Q^2 for all events taken on the lead target. Superimposed as a shaded histogram are those events which are candidates for being $\mu\gamma$ scatters. The shaded distribution had no forward spectrometer tracks other than the scattered muon and $y_{Bj} > 0.3$.

The cross section for $\mu\gamma$ depends on the strength of the electric field of the nucleus which caused the scattering. Therefore the $\mu\gamma$ scattering probability was proportional to Z^2 of the target and therefore was strongly target dependent. Since saturation of the nuclear cross section ratio was expected to be observed in the low x_{Bj} region, which was equivalently low Q^2, removal of this background was critical. To do this, electromagnetic clusters must be identified in the ECAL. The method used will be discussed below.

4.4.2 Separating Hadron and Electron Clusters in the Calorimeter

Before the calorimeter could be used to distinguish between hadron clusters and electron clusters, it was necessary to construct a reasonably clean a sample of both. Elastic muon-electron scattering and $\mu\gamma$ scattering occurred in well defined kinematic regions where they predomi-

nated. By making restrictive kinematic cuts, a sample of events which were $\mu\gamma$ or μe^- were separated from a sample of DIS events.

Once these samples had been defined, the calorimeter response to the hadrons in the DIS sample was compared with the response to electrons and photons. Through this comparison, a method was derived to separate the background events from DIS scattering in the kinematic region where the two overlap.

The cleanest sample of deep inelastic sample occurred in the region of low y_{Bj} and high Q^2. Conversely electromagnetic background events occurred in the high y_{Bj}, low Q^2 region. Another property of these background events was their low track multiplicity. Muon-electron scattering produced a single high energy electron, muon-bremsstrahlung produced a single high energy photon. Photons produced no tracks in the detector, but traversed the target material in which pair production was possible. Although pair production occurred, the resulting multiplicity was still less than 5-10 hadrons typically produced in deep inelastic scattering. By taking advantage of differences in multiplicity and kinematics, reasonably clean data sub-samples were defined. The final electron and DIS (hadron) sample cuts are defined below:

$$\text{Electron Candidate} \equiv (Q^2 < 0.4) \text{ and less than 3 Fitted Tracks} \tag{4.5}$$

$$\text{DIS Candidate} \equiv (Q^2 > 1.5) \text{ and more than 4 Fitted Tracks} \tag{4.6}$$

For any event which passed the definitions outline above, if there was a forward spectrometer

track which impacted the calorimeter within 10 cm of a cluster, the track and cluster information was examined. The track-cluster requirement limited this study to hadrons and electrons; no conclusions about photons was derived from this study. Since the calorimeter was 20 radiation lengths and 0.2 interaction lengths, electrons deposited a larger fraction of their energy than hadrons. A measure of how much of the incident particle's energy was deposited in the calorimeter was the ratio of (Calorimeter Energy)/(Track Momentum). This ratio is shown in figure 4.17 for the electron sample and in figure 4.18 for the hadron sample.

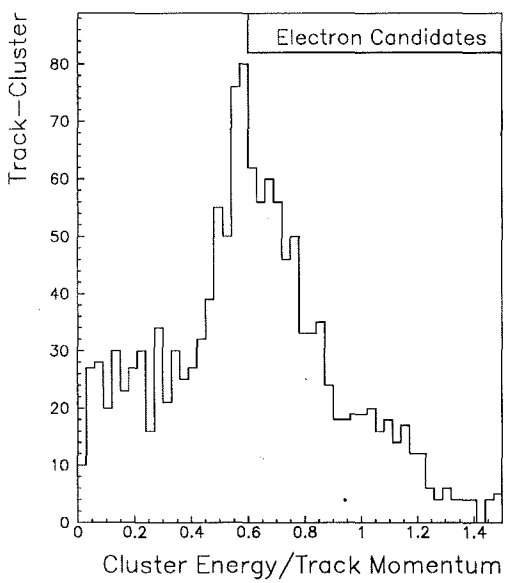

Figure 4.17: Eclus/Ptrack for Electrons

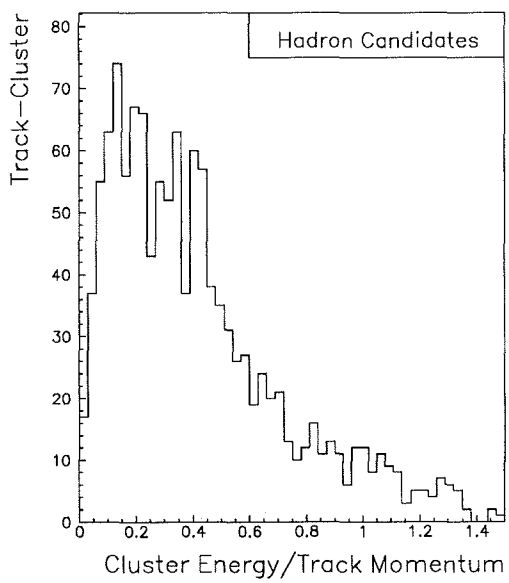

Figure 4.18: Eclus/Ptrack for Hadrons

Since cluster energy/track momentum was indicative of the type of particle which hit the calorimeter; figures 4.17 and 4.18 demonstrate the effectiveness of definitions 4.5 and 4.6. The separation between the two samples was not absolute; the contamination present indicates the

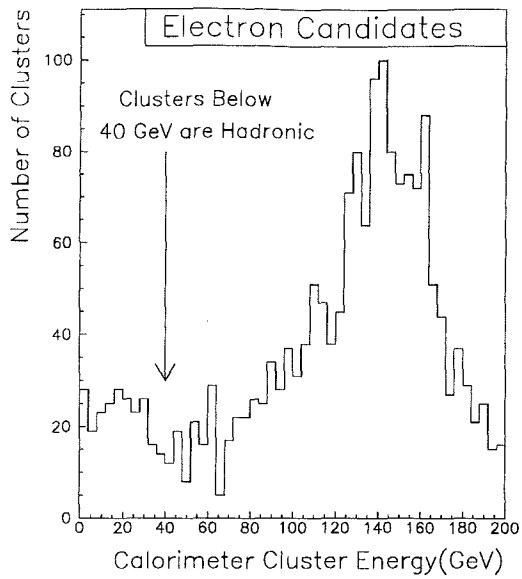

Figure 4.19: Cluster Energy from Electrons

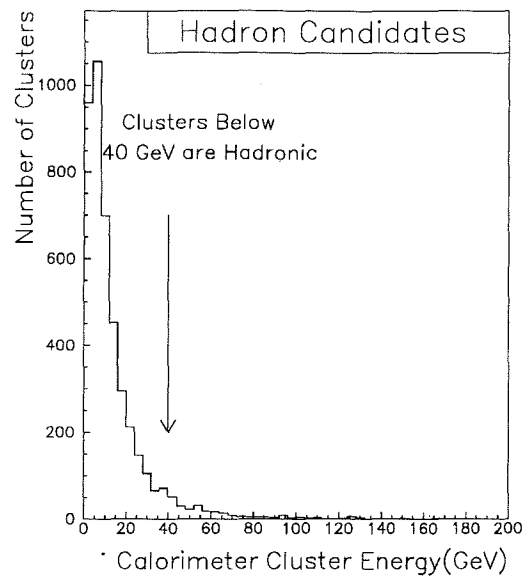

Figure 4.20: Cluster Energy from Hadrons

limits of defining background samples using kinematic cuts alone.

Figures 4.19 and 4.20 show the distribution of cluster energies for these two samples. A cut of 40 GeV was used to distinguish between a hadron and electron clusters. Since the distribution of hadronic clusters is peaked at low energy, very few real DIS event were rejected. The final electromagnetic background cut was to examine every calorimeter cluster in an event. If any cluster had an energy exceeding 40 GeV, the event was rejected.

4.4.3 Effectiveness of the Cal Cuts

In the previous section, track momentum was compared to calorimeter energy in order to identify electrons and hadrons. This analysis did not address photons produced from coherent muon

bremsstrahlung scatters. Additionally electrons from μe were required to have an associated calorimeter cluster. Implicit in the track-cluster analysis is the assumption that all electrons shower in the calorimeter. To measure the efficiency of the calorimeter cuts, a sample of muon-bremsstrahlung and muon-electrons scatters was defined independently of any calorimeter requirements. $\mu\gamma$ and μe scatters were identified by kinematic cuts and forward track multiplicity without any track-cluster requirements. An event was defined to be a muon-bremsstrahlung scatter if it met the following requirements:

i) Only two positively charged tracks fitted to the primary vertex

ii) No other tracks reconstructed in the event

iii) $y_{Bj} > 0.3$

The requirement on the number of tracks reconstructed restricts the event sample to those events in which only the incident and scattered muon were observed. The y_{Bj} cut removed deep inelastic scatters in which tracking inefficiency caused low track multiplicity to be reported. In figure 4.21A the distribution of the $\mu\gamma$ sample is plotted against x_{Bj}, figure 4.21C shows their y_{Bj} distribution. As expected these events are peaked in the low x_{Bj}, high y_{Bj} region. Figures 4.21B and 4.21D show the resulting distributions after all events which had any calorimeter cluster of greater than 40 Gev were removed. The initial bremstralung sample contained 5346 events. After the calorimeter cut was applied, only 49 events remained. Therefore the efficiency

of removing these events was:

$$\epsilon(\mu\gamma) = 1 - \frac{(\mu\gamma \text{which pass cal cut})}{(\mu\gamma)} = 1 - \frac{49}{5346} = 99.1\% \tag{4.7}$$

The elastic muon-electron scattering sample was defined as:

i) Only two positively charged tracks fitted to the primary vertex

ii) Only one negatively charged track fitted to the primary vertex

iii) No other tracks reconstructed in the event

iv) $y_{Bj} > 0.2$

v) $y_{Bj} < 0.7$

vi) $Q^2 < 0.5012$

Figures 4.22A and C show the x_{Bj} and y_{Bj} distribution of these events. Figures 4.22 B and 4.22 D show the results of removing every event in which a cluster of greater than 40 GeV was detected in the calorimeter. Only 78 out of the original sample of 4164 events survive the calorimeter cuts. Thus, the efficiency of removing these events was:

$$\epsilon(\mu e) = 1 - \frac{(\mu e \text{ which pass cal cut})}{(\mu e)} = 1 - \frac{78}{4164} = 98.1\% \tag{4.8}$$

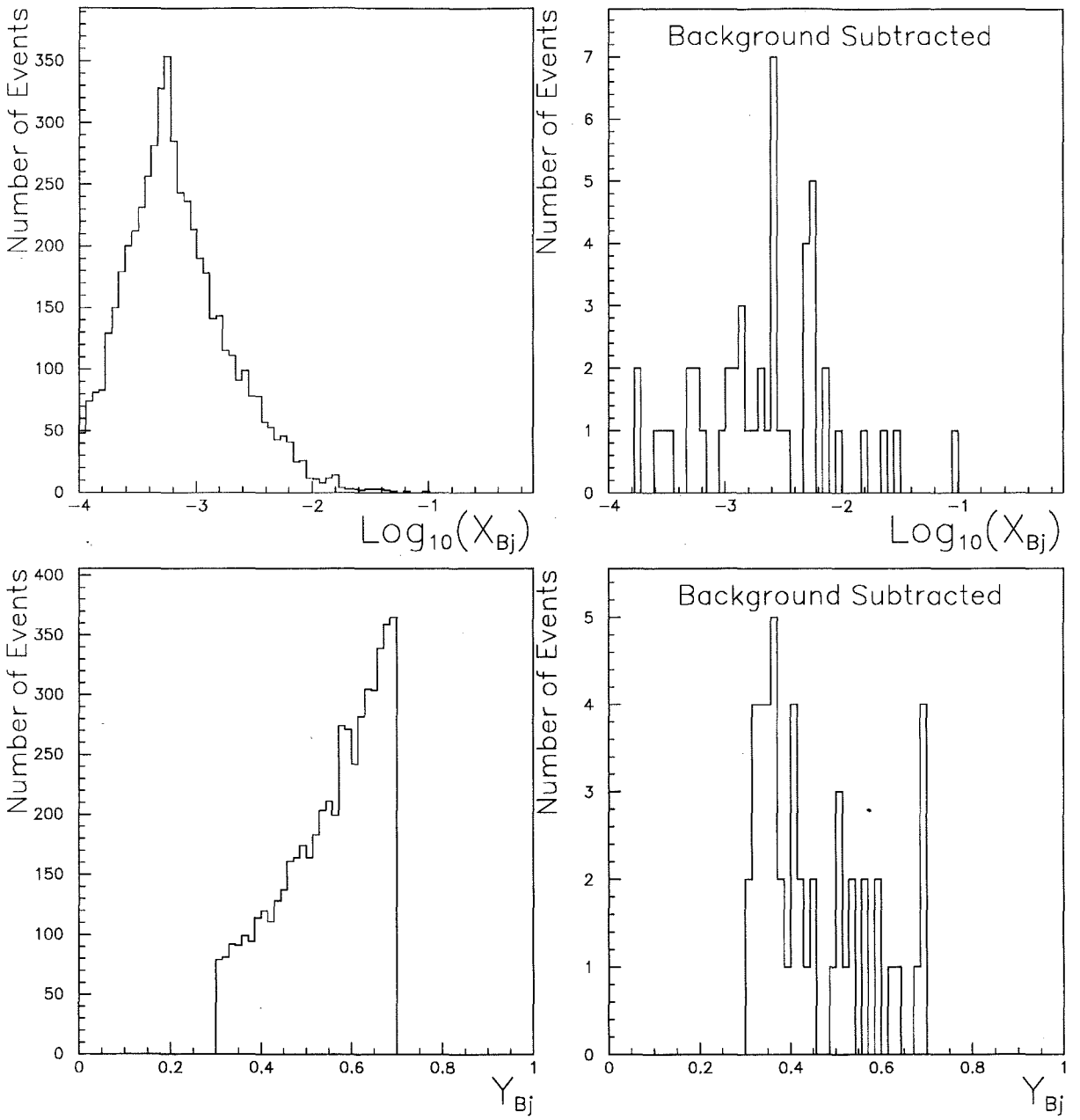

Figure 4.21: Identifying Muon Bremsstrahlung Using ECAL

In figure 4.23 the x_{Bj} distribution is shown for deuterium, carbon, calcium and lead targets. The distribution before the application calorimeter cuts is denoted by solid circles. The hatched histogram is the distribution after the calorimeter cut was imposed. The large spike at low x_{Bj} is due mainly to elastic μe^- scatters. Muon bremsstrahlung is the broader enhancement at $x_{Bj} < 0.01$ and is more pronounced in the lead and calcium targets due to the charge of their nuclei.

4.4.4 DIS Event Topology

As a final demonstration of background removal, the spatial distribution of the calorimeter clusters was studied. Previous analyses used event topology to distinguish between electromagnetic background and DIS events (8). In particular, μe^- and $\mu\gamma$ tend to occur in a plane defined by the incident and scattered muon trajectories. A quantity called "planarity"(P), defined as:

$$P \equiv \frac{(P_\mu \times P_{\mu'}) \cdot P_\gamma}{|P_\mu||P_{\mu'}||P_\gamma|} \tag{4.9}$$

is a measure of the energy flow out of the muon scattering plane. Here $P_{\mu,\mu'}$ are the 3-momenta of the incident and scattered muons and P_γ is the 3-momentum of a hypothetical bremsstrahlung photon constructed from the scattering vertex and the position of the most energetic calorimeter cluster. No cut based on planarity was applied in this analysis. However this quantity is useful in illustrating the robustness of cluster threshold cut.

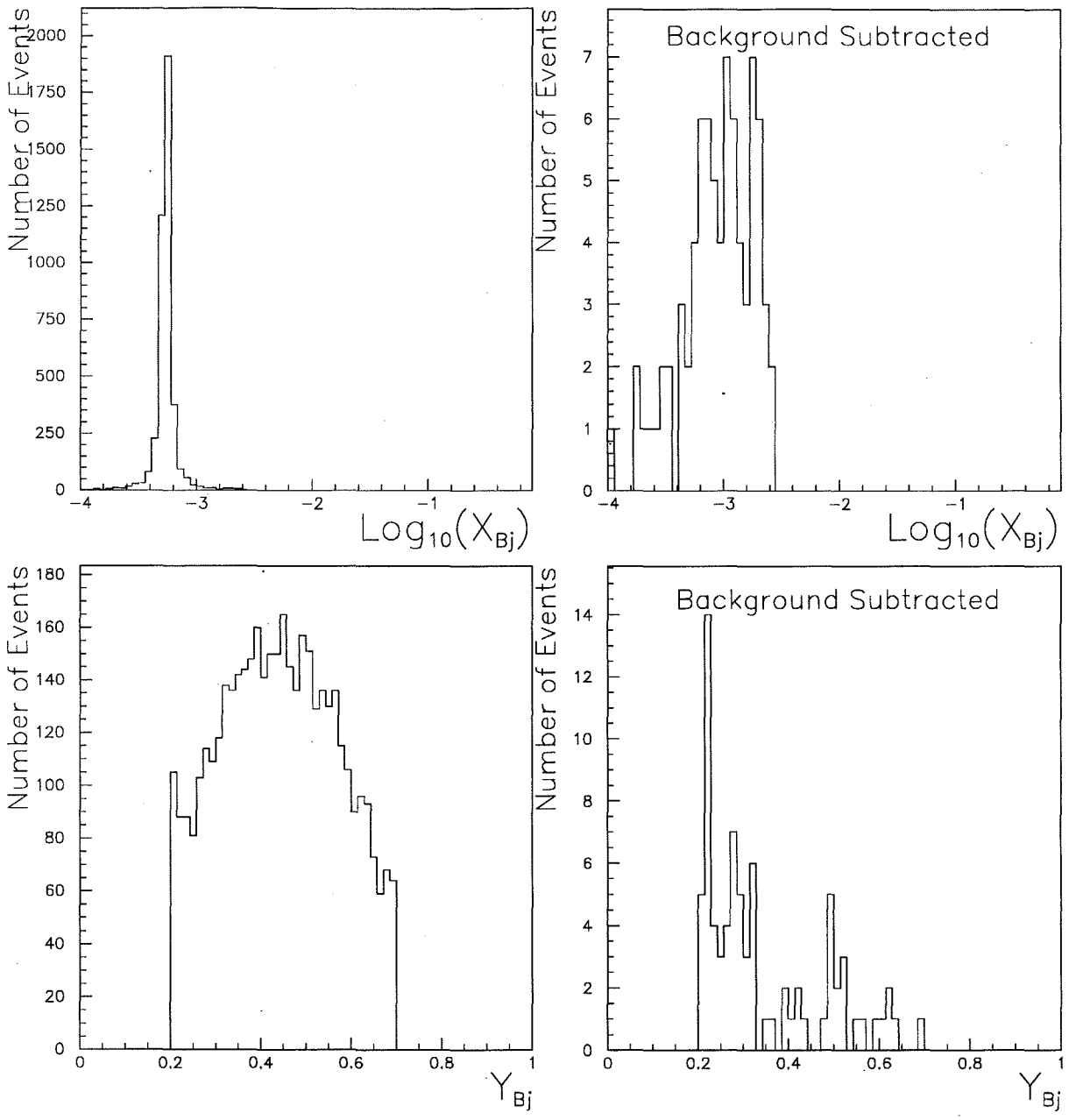

Figure 4.22: Identifying Elastic Muon-Electron Scattering Using ECAL

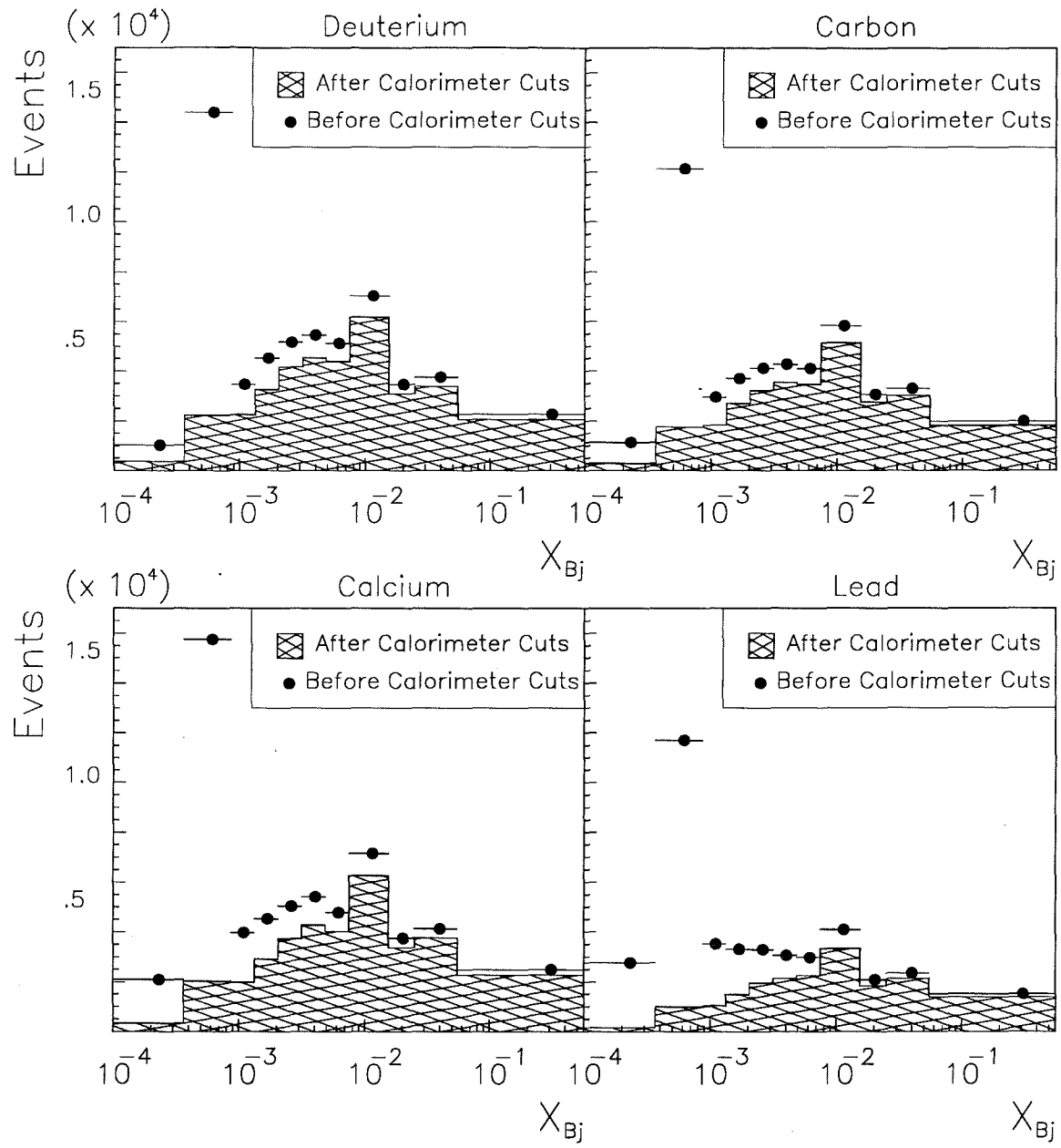

Figure 4.23: x_{Bj} Distribution Before and After Calorimeter Cuts

Figure 4.24 shows the distribution of planarity. In the planarity distribution there are two clearly observable peaks. The peak in the region of lower planarity are scatters which have a calorimeter cluster which is nearly colinear with the incident or scattered muon. This quantity was formed only for those events in which at least 1 calorimeter cluster was found. Events which had no energy deposited in the calorimeter were assumed to be DIS events. In figure 4.25 the planarity distribution is plotted for events which pass the previously defined calorimeter cut. The planarity distribution for high multiplicity scatters is superimposed on figure 4.25 as a shaded histogram. The high multiplicity events have in excess of 2 negatively charged or 4 positively charged tracks attached to the muon-muon vertex and are hypothesized to be DIS events. The shaded histogram has been multiplied by a factor of 6 in order to allow for comparison of the shape of the two distributions.

4.5 Minimum ν

A minimum ν of 50 GeV was required. Figure 4.26 shows the fractional error on ν. Imposing a resolution cut on x_{Bj} indirectly restricts the resolution in ν to be better than 20%. Hypothetically, a muon which had scattered with ν of 40 GeV could have been reconstructed with an error as big as 8 GeV. Had this been a $\mu\gamma$ event, it would have passed the 40 GeV calorimeter cut and been identified as a DIS event. By imposing a minimum ν cut of 50 GeV, electromagnetic background processes which involved small energy transfers could be identified with the 40 GeV

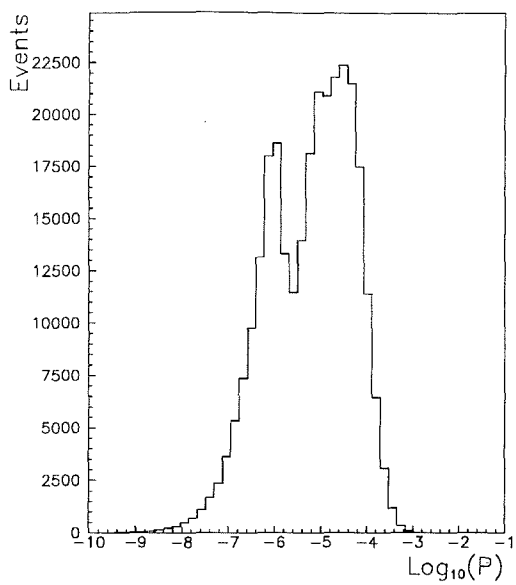

Figure 4.24: Planarity

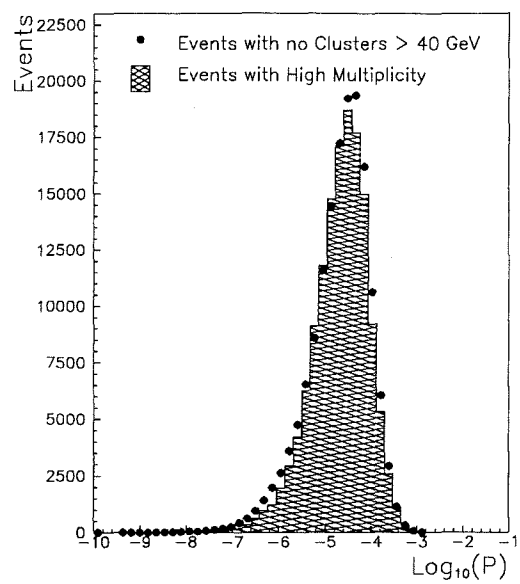

Figure 4.25: Planarity Comparing DIS Cuts

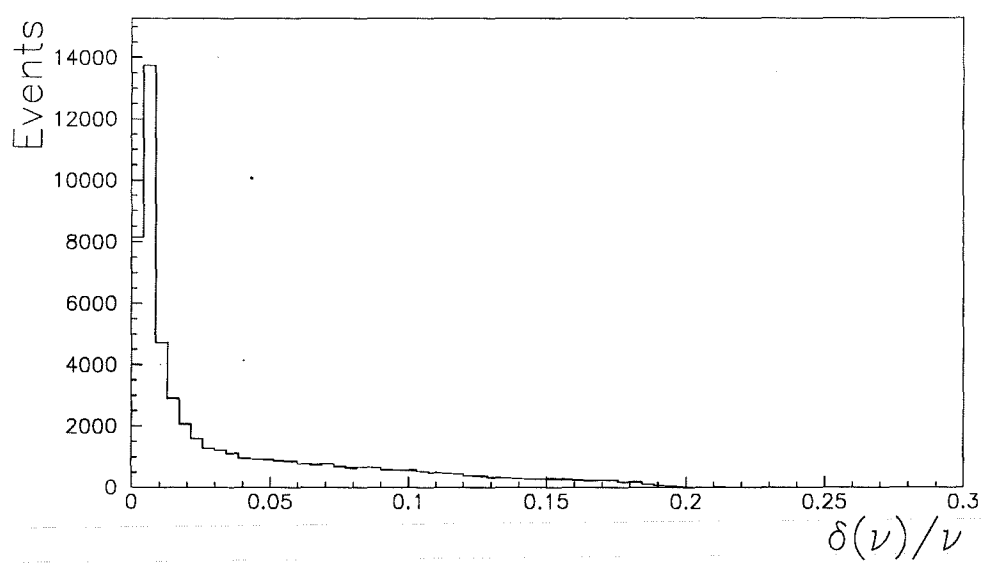

Figure 4.26: Fractional Error on ν After x_{Bj} Resolution Cuts

calorimeter cut.

4.6 Muon Reconstruction

Every scattered muon's position was determined at each trigger plane. If the muon's X-Y coordinate fell inside the veto window defined by the SAT, the event was rejected from further analysis. A large fraction of these events were spurious triggers. These triggers were caused by an electronic reflection introduced by the beam signal splitter panel. The reflection resulted in the SAT veto window being incorrectly determined and caused the SAT to trigger on unscattered muons.

An event was also rejected if it was identified as having been pattern recognized using the ray trace match algorithm(See Muon Match section). These muons were formed from forward spectrometer tracks which were not fully reconstructed. The kinematic resolution of these tracks was poor due to the lack of either drift chamber or PSA hits needed to constrain the track.

4.7 Summary

Cuts were applied to the events selected by the PAW Ntuples which were used in this analysis. Bad runs were defined by; unstable calorimeter response, incorrectly aligned chambers, inability to cross check normalization triggers or improper target cycling. After the bad runs were

TABLE XIII: Final Event Statistics

	SAT	RSAT Per Prescale Run Period	
Target	Events	II	III
^{2}D	36030	58915	24751
^{12}C(Thin)	2547	0	6090
^{12}C(Thick)	29585	26529	12370
^{40}Ca	34993	51266	22117
^{208}Pb	18712	82898	63521
Empty Ca	190	7322	13061
Empty Solid	233	21030	6460
Empty D	410	28186	6595

removed, cuts were applied to eliminate spurious triggers and events with poorly reconstructed. A final cut was derived to remove non-DIS backgrounds. The number of events which passed all the analysis cuts including the calorimeter cuts appears in table XI.

5. CORRECTIONS TO RAW EVENT YIELDS

5.1 Raw Event Distributions

The cuts described in Chapter 4 removed backgrounds and poorly reconstructed muons, but did not account for differences in beam flux, target density or empty target scatters. In this chapter these corrections will be discussed. The systematic uncertainty in the cross section ratios will also be estimated.

In figure 5.1 the uncorrected x_{Bj} distributions are presented. Final ratios presented in figure 5.13 had bins which were chosen to be broader in the low x_{Bj} and high x_{Bj} regions in order to minimize the measurement uncertainty due to low bin population. Included in figure 5.1 are the empty target data and half density carbon distributions which will be used to correct the raw distributions. The solid circles are the distributions before the calorimeter threshold cut was applied. The shaded band is the distributions after the calorimeter was used to remove μe

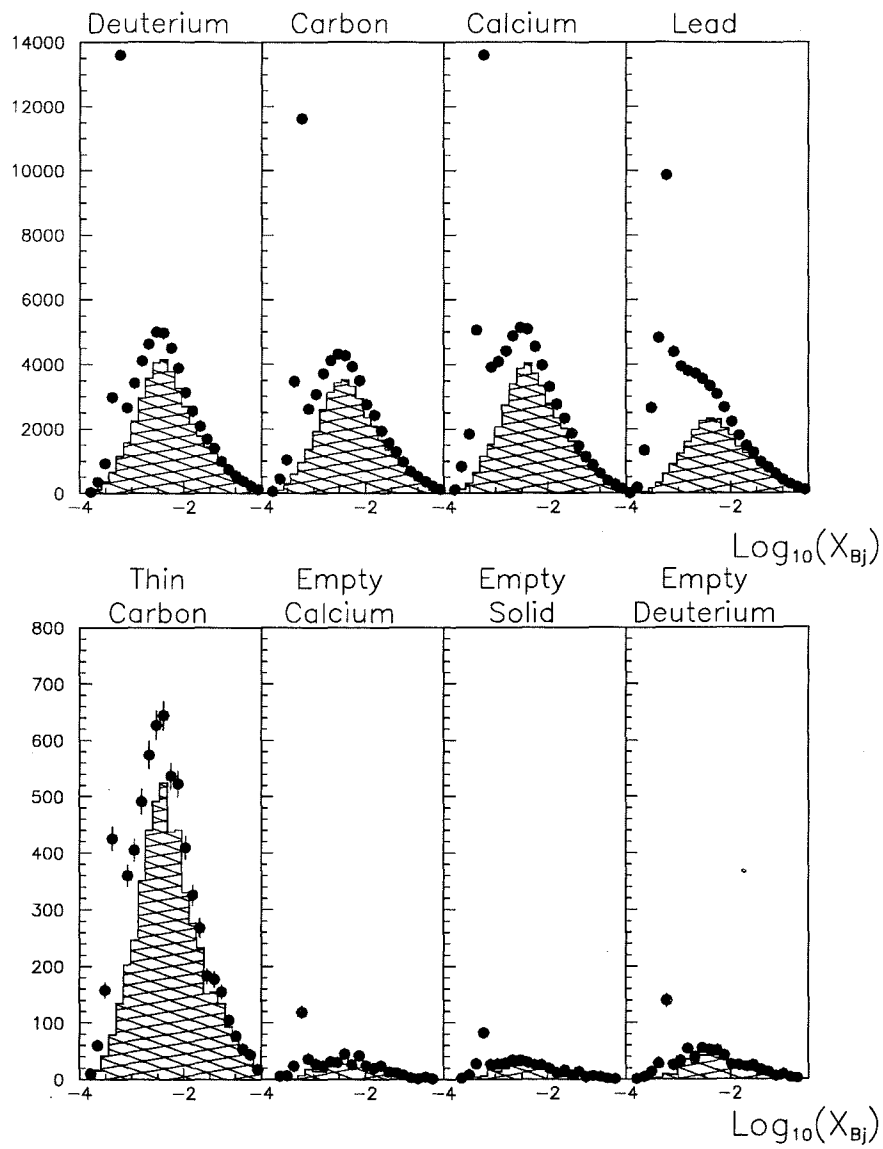

Figure 5.1: $\mathrm{Log}_{10}(x_{Bj})$ Before and After CAL Cuts

and $\mu\gamma$ backgrounds. The difference in the two distributions demonstrates the magnitude of the electromagnetic background events in our data. The signal to noise ratio in the bin which included elastic muon-electron scatters is as high as 1:18 in lead.

5.2 Normalization

The cross section for a given process is related to the number of interactions and beam luminosity by:

$$\sigma = \text{Number of Interactions}/\mathcal{L}. \tag{5.1}$$

In fixed target experiments, luminosity, $\mathcal{L}$, is the product of beam flux and the number of scattering centers which are exposed to this flux. The number of scattering centers is proportional to a target's density, so our luminosity is the product of target density and beam flux. Since this analysis is concerned with cross section *ratios*, it will suffice to measure the relative luminosity of each target with respect to deuterium.

5.2.1 Solid Target Densities

The carbon, calcium and lead targets were weighed, and with knowledge of their dimensions, densities were calculated. Target densities for the solid target were presented in table II. All solid target densities have been determined to better than 0.2%.

5.2.2 Liquid Deuterium Density

Although the density of the liquid deuterium target was measured indirectly, the procedure for doing so was straightforward (63). The vapor pressure of the evaporated deuterium liquid at the liquid-vapor boundary was measured. Then, with knowledge of the relationship between temperature, pressure and density for liquid deuterium, the density of the liquid was calculated.

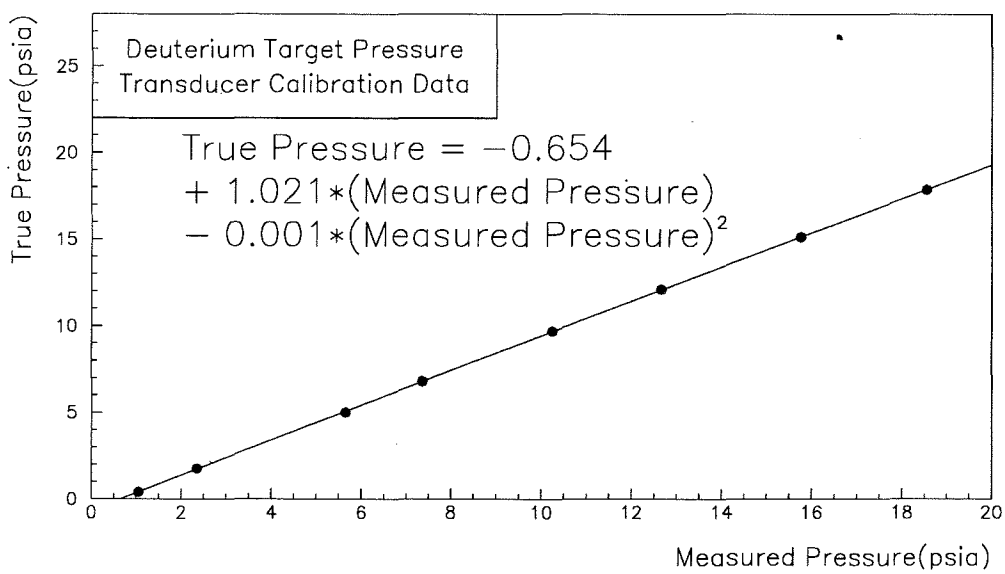

Figure 5.2: Deuterium Pressure Transducer Calibration

A correction was applied to the reported target pressure before target density was calculated. Calibration of the target pressure transducer showed it to have been reporting pressures with a slight offset (64). Figure 5.2 shows the result of calibration and the parameterization which was used to correct the measured values. The corrected vapor pressure was translated into

deuterium density using the following relation (65):

$$\begin{aligned}\text{Density}(\text{g/cm}^3) &= 0.27922 - (.22528 \times 10^{-1}) \times \text{pressure(psia)} \\ &\quad +(0.14804 \times 10^{-02}) \times (\text{pressure(psia)})^2 \\ &\quad -(0.33142 \times 10^{-04}) \times (\text{pressure(psia)})^3 \end{aligned} \tag{5.2}$$

Ideally one would like to determine the density of the deuterium target on a spill-by-spill basis. In the 1990 run, target density information was obtained from the Fermilab Cryogenics Group which had kept independent records of the target density. The deuterium vapor pressure was measured and recorded every 30 minutes throughout the run.

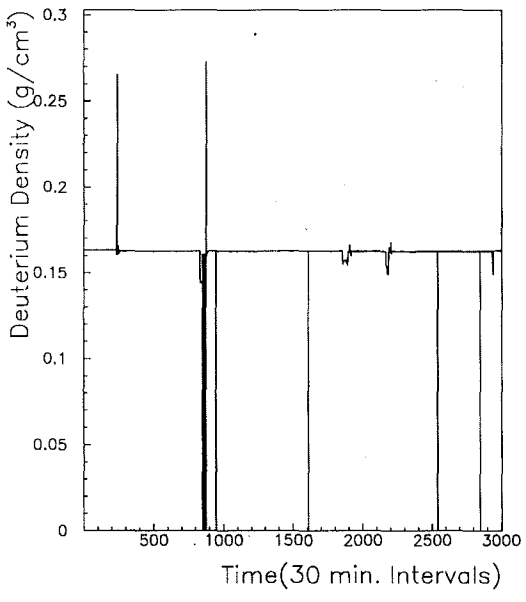

Figure 5.3: Deuterium Density Verses Time

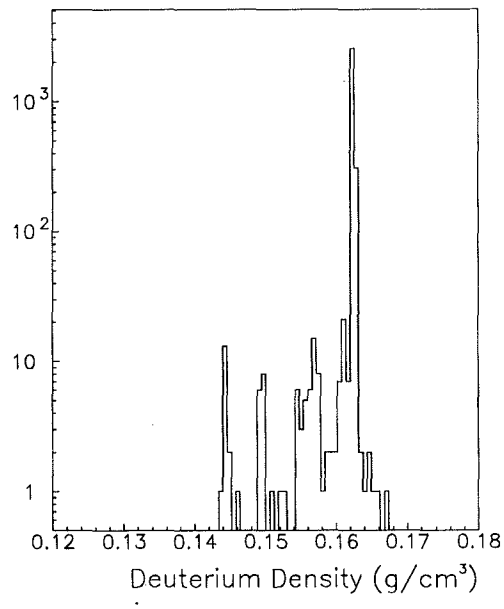

Figure 5.4: Deuterium Density

Figure 5.3 shows the deuterium density as a function of time for the run90 data taking period.

Plotted in figure 5.4 is the distribution of those densities. The variation in the target density was required to be within 1% of the nominal value of 0.1625 g/cm^3. The time and date of every measured density which varied by more than 1% was used to identify the run blocks during which the fluctuation had occurred. These fluctuations were caused by the deuterium target vessel being emptied, during which no deuterium data were taken. The time dependence and distribution of target densities after having removed the runs which exhibited large fluctuations appear in figures 5.5 and 5.6.

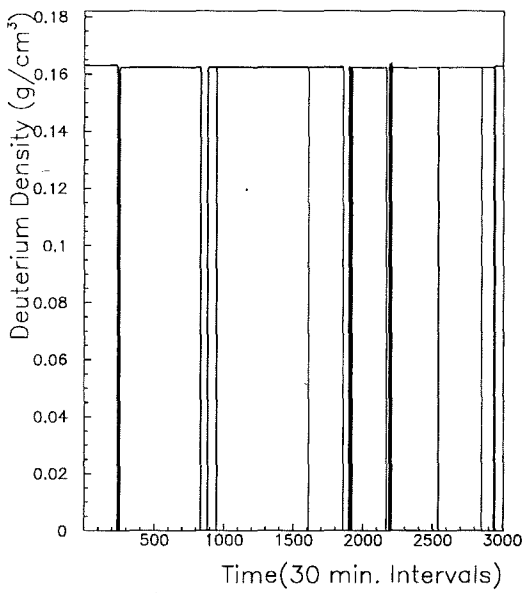

Figure 5.5: Corrected Density Verses Time

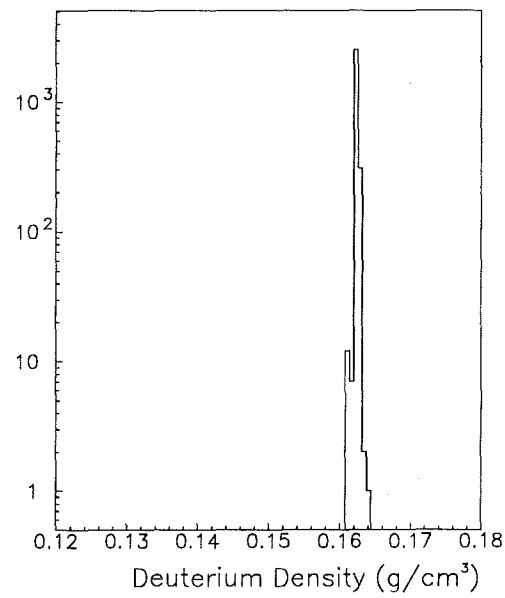

Figure 5.6: Corrected Density

To calculate the density per unit area, the density was multiplied by the length of the liquid deuterium. The length of the vessel was determined by dissecting the cryogenic target after the completion of the run. The target was 99.13 $\pm$ 1.4 cm long. The ends of the target were rounded

in order to provide mechanical strength to the flask. The rounded endcaps were responsible for the rather large uncertainty in the target length. The combination of the 1% density error and 1.4% target length error leads to a 1.72% uncertainty in the areal density of the deuterium.

5.3 Beam Flux

Muon beam flux was determined by two independent methods. As discussed previously, the method chosen for determining the beam flux was that of counting randomly prescaled beam triggers. Cuts which were applied to the incident muon for the SAT triggers were also required on the normalization sample. Since it was impossible to apply these cuts to the scalers, RSAT triggers were used to account for differences beam flux. The spill scalers were used solely to check the prescaling.

Prescaler Validation

Some validation of the RSAT prescaling was discussed in Chapter 4. In order to validate the method of prescaling, beam flux measured by the RSAT triggers was compared to the flux measured by the spill scalers. It was assumed that the two methods of measuring beam flux were independent.

The comparison was based on the results of gaussian fits to the RSAT/spill scaler ratio before quality cuts were applied to the RSAT sample. The ratios were fit in order to determine the

mean values and widths of the distributions. Table X, in Chapter 4, contains the results of comparing the two methods. Based on the mean value of the gaussians, the two agree to within 1%.

Target Dependence

In order to search for any possible target dependent effects, the validation of the RSAT beam flux measurement was carried out for each target separately. Again, a gaussian fit was performed on the RSAT/spill scaler distribution. The results exhibited broadening of the distribution which was consistent with larger statistical fluctuations, however, the two methods agreed to within 2% for each target. The results of the fits appear in table XIV. All bad runs had been removed before forming the ratios.

TABLE XIV: Target Dependence of Beam Flux Measurements

Target	Prescale Value	Mean	Width	Prescale Value	Mean	Width
Deuterium	2^{18}	0.998	0.063	2^{19}	1.007	0.1061
Thin Carbon	2^{18}	N/A	N/A	2^{19}	1.001	0.1205
Thick Carbon	2^{18}	0.988	0.082	2^{19}	0.995	0.1103
Calcium	2^{18}	0.998	0.078	2^{19}	0.988	0.0817
Lead	2^{18}	0.983	0.051	2^{19}	0.992	0.0471
Empty Ca Can	2^{18}	0.996	0.128	2^{19}	1.022	0.0919
Empty Solid Holder	2^{18}	0.993	0.091	2^{19}	1.004	0.1274
Empty Deuterium	2^{18}	1.017	0.137	2^{19}	0.994	0.1307

No significant target dependence was observed. The accuracy of the flux measurement was

estimated from the mean of the ratio. These mean values indicate a 2% systematic uncertainty in the beam flux measurement.

Beam Reconstruction

As a final check of the normalization, the cuts which were applied to the splitbeam tapes were studied. Cuts were applied to the splitbeam sample in order to remove multi-muon events, poorly reconstructed beam muons and spurious triggers. A file separate from the PAW Ntuples was written with a run-by-run accounting of the rejected RSATs for each target. Approximately 14% of all RSAT triggers were rejected by the quality cuts applied to the splitbeam tapes. The rate at which RSAT's were rejected was found to be independent of the target to less than 0.3%.

5.3.1 Normalization Uncertainty

The systematic error associated with the relative luminosity was estimated based on the accuracy with which the beam flux and target densities were measured. Target densities were determined to 0.02%, 0.004% and 0.2% for the carbon, calcium and lead targets and 1.72 % for the deuterium target. The beam flux measurement has a 2% error associated with it and is the dominant source of error. The quality cuts applied to the splitbeam sample rejected beams from different targets equally to within 0.3%. The error associated with the interfile event loss was discussed in Chapter 4, an error of 0.53%, 0.08%, 0.26% and 0.4% was assigned to the deuterium, carbon, calcium

and lead targets respectively. The quadratic sum of all the quoted errors results in a fractional error in luminosity of 2.71%, 2.02%, 2.02% and 2.07% for the deuterium, carbon, calcium and lead targets respectively. Combining these errors results in an systematic uncertainty of 3.4% in the overall normalization of the cross section ratios.

5.4 Empty Target Subtraction

The E665 target assembly contained material which induced muon scatters in addition to the nominal nuclear target interactions. The effect of these scatters, termed "empty target" scatters, was measured and a correction applied to the data. Materials in the target included; air, the stainless steel cans which encased the calcium targets, the vessel which the deuterium was held and a G10 fiberglass window which was located downstream of the targets.

5.4.1 Empty Target Distributions

Empty target data were taken as a normal component of the target cycle. The deuterium target was an evacuated flask constructed identically to the vessel which held the deuterium. Empty solid target data were taken by rotating empty target holders into the beam. Since the calcium targets were encased in stainless steel in order to prevent oxidation, a single stainless steel can was positioned in the beam in order to estimate its empty target scatters.

Figure 5.7 shows the distribution of vertices along the beam line for full and empty targets

of deuterium, calcium and lead. The empty target distributions for carbon were identical to lead and omitted from figure 5.7. The G10 window and empty stainless steel can are denoted by arrows. The region between the upstream arrows included the stainless steel can, the arrows downstream bracket the G10 window. The normalization of the distributions in figure 5.7 is arbitrary.

Full analysis cuts were applied to the empty target events. The resulting distribution, N^{empty}, was subtracted bin-by-bin in x_{Bj} from the full target data, N^{full}.

$$N^{corrected}(x_{Bj}) = N^{full}(x_{Bj}) - \frac{RSAT^{full}}{RSAT^{empty}} N^{empty}(x_{Bj}) \quad . \quad (5.3)$$

The empty target data were scaled by the ratios of the RSAT triggers in order to correct for differences in beam flux. All events which scattered from the single empty calcium can were weighted by a factor of 5 in their x_{Bj} distribution. Events were defined as being an empty calcium scatter based on their vertex position being between (-12.7 meters < X vertex < -12.4 meters) (see figure 5.7).

Figure 5.8 shows the x_{Bj} distribution of scatters before(histogram) and after(solid circles) empty target subtraction. The plots on the right are the corrected to uncorrected ratios as a function of x_{Bj}.

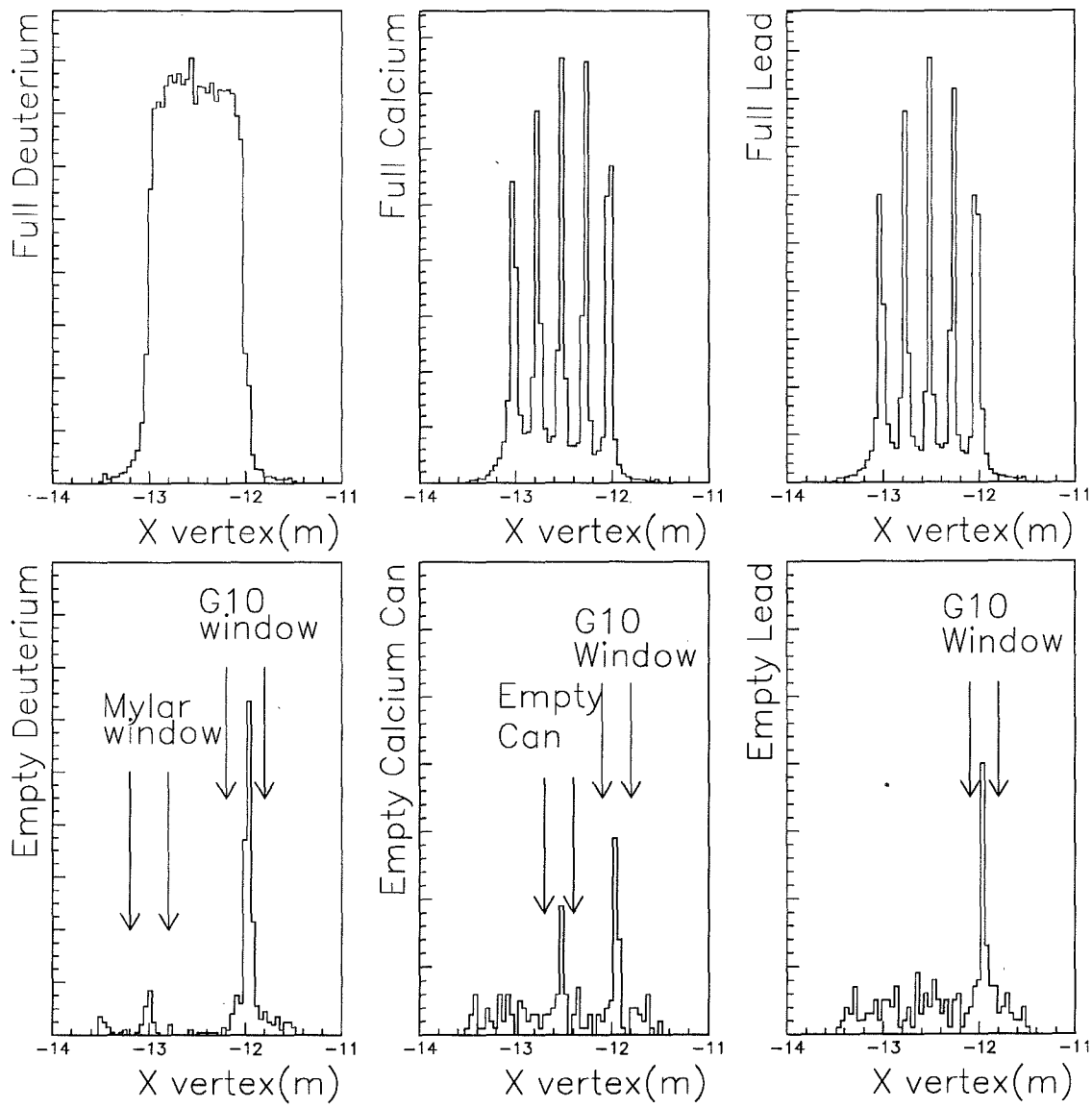

Figure 5.7: Vertex Distribution For Full And Empty Targets

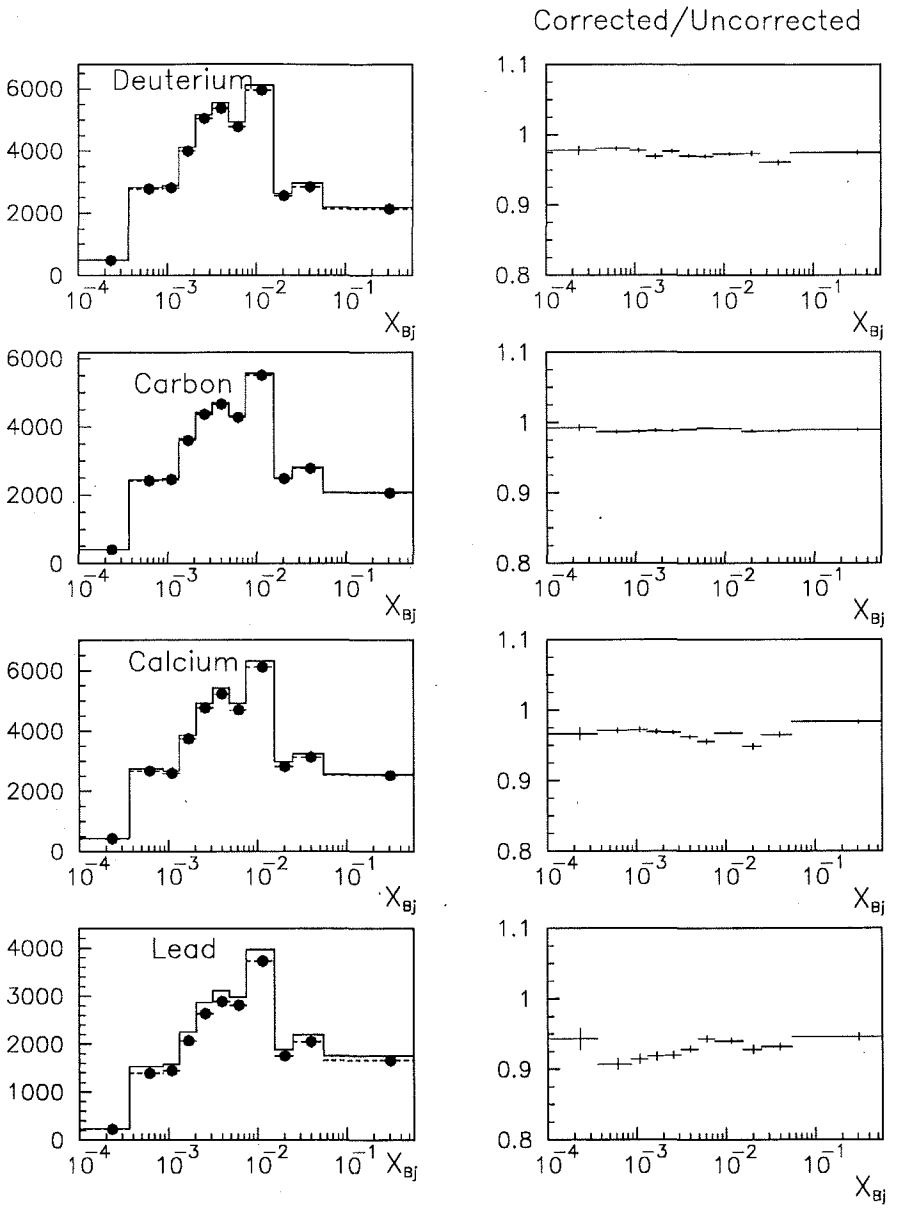

Figure 5.8: x_{Bj} Dependence of the Empty Target Correction

A Cross Check of the Empty Target Subtraction

In order to check empty target correction method, the ratios in figure 5.8 were compared with a calculation of the empty target correction. The areal density of the empty target materials was summed and divided by the nominal target density. In general, each target configuration introduced a different amount of material in the target region. Thus, the amount of material was calculated separately for each target, the results appear in table XV. The density of air was calculated assuming a temperature of 20° at 1 atmosphere of pressure. The empty deuterium target vessel was evacuated so 1.0 meter of air was included in its empty target calculation compared to 2.0 meters for the solid targets. The stainless steel can's material was approximated using the density of iron. The deuterium target vacuum flask was constructed of mylar and insulated with Rohacell.

TABLE XV: Empty Target Material For Each Target Configuration

	Areal Density(g/cm^2)			
Material	^{2}D	^{12}C	^{40}Ca	^{208}Pb
Air	0.120	0.241	0.241	0.241
G10 Fiberglass	0.134	0.134	0.134	0.134
Stainless Steel Cans	0.000	0.00	0.197	0.00
Vacuum Window(Mylar)	0.025	0.00	0.00	0.00
Target Flask(Mylar)	0.071	0.00	0.00	0.00
Rohacell	0.178	0.00	0.00	0.00

The measured empty target corrections were approximated by fitting the ratios presented

in figure 5.8 to a flat line. The results of the fits appear in table XVI labelled as "measured correction". The measured empty target corrections were compared to the "expected" empty target correction. The expected correction was determined by the ratios of full to empty target density, labelled "Empty/Full" in table XVI. The total empty target contribution listed in table XVI is the sum of the densities listed in table XV. The difference in the expected and measured corrections was found to be less than 1%.

TABLE XVI: Calculated and Measured Empty Target Corrections

Target	Target Density (g/cm^2)	Empty Target (g/cm^2)	Empty/Full	Measured Correction	Difference (%)
^{2}D	16.109	0.528	0.0327	0.0270	0.57
^{12}C	29.952	0.375	0.0125	0.0110	0.15
^{40}Ca	19.497	0.572	0.0293	0.0324	0.31
^{208}Pb	5.370	0.375	0.0698	0.0687	0.11

5.5 Target Density Effects

Because of the nature of the measurement which was made, targets of different interaction and radiation lengths were compared. We assume than the observed differences are due solely to the physics of the underlying interaction. Implicit in this assumption is that macroscopic target properties such as radiation length and interaction length do not alter the measured ratios. Hypothetically, downstream reinteractions or multiple coulomb scattering could affect the scattered muon reconstruction or acceptance. In the following section a measurement of

these effects will be presented.

5.5.1 Thin to Thick Carbon Comparison

The effect of target rescattering was measured by comparing the x_{Bj} distributions for different thicknesses of the same target material. In run90 data were taken with carbon targets of two different thicknesses. Since the targets were identical in every respect except for areal density, by comparing these, the effect of having material downstream of the interaction was estimated.

The half density carbon data were taken during the later run blocks in run90. In order to eliminate any time dependent effects, the target density study was restricted those run blocks during which both targets were exposed to the beam. All analysis cuts were applied to both targets. Bin-by-bin empty target subtraction was applied and the ratios was corrected for muon flux using RSAT triggers.

Figure 5.9 shows the fully corrected cross section ratio $\mathrm{R}(x_{Bj}) = \sigma_{\text{thin carbon}}/\sigma_{\text{thick carbon}}$. The reduced χ^2 was calculated assuming no effect and reported in the box. A fit was also performed assuming the form:

$$\mathrm{R}(x_{Bj}) = a + bx_{Bj} \tag{5.4}$$

The resulting fit parameters were $a = 0.9512 \pm 0.0234$ and $b = 0.1125 \pm 0.2870$, with a reduced χ^2 of 0.722. Since in both cases the ratio was consistent with unity to within our normalization uncertainty, no corrections were applied to the nuclear target cross section ratios.

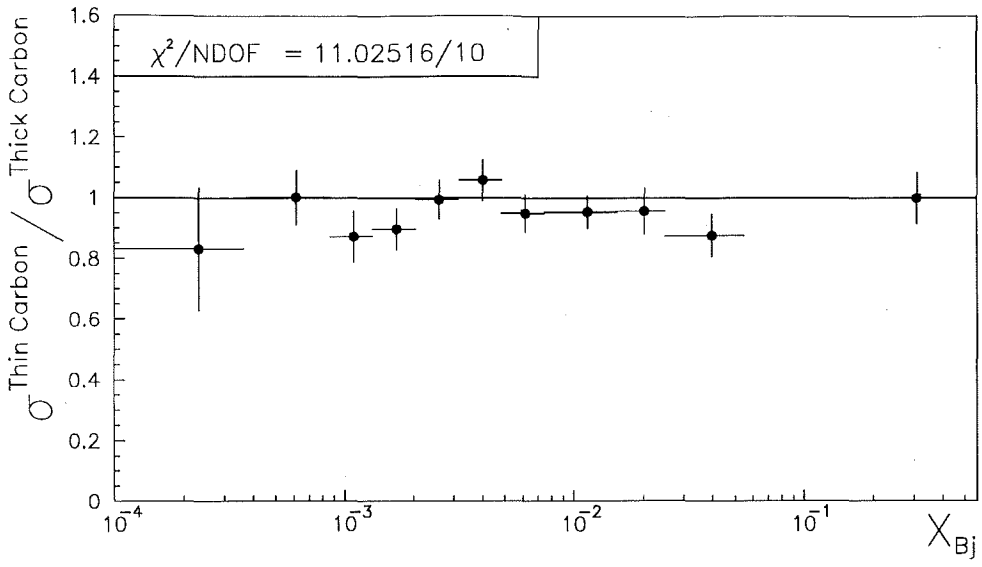

Figure 5.9: x_{Bj} Cross Section Ratio of Thin to Thick Carbon

5.5.2 SAT Self-Vetos

One property which characterizes deep-inelastic scattering is the production of final state hadrons. In order to determine the rate at these hadrons passed through the SSA counters and vetoed an event, a "monitor "trigger, SATPS, was devised. The SATPS was identical to the SAT trigger in every respect except for the SSA veto plane(See Trigger Section). By eliminating the upstream veto plane from the trigger, the rate of hadron vetos in the SAT trigger could be measured.

An "SAT self-veto" event was defined as an event in which a hit in the SSA hodoscope vetoed the event. Additionally, it was required that the SSA hit was not associate with the scattered muon. Therefore, in determining which events were self-vetoes, hodoscope hits and scattered

muon tracking information was employed.

Figure 5.10A shows the position of the muon track, for SAT triggers only, at the X plane which corresponds to the SSA. The box denotes aperture of the SSA hodoscope counters. Figure 5.10C is the same distribution for those muons which were self-veto candidates. Clearly there is an enhancement in the self-veto sample inside the edge of the veto aperture. The multiple scattering of the muons due to the hadron absorber is shown in figures 5.10B and 5.10D. Multiple scattering was determined by comparing the slope of the muon track before and after the steel:

$$MS = \left(\frac{\Delta \mathrm{Y}}{\Delta \mathrm{X}}\right)_{\mathrm{LSTF}} - \left(\frac{\Delta \mathrm{Y}}{\Delta \mathrm{X}}\right)_{\mathrm{LPRO}} \tag{5.5}$$

where $(\Delta \mathrm{Y}/\Delta \mathrm{X})$ is the difference in slope of the track projected into the Y-plane. LSTF and LPRO refer to the track formed upstream and downstream of the absorber respectively.

The enhancement in the multiple scattering distributions at MS$\sim$-0.001 indicates that the self-veto selection was biased towards events which passed through the SSA counter but scattered away from the veto window behind the steel. In order to eliminate this bias, an additional cut was imposed on the position of the muon at the veto hodoscope. The cut removed the region of enhancement:

$$0.05 < \mathrm{Y_{SSA}} < -0.1 \text{ AND} - 0.003 < \mathrm{Z_{SSA}} < 0.02 \tag{5.6}$$

Figure 5.11B shows Y verses Z of the muon tracks with the additional cut applied. Notice

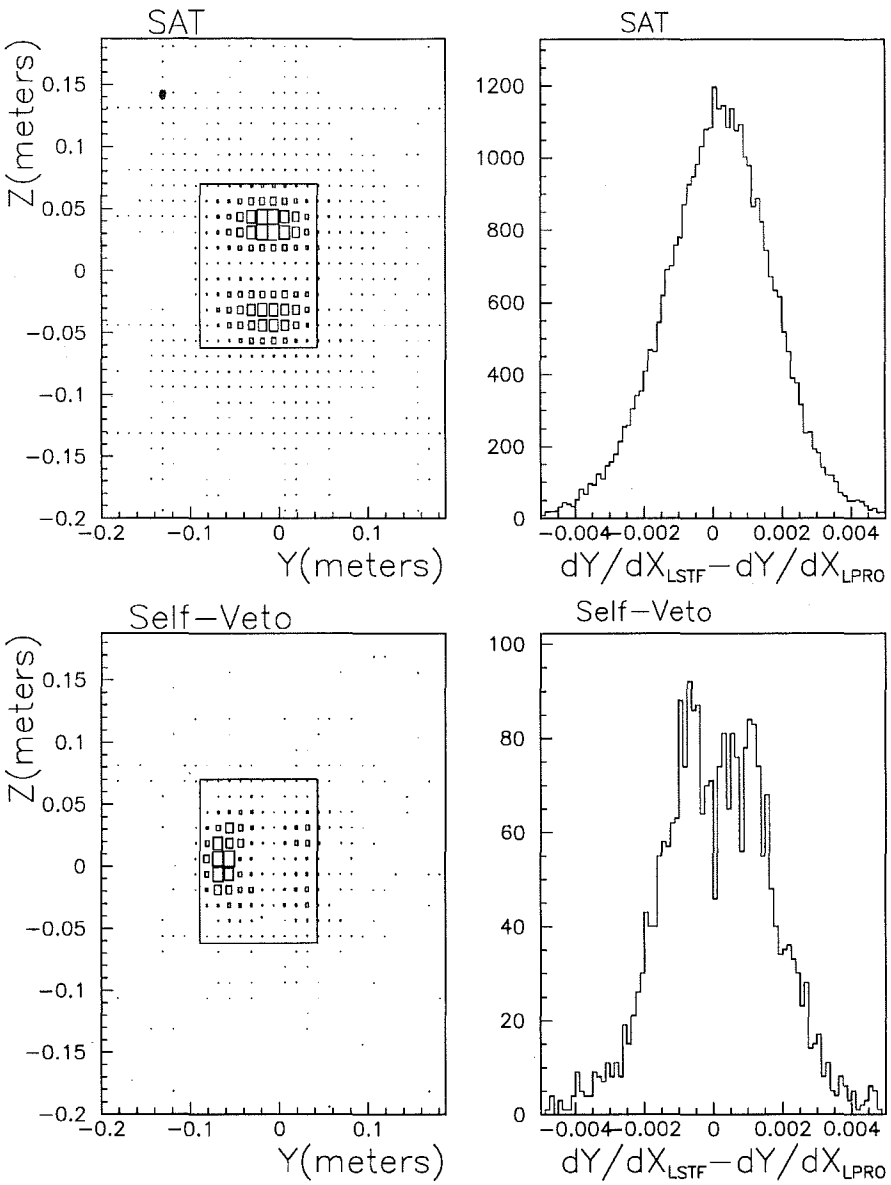

Figure 5.10: Muon Topology for SAT Self-Veto Candidates

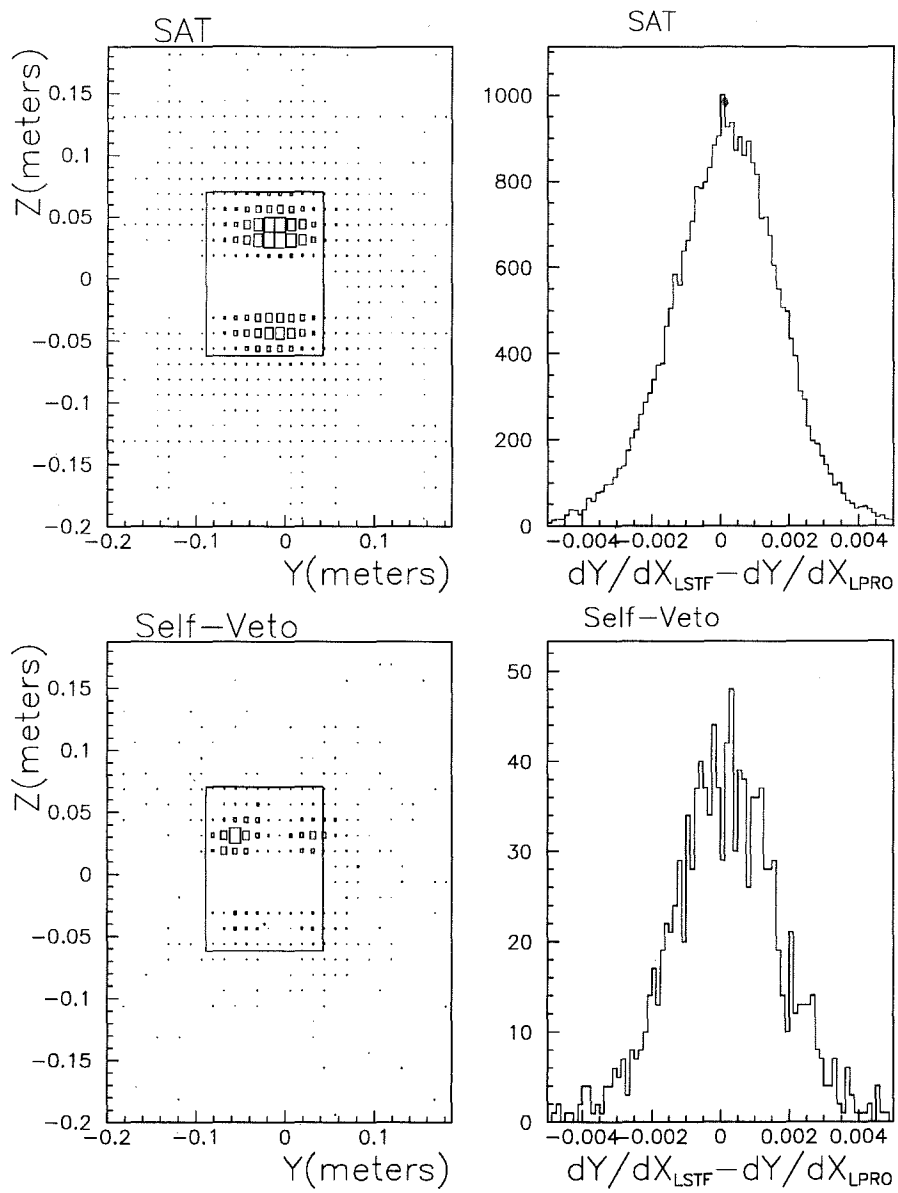

Figure 5.11: Muon Topology Final Self-Veto Sample

that the self-veto multiple scattering distribution now reproduced the SAT multiple scattering distribution, indicating the trigger bias has been removed.

Once the final self-veto sample was defined, full analysis cuts were applied to both SAT and self-veto events. The x_{Bj} dependence of the self-veto's was defined as:

$$\text{Self Veto Rate}(x_{Bj}) \equiv \text{SAT Self Veto}(x_{Bj})/\text{SAT}(x_{Bj}) \tag{5.7}$$

The self-veto rate was determined for each target separately. Because the SATPS trigger used an identical beam as the SAT trigger, normalization and empty target corrections cancel automatically.

Since the data for the self-veto study was limited, the distributions suffered from large statistical fluctuations. Therefore, the x_{Bj} bins were chosen to be more coarse than the bins used in the cross section ratios. The $\text{Log}_{10}(x_{Bj})$ of the self-veto rate was approximated by the exponential form:

$$\text{Self Veto Rate}(x_{Bj}) = \exp\left[A + B \times \text{Log}_{10}(x_{Bj})\right]. \tag{5.8}$$

The results of fitting each targets self-veto rate to equation 5.8 appears in the following table.

These results indicate a strong dependence on x_{Bj}. The x_{Bj} dependence of the veto rate could have been guessed at knowing that the mean multiplicity in μN scattering is approximately logarithmic in ν. The SAT self-veto rate reached a maximum in the lowest x_{Bj} bin where ν reached values of 200 GeV. The mean multiplicity of charged tracks in the self-veto sample was

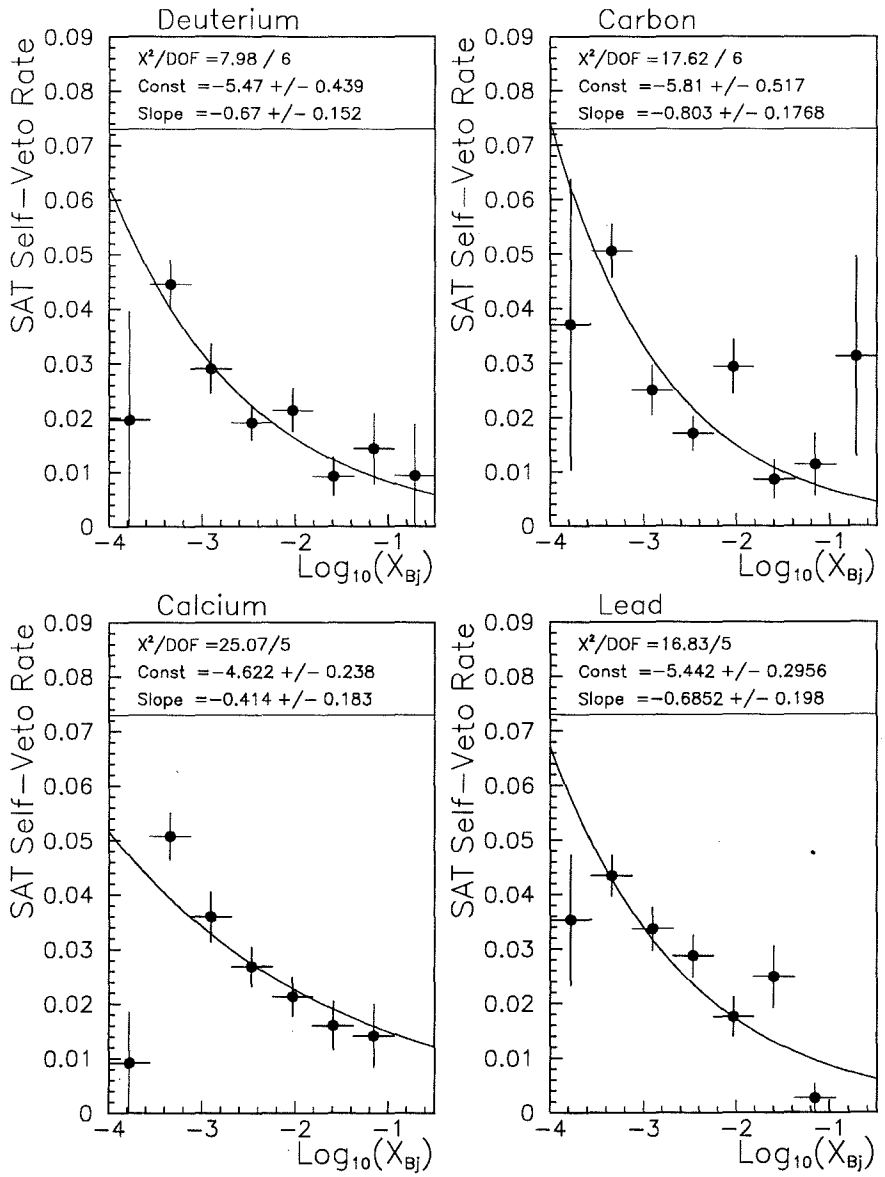

Figure 5.12: SAT-Self-Veto Rate As a Function of x_{Bj}

TABLE XVII: Fits to the SAT Self-Veto Rate Verses x_{Bj}

Target	χ^2/DOF	A	B
Deuterium	7.98 /6	-5.47 $\pm$ 0.44	-0.675 $\pm$ 0.152
Thin Carbon	2.90 /5	-6.34 $\pm$ 0.98	-0.956 $\pm$ 0.329
Thick Carbon	17.62/6	-5.81 $\pm$ 0.52	-0.803 $\pm$ 0.177
Calcium	25.07/5	-4.62 $\pm$ 0.24	-0.414 $\pm$ 0.183
Lead	16.83/5	-5.44 $\pm$ 0.30	-0.685 $\pm$ 0.197

4.23, the SAT mean multiplicity was 4.24.

The size of the self-veto rate reached as high as 8% in the region of $x_{Bj} < 0.0001$, however, the target-to-target differences were negligible.

SAT Self-Veto Systematic Error

A correction was not applied to the cross section ratios based on the self-veto analysis. Instead, a systematic error was assigned to each bin which parameterized the self-veto effect. The systematic error was determined by forming fully corrected cross section ratios and comparing to an identical measurement which included an SAT self-veto correction. The correction was found to be small, and since the measured effect suffered from poor statistics, the uncorrected ratios will be presented as the result. The method of applying the self-veto correction is described below.

Each scatter was assigned a weight based on the probability that there was a rejected self-

veto at the same x_{Bj}. The weights were intended to approximately "restore" the rejected self-veto scatters. The self-veto weight function, $w(x_{Bj})$, was used to connect "measured" x_{Bj} distributions to the "true" distributions. The "true" were the self-veto corrected distributions.

The measured scatters were related to the true scatters through the SAT self-vetos by:

$$\mathrm{N}^{measured}(x_{Bj}) = \mathrm{N}^{true}(x_{Bj}) - \mathrm{N}^{Self-Veto}(x_{Bj}) \tag{5.9}$$

with

$$\mathrm{N}^{Self-Veto}(x_{Bj}) = [\mathrm{Self-Veto\ Rate}(x_{Bj})] \times \mathrm{N}^{true}(x_{Bj}). \tag{5.10}$$

The exponential parameterization of the SAT self-veto as a function of x_{Bj} was used to determine the weight function $\mathrm{N}^{true} = w(x_{Bj}) \times \mathrm{N}^{measured}$.

$$w(x_{Bj}) = (1 - exp[\mathrm{A} + \mathrm{B} \times \mathrm{Log}_{10}(x_{Bj})])^{-1}. \tag{5.11}$$

The terms A and B are the target dependent parameters which were reported in table XVII. The weight function was applied to each scatter and full analysis cuts were applied to the resulting "true" x_{Bj} distributions. Cross section ratios formed from the "true" x_{Bj} distributions were compared to the "measured" ratios and found agree to better than 0.7% in at all x_{Bj}. The difference in the "true" and "measured" distributions were combined to determine the x_{Bj}-dependent relative error:

$$\epsilon_{self-veto}(x_{Bj}) = \frac{|\mathrm{R}_{true}(x_{Bj}) - \mathrm{R}_{measured}(x_{Bj})|}{\mathrm{R}_{measured}(x_{Bj})} \tag{5.12}$$

this error was added in quadrature to the terms described below.

5.6 Sensitivity to the Applied Cuts

The sensitivity to the applied cuts was used to estimate the systematic uncertainty in the ratios. The value of each cut was varied independently. Then, the fully corrected cross section ratios were formed and compared the the ratios formed with the nominal cuts. The difference between cross section ratios calculated with the cut " i " and the varied cut " i' " was calculated bin-by-bin in x_{Bj} for each cut:

$$\epsilon_i(x_{Bj}) = \left[\mathrm{R}_{i'}(x_{Bj}) - \mathrm{R}_i(x_{Bj})\right] / \mathrm{R}_i(x_{Bj}) \tag{5.13}$$

where $\mathrm{R}_i \equiv \sigma^{\mathrm{A}}/\sigma^{\mathrm{D}}$. The ϵ_i's are the relative error associated with the cut.

A Summary of the Cut Variation

The systematic error introduced by the software trigger requirement, y_{Bj}, ν, resolution and calorimeter cuts were studied. The requirement that the scattered muon satisfy a software simulation and the resolution cuts had very little effect on the ratios. The software trigger cut was removed in order to estimate its effect. All ratios differed by less than 1% in all x_{Bj} bins as a result of this cut. The x_{Bj} resolution cut, $\delta x_{Bj}/x_{Bj} < 0.2$ was varied from 0.15 to 0.25. The resolution differences were less than 2% for all ratios and in all x_{Bj} bins.

The maximum y_{Bj} cut was changed from 0.7 to 0.6 and 0.8. The difference in cross section ratios was most pronounced in the low x_{Bj} bins. The Pb/D ratio saw the largest difference

of 9%. The carbon and calcium ratios increased by 5% and 8% respectively. The minimum ν requirement was varied from 40 GeV to 70 GeV. This cut altered the ratios by less than 2% in the highest x_{Bj} bins.

Finally the cut on the energy of the calorimeter cluster which defined an electromagnetic background event was varied by 10% from 36 GeV to 44 GeV. The resulting cross section ratios differed from the nominal cut of 40 GeV by as much as 4% at low x_{Bj}. In addition, scatters with $0.00044 < x_{Bj} < 0.00064$ were explicitly removed to quanitify the 2% inefficiency for removing elastic muon-electron scatters. The effect was largest in the calcium to deuterium ratio, 3.5%, but less than 1% in carbon and lead.

The total systematic uncertainty was calculated by summing the relative errors in quadrature, assuming no correlation.

$$\Delta \mathrm{R}(x_{Bj}) = \sqrt{\Sigma_i \epsilon_i^2(x_{Bj})} \tag{5.14}$$

The resulting errors were as large as 13% in the very low x_{Bj} region($x_{Bj} < 0.0001$).

5.7 Fully Corrected Ratios

Figure 5.13 show the fully corrected cross section ratios for ^{12}C/D, ^{40}Ca/D and ^{208}Pb/D. The systematic error is represented by the shaded band at the bottom of the plot. Error bars represent statistical errors only. The 3.4% overall normalization error has not been included.

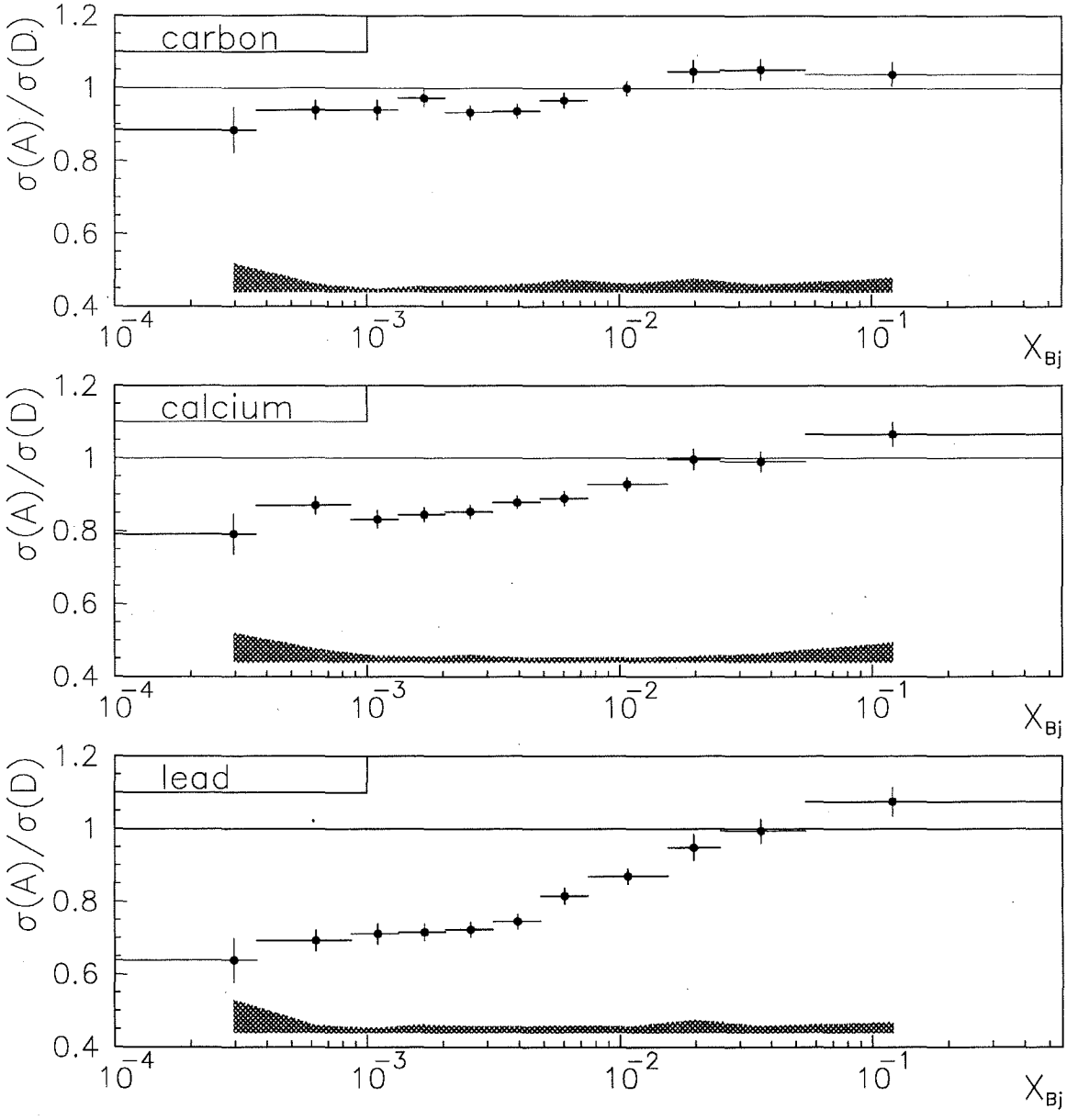

Figure 5.13: Fully Corrected Nuclear Cross Section Ratios

Several features of the data are obvious. First, all the ratios approach unity at $x_{Bj} > 0.1$. In the region above 0.1 there is an enhancement of 3-7% depending on the target. Below $x_{Bj} < 0.1$ the ratios exhibit "shadowing", that is, they lie below unity. The size of this depletion depends on the target; lead is more strongly shadowed than calcium and calcium is more strongly shadowed than carbon. Finally, as for x_{Bj} values less than 0.001 the shadowing becomes independent of x_{Bj}: the amount of shadowing has "saturated". The value of the ratio in the saturation region also depends on the target and is smallest for the heaviest nuclear target, lead.

5.8 Summary

The x_{Bj} distributions from targets of deuterium, carbon, calcium and lead were corrected for beam flux and empty target interactions. The resulting distributions were used to form the cross section ratios ^{12}C/D, ^{40}Ca/D and ^{208}Pb/D. The ratios exhibit shadowing at values of $x_{Bj} < 0.1$ and the amount of shadowing saturates below $x_{Bj} < 0.001$.

The x_{Bj} dependence of systematic uncertainty was estimated by varying the kinematic cuts independently. The uncertainty reaches a maximum value of 13% in the lowest x_{Bj} bin. Target length effects were measured using different thicknesses of the same target material and found to be consistent with having no effect. The SAT self-veto rate was defined and measured. The self-veto rate was as large as 8% and could be approximated by an exponential function of $\mathrm{Log}_{10}(x_{Bj})$. The effect was found to be independent of the target and therefore did not alter

the measure ratios.

6. COMPARISON WITH THEORY AND PREVIOUS RESULTS

Cross section ratios presented in Chapter 4 exhibit a systematic depletion in the region below $x_{Bj} \sim 0.1$. The size of the depletion is A-dependent and more pronounced in the heavier nuclear targets. The carbon to deuterium ratio shows the smallest depletion: approximately 5%. The lead and calcium ratios exhibit 15% and 30% shadowing respectively. In the region of very low x_{Bj}, below $x_{Bj} \sim 10^{-2}$, shadowing looses its dependence on x_{Bj}. This lack of x_{Bj} dependence has been termed "saturation" (8) and has previously been observed in the xenon to deuterium cross section ratio. This chapter will focus on the A-, Q^2-, and ν-dependence of shadowing, as well as the x_{Bj} dependence of saturation.

6.1 Saturation of Shadowing

In the following section the onset of saturation and cross section ratios in the saturation region will be discussed. A comparison will be made with theoretical predictions based on the gener-

alized vector dominance(GVD) interpretation of shadowing. Parton recombination(PR) models will be mentioned, although the validity of applying this model in the low Q^2 region where this analysis presents results is questionable (33).

6.1.1 The Onset of Saturation

The onset of the saturation of shadowing is the largest value of x_{Bj} at which cross section ratios are independent of x_{Bj}. In the GVD interpretation of shadowing, this is the region where the hadronic component of the photon has a lifetime which is greater than the nuclear radius. Parton recombination models explain saturation in terms of a delocalization of low x_{Bj} partons. In this view, saturation results from $1/x_{Bj}$ of a parton being large enough that it is associated the entire nucleus as opposed to a single nucleon.

In order to demonstrate that shadowing in nuclear cross section ratios saturate, an iterative procedure was used. The low x_{Bj} regions were fit to a flat line. First, the lowest two x_{Bj} bins were fit. Then the lowest three bins, and so on through all 11 bins. The reduced χ^2 was used to determine the "flatness" of the points. The largest bin with a χ^2/DOF less than 3 was defined as the bin in which the onset of saturation had occurred. In order to measure the saturation onset more precisely, this procedure was repeated with smaller x_{Bj} bins in the region where the onset of saturation was being observed.

The value of the "saturated ratios", $R_s(x_{Bj})$, was simply the value of the fit to bins 1 to N,

where N was the largest x_{Bj} bin in which the saturation condition was satisfied. The fit results appear in the following table. The reduced χ^2 was determined using the original binning, not the finer bins used in the onset measurement. Results indicate that the saturation region moved to lower values of x_{Bj} as the size of the nucleus increased. The x_{Bj} of the onset of saturation is plotted against atomic number in figure 6.1 and ratio at saturation is plotted against atomic number in 6.2. Both results exhibit a linear dependence on $\mathrm{Log}_{10}(\mathrm{A})$ indicating a power law dependence on A.

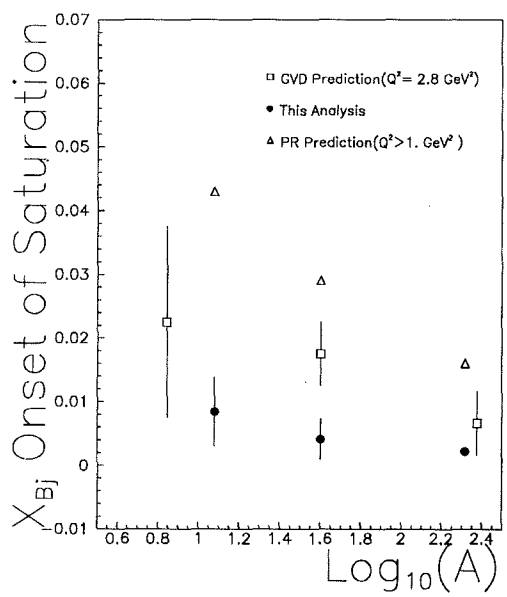

Figure 6.1: Saturation Onset vs Atomic Number

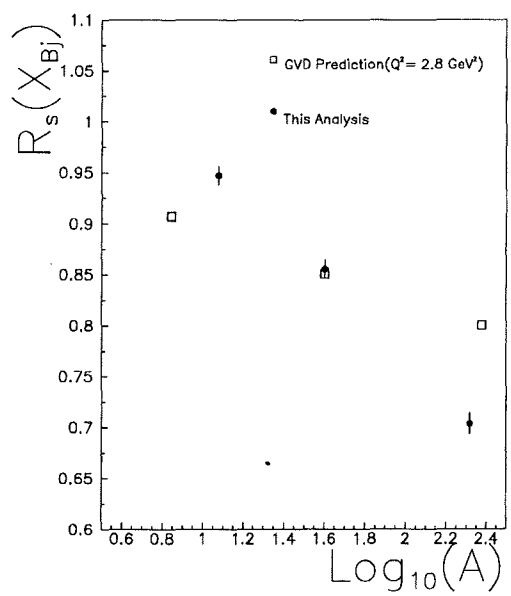

Figure 6.2: Saturation Ratio vs Atomic Number

TABLE XVIII: $R_s(x_{Bj})$:Nuclear Cross Section Ratio Saturation

Ratio	$R_s(x_{Bj})$	x_{Bj} Onset	χ^2/DOF
^{12}C/D	0.9471 ± 0.009	$0.0057 < x_{Bj} < 0.0111$	4.163/ 6
^{40}Ca/D	0.8550 ± 0.009	$0.0025 < x_{Bj} < 0.0057$	4.624/ 5
^{208}Pb/D	0.7033 ± 0.010	$0.0019 < x_{Bj} < 0.0025$	4.37 / 5

6.1.2 Comparison with Theoretical Predictions

Generalized Vector Dominance

In a paper by Bilchak,Schildkneckt and Stroughair (28) the saturation of nuclear cross section ratios was presented for fixed $Q^2 = 2.8$ GeV^2. The ratio $R(x_{Bj}) = F_2^A/F_2^D$ was plotted for A-values of 7, 40 and 238. The value of the onset of the saturation of shadowing was estimated and the results appear in figure 6.1 as empty boxes. The GVD points lie systematically higher than the data(solid circles) at all values of atomic number. The values of the $R_s(x_{Bj})$ in the saturation region appear in table XIX. The E665 $R_s(x_{Bj})$'s are included for comparison.

TABLE XIX: $R_s(x_{Bj})$ in the Saturation Region-Comparison with Theory

	Bilchak		This Analysis	
Target	$R_s(x_{Bj})$	Q^2	$R_s(x_{Bj})$	Q^2
^{7}Li	0.907	2.8 GeV^2	N/A	N/A
^{12}C	N/A	N/A	0.9471± 0.009	1.1 GeV^2
^{40}Ca	0.85	2.8 GeV^2	0.8550± 0.009	0.83 GeV^2
^{208}Pb	N/A	N/A	0.7033± 0.010	0.83 GeV^2
^{238}Ur	0.80	2.8GeV ^{2}	N/A	N/A

The calcium to deuterium saturation value, R_s, agrees with the measured saturation. However, based on this analysis, one might expected the lithium to saturate at with a higher $R_s(x_{Bj})$ and the uranium to saturate lower R_s than the predicted values. This would require the calculated saturation values to exhibit a more pronounced A-dependence.

The predicted ratios which were used for comparison were calculated at Q^2= 2.8 GeV^2. The E665 data in the region where $R_s(x_{Bj})$ were compared were much lower 0.5-0.8 GeV^2. To see how the difference in Q^2 may have skewed the comparison a second comparison was made. The Bilchak model also predicts how cross section ratios vary as a function of A-in different Q^2 ranges. An example has been reproduced in figure 6.3. It is apparent that as Q^2 decreases, the logarithmic dependence on atomic number becomes more pronounced. This trend disagrees with the A-dependence measured in this analysis, shown as a solid circle.

Parton Recombination(PR)

The parton recombination models predict the onset of of "complete" shadowing to occur at (34)

$$x_s \leq 0.1/\mathrm{A}^{1/3}. \tag{6.1}$$

This relation was not rigorously calculated, and the authors caution against interpreting results in the region $Q^2 < 1$ GeV^2. Results are included for the sake of completeness. Based on equation 6.1, one would expect saturation values for carbon, calcium and lead of 0.043, 0.029, and 0.016 respectively. These values have been included in figure 6.1 as empty triangles. These

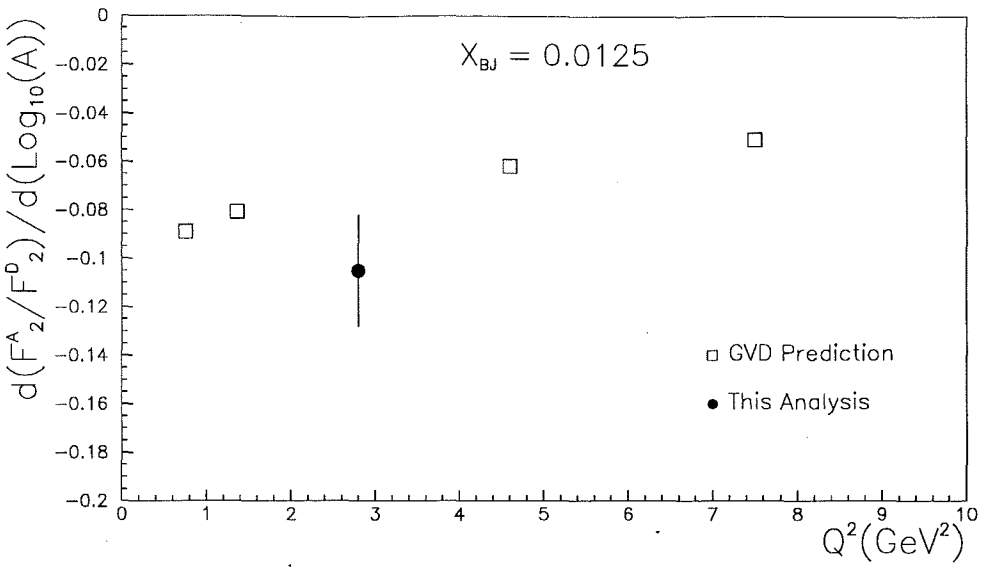

Figure 6.3: Comparison of the A-Dependence with a GVD Prediction

PR values lie systematically higher than both the GVD points and saturation onset measured in this analysis.

The only cross section ratio in this analysis which saturated in a region with $Q^2 > 1.\text{GeV}^2$ was that of carbon. The carbon saturation occurs in the region $0.006 \leq (x_s(^{12}\text{C})) \leq 0.011$ with a mean Q^2 of 1.2 GeV^2. Even in the region were the PR model claims validity, the predicted onset of "complete shadowing" occurs at a larger x_{Bj} than the measured value. Both the calcium and lead ratios saturate in the x_{Bj} region were the mean value of $Q^2 \sim 0.83\text{GeV}^2$ at $x_{Bj} \sim 0.006$.

Conclusions

In conclusion, neither GVD or PR model exactly reproduces the saturation result. Both models do however show qualitative agreement with this analysis-the shadowing in larger nuclei saturates at lower values of x_{Bj}. In comparison to both theoretical predictions some liberties were taken with Q^2 and A values. However, the GVD interpretation seems to be a better candidate for describing the E665 low x_{Bj}, low Q^2 region.

6.2 A-Dependence

The A-dependence of the cross section ratios were also studied in order to compare with theoretical predictions. The nuclear cross section ratio $\mathrm{R}(x_{Bj})$ was plotted against the logarithm of the atomic number. Figure 6.4 shows $\mathrm{R}(x_{Bj})$ verses $\mathrm{Log}_{10}(\mathrm{A})$ for each x_{Bj} bin. A straight-line fit to the points has been superimposed. The distributions are well reproduced by fits, indicating the ratios exhibit a power law dependence on atomic number. Each slope and error has been tabulated below. The values in table XX are represented graphically in figure 6.5. In the low x_{Bj} region the slopes are constant indicating the per nucleon cross section ratios obey:

$$\frac{\sigma^{\mathrm{A}}(x_{Bj})}{\sigma^{\mathrm{D}}(x_{Bj})} \sim \mathrm{A}^{-.2} \tag{6.2}$$

In the region above $x_{Bj} \sim 0.001$ where the shadowing effect dies away, the A-dependence becomes softer.

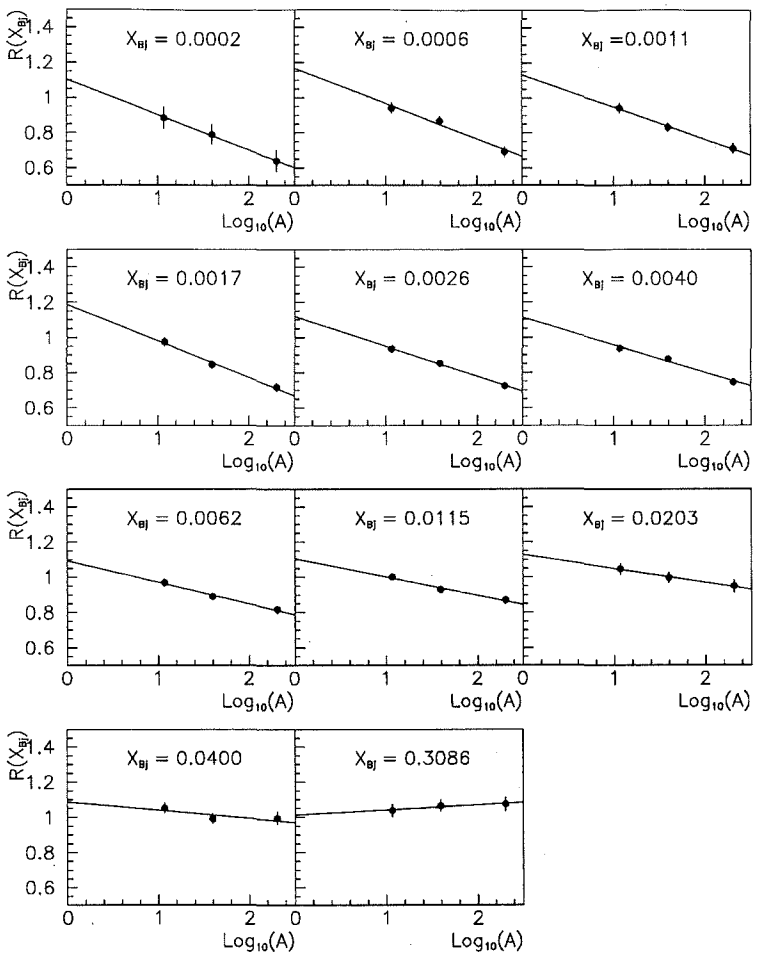

Figure 6.4: Logarithmic A-Dependence of Shadowing

Generalized Vector Dominance

The measured A-dependence was compared with results derived using the vector meson picture of shadowing. In the Bilchak paper the ratio

$$R(A) \equiv F_2^A / F_2^D \tag{6.3}$$

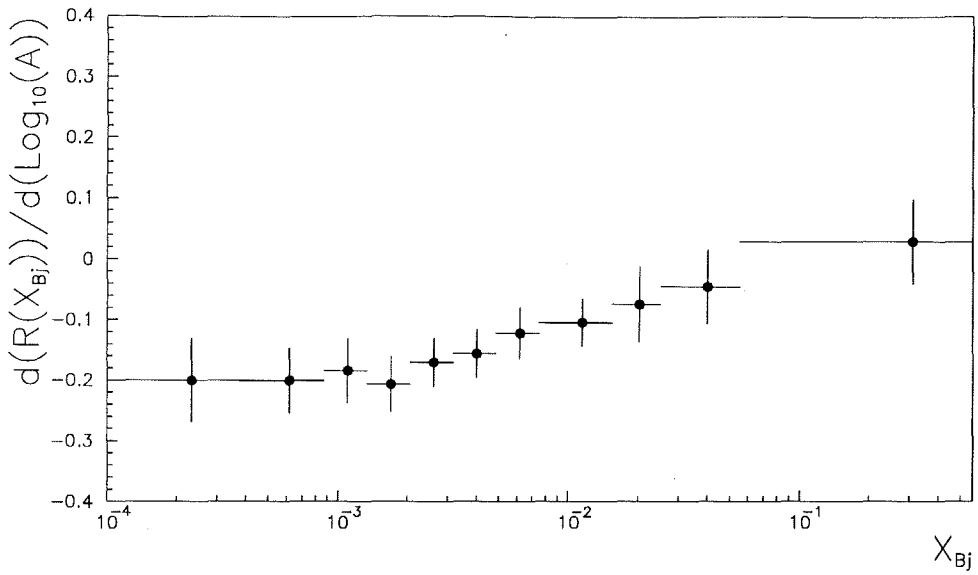

Figure 6.5: Logarithmic A-Dependence vs x_{Bj}

was presented. The ratio were calculated at fixed x_{Bj} for $Q^2 = 7.50\,\mathrm{GeV}^2, 4.6\,\mathrm{GeV}^2, 1.36\,\mathrm{GeV}^2$ and .7 In order to compare with our results, the mean Q^2 of our data was determined for the $x_{Bj}(= 0.0125)$ used in the Bilchak calculation. The mean Q^2 of E665 data a $x_{Bj} = 0.0125$ was 2.8 GeV^2, but values ranged from 0.3 GeV^2 to 10 GeV^2. The slope of R(A) extracted from the theoretical prediction are presented in figure 6.3 as a function of Q^2. Empty boxes are the Bilchak points, the solid dot is the corresponding E665 result. Clearly the prediction exhibits a much less pronounced A-dependence than what has been measured by E665.

Another prediction based on GVD was that of Piller and Weise (30). They predict the A-dependence to obey:

$$\sigma_{\mathrm{A}} \sim \mathrm{A}\sigma_{\mathrm{N}} \left[1 - \frac{3\sigma_{\mathrm{N}}}{8\pi \mathrm{r}_0^2} \mathrm{A}^{1/3}\right] \tag{6.4}$$

This form can be compared as

$$A_{eff}/A = \sigma_A/A\sigma_N \tag{6.5}$$

to the E665 results. The $A^{1/3}$ depends on $r_0 = 1.2\,\mathrm{fm}$ and σ_N, the single nucleon cross section. The E665 cross section ratios were again plotted against atomic number,"A", and a fit to $R(A) = \alpha - \beta A^{1/3}$ was performed in each x_{Bj} bin. The results appear in figure 6.6. The fit has been superimposed and results have been tabulated below. The range of Q^2 used in this calculation was $(0.6 < Q^2 < 10.)\mathrm{GeV}^2$, which overlaps the Q^2 values measured in this analysis.

TABLE XX: Statistical Analysis R(A) verses x_{Bj}

x_{Bj}	$R(A)=\alpha-\beta A^{1/3}$			$R(A)=\alpha \mathrm{Log}_{10}(A)$	
(bin center)	α	β	χ^2/DOF	α	χ^2/DOF
0.0002	1.026 ± 0.034	0.066 ± 0.008	0.098 / 3	-0.20±.07	0.02/1
0.0006	1.097 ± 0.015	0.069 ± 0.004	0.117 / 3	-0.20±.03	1.28/1
0.0011	1.058 ± 0.015	0.062 ± 0.004	1.35 / 3	-0.18±.03	0.12/1
0.0017	1.100 ± 0.013	0.067 ± 0.003	3.44 / 3	-0.21±.03	0.54/1
0.0026	1.054 ± 0.011	0.057 ± 0.003	0.867 / 3	-0.17±.02	0.16/1
0.0040	1.056 ± 0.011	0.053 ± 0.003	0.069 / 3	-0.16±.02	1.05/1
0.0062	1.043 ± 0.012	0.034 ± 0.003	1.44 / 3	-0.12±.02	0.26/1
0.0115	1.062 ± 0.011	0.034 ± 0.003	1.74 / 3	-0.11±.02	0.47/1
0.0203	1.097 ± 0.018	0.026 ± 0.005	0.295 / 3	-0.08±.03	0.05/1
0.0400	1.062 ± 0.173	0.014 ± 0.004	1.81 / 3	-0.04±.04	1.1/1
0.3086	1.026 ± 0.020	-0.009 ± 0.005	0.133 / 3	0.02±.04	0.07/1

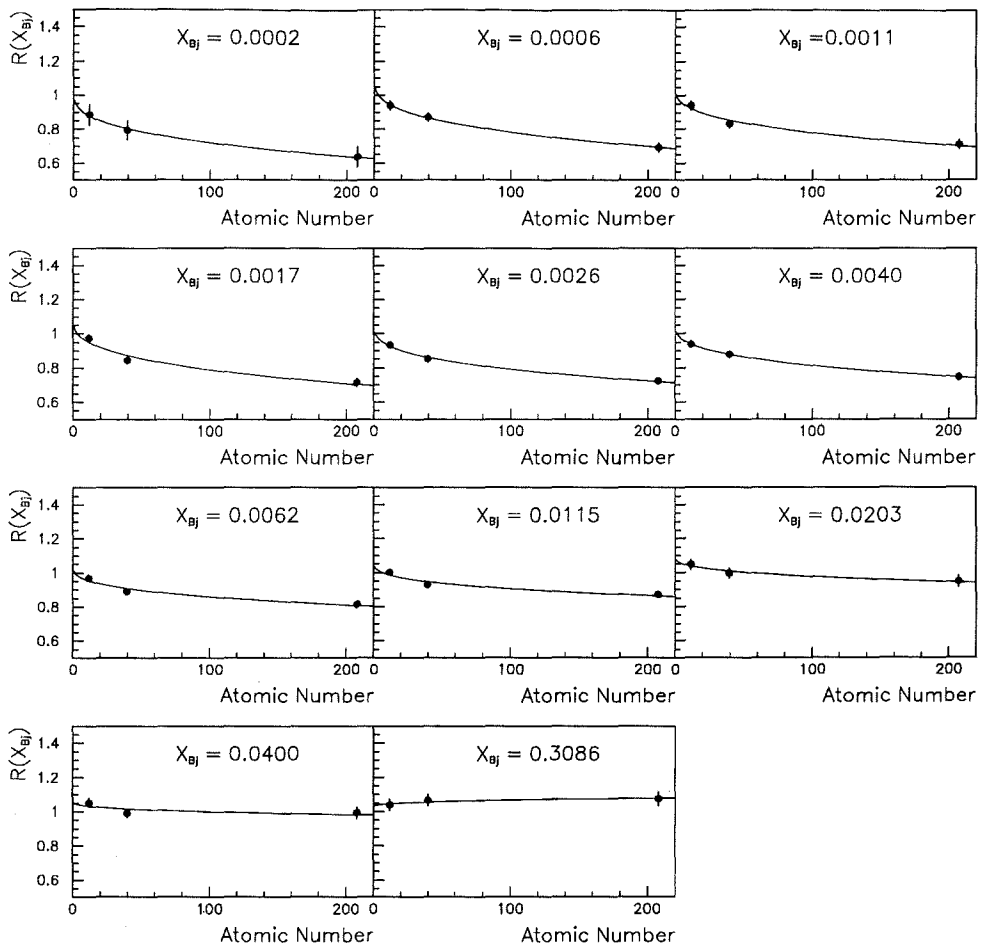

Figure 6.6: R(A) verses x_{Bj}

Conclusion

Based on the power-law fits to the model of Piller, this analysis is consistent with the GVD interpretation of shadowing. The model proposed by Piller and Wiese differs from the Bilchak model in its treatment of the virtual photon interaction inside the nucleus. Piller explicitly accounts for rescattering of the hadronic fluctuation inside the nucleus.

6.3 Q^2-Dependence

Most theoretical models agree than the Q^2-dependence of virtual photon shadowing should be approximately logarithmic at fixed x_{Bj}. In order to search for this relation, cross section ratios were plotted against $\mathrm{Log}_{10}(Q^2)$. The slope of the Q^2 ratio was extracted for each x_{Bj} bin. Figures 6.7, 6.8 and 6.9 show the ratio:

$$R(Q^2) \equiv \left.\frac{\sigma^{\mathrm{A}}}{\sigma^{\mathrm{D}}}\right| \tag{6.6}$$

at fixed x_{Bj} for carbon,calcium and lead, respectively. Error bars result from the error on the fitted slope. The results presented in table XXI indicated that the slope is well represented by a straight line in most x_{Bj} bins. The slopes are plotted against x_{Bj} in figure 6.10. The logarithmic Q^2-dependence of the data reproduces the predicted result. The result of a flat line fit has been superimposed and the fit results appear in table XXII. Fits indicate the logarithmic Q^2 dependence to be weakly correlated with x_{Bj}.

6.4 ν-Dependence

Finally, in figure 6.11 the cross section ratios have been presented as a function of the energy of the virtual photon, ν. The result of a fit to $\mathrm{R}(\nu) = A + B\nu$ appear in table XXIII. Tabulated ratios appear in Appendix A. The ν dependence is well represented by the linear fits. The slope of the line depends on the size of the nulceus. The ratio of heavier nuclei show a

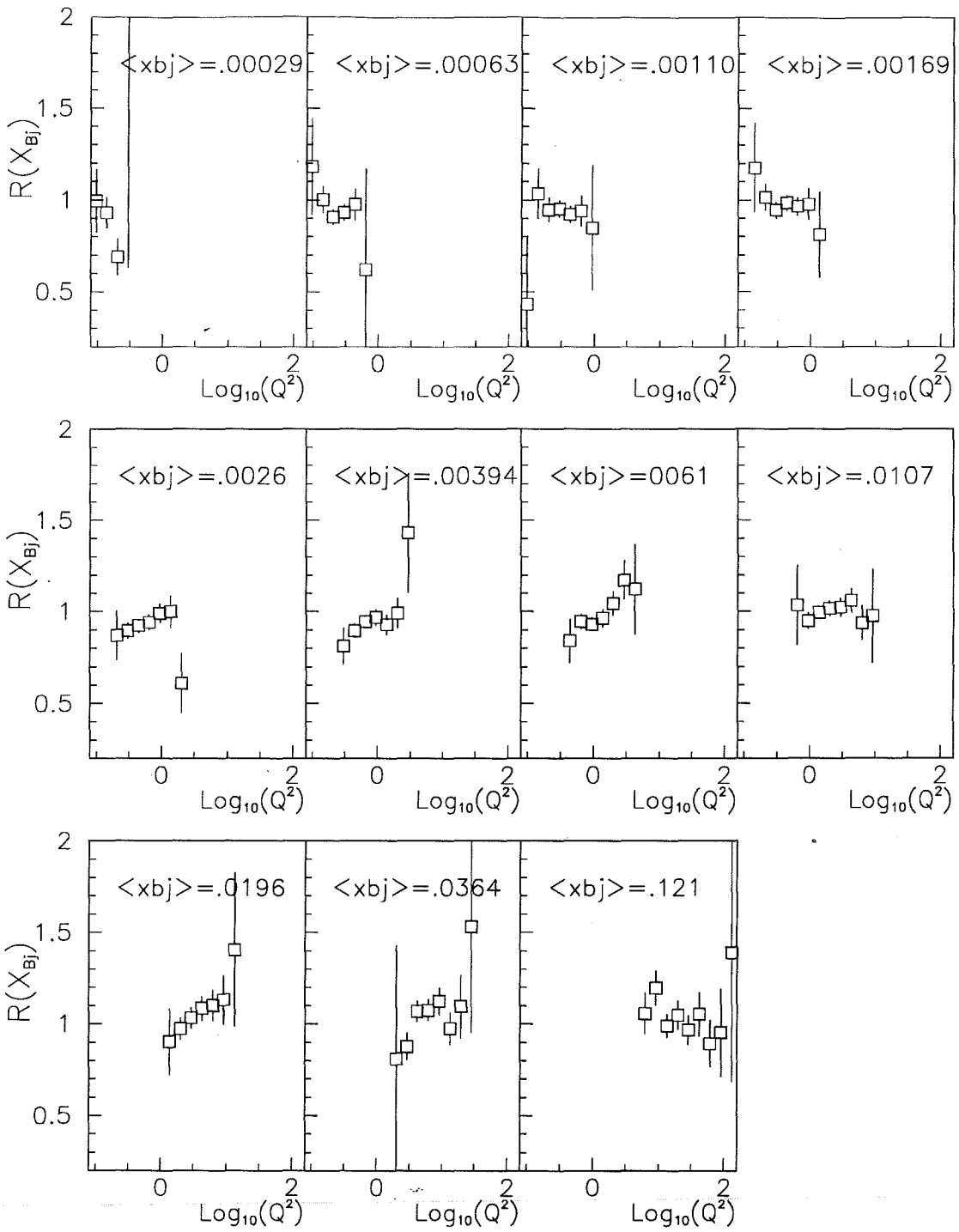

Figure 6.7: Q^2-Dependence of Shadowing for Carbon

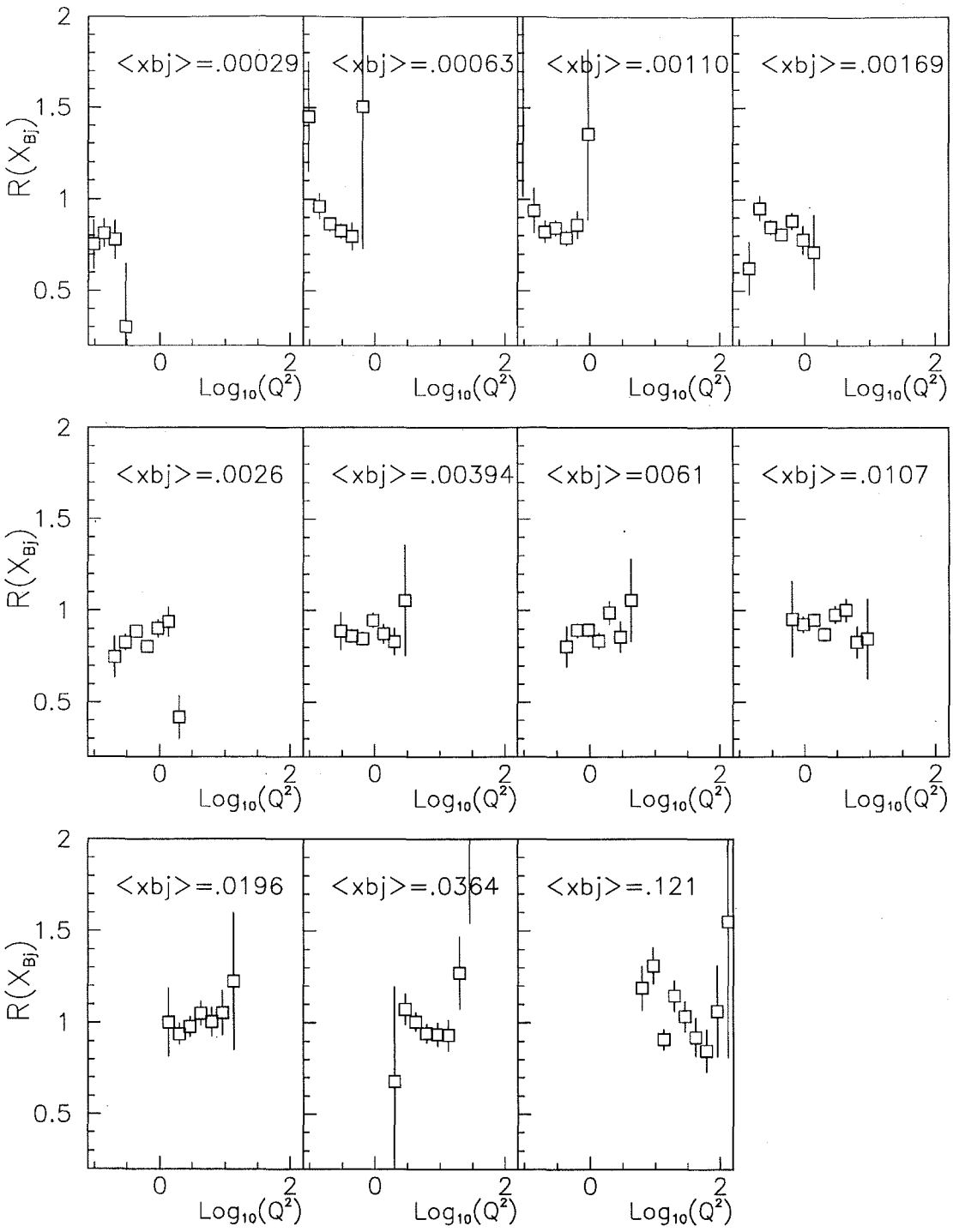

Figure 6.8: Q^2-Dependence of Shadowing for Calcium

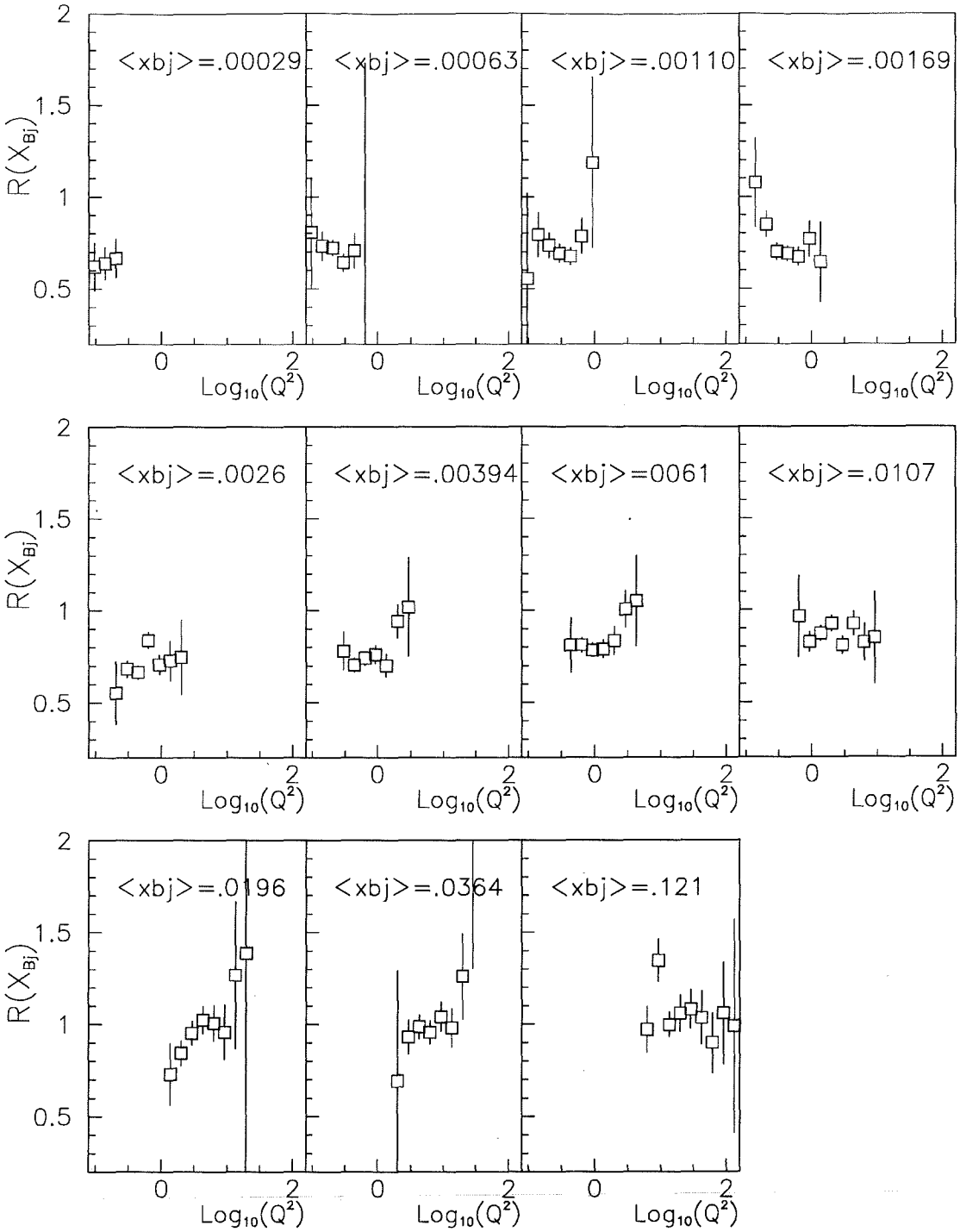

Figure 6.9: Q^2-Dependence of Shadowing for Lead

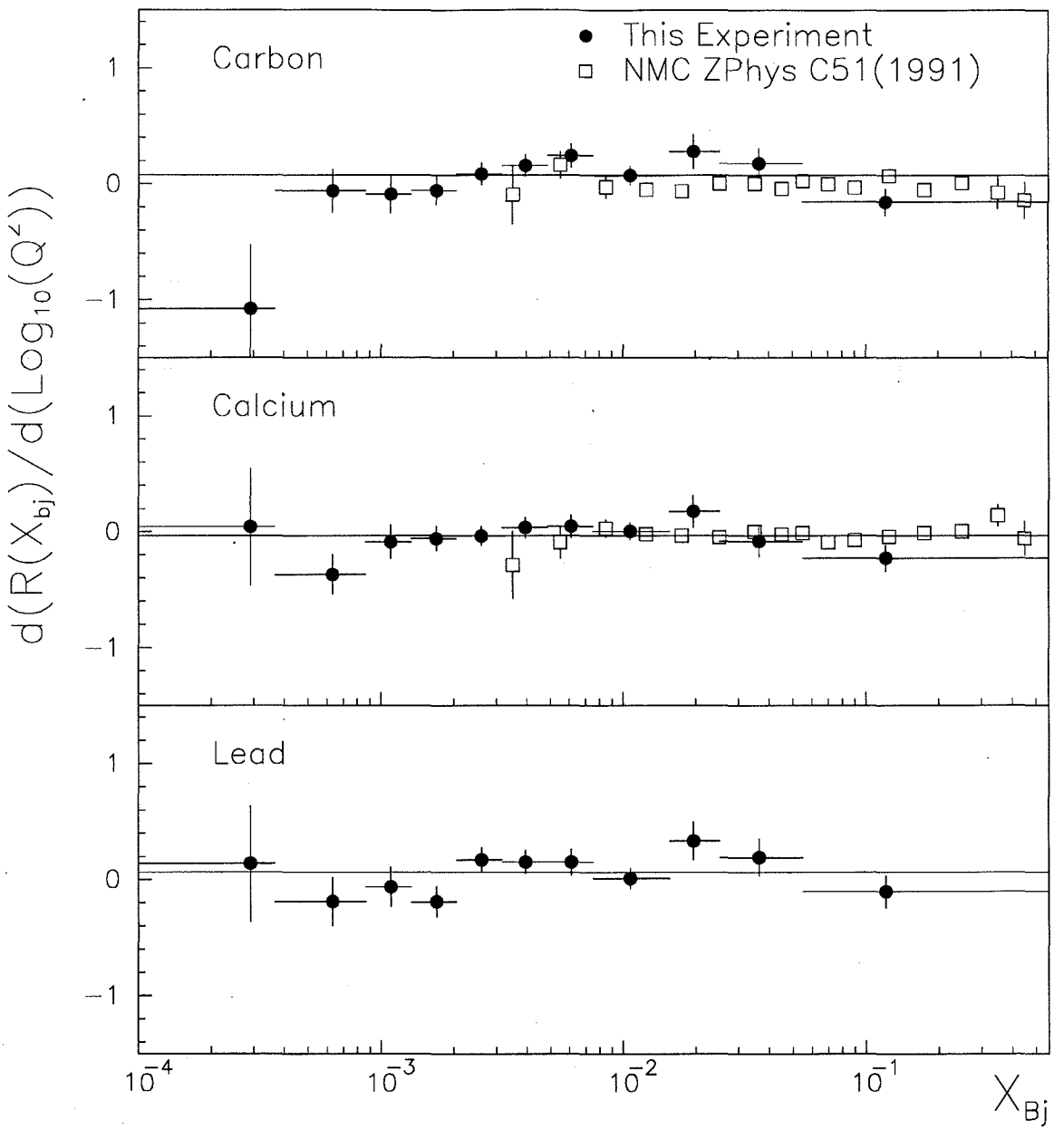

Figure 6.10: Logarithmic Q^2-Dependence vs x_{Bj}

TABLE XXI: d(R(x_{Bj}))/d(Log(Q^2)): Q^2-Dependence of Shadowing

	Carbon		Calcium		Lead	
$< x_{Bj} >$	Slope	χ^2/DOF	Slope	χ^2/DOF	Slope	χ^2/DOF
0.00029	-1.026 ± 0.55	1.59/ 2	-0.228 ± 0.46	1.89/ 2	0.137 ± 0.49	0.02/ 1
0.00063	-0.075 ± 0.18	2.67/ 4	-0.350 ± 0.17	3.79/ 4	-0.191 ± 0.19	1.19/ 4
0.00110	-0.037 ± 0.15	2.67/ 5	-0.075 ± 0.14	4.48/ 5	-0.021 ± 0.16	2.95/ 5
0.00169	-0.056 ± 0.12	1.83/ 5	-0.059 ± 0.10	7.54/ 5	-0.183 ± 0.12	5.12/ 5
0.0026	0.087 ± 0.10	6.07/ 5	-0.036 ± 0.08	19.7/ 5	0.172 ± 0.12	9.07/ 5
0.00394	0.161 ± 0.09	3.21/ 5	0.378 ± 0.08	4.51/ 5	0.152 ± 0.10	5.32/ 5
0.0061	0.246 ± 0.12	2.41/ 5	0.046 ± 0.95	5.40/ 5	0.153 ± 0.11	3.69/ 5
0.0107	0.072 ± 0.08	2.16/ 6	0.026 ± 0.08	7.42/ 6	0.095 ± 0.09	4.89/ 6
0.0196	0.282 ± 0.15	0.41/ 5	0.172 ± 0.14	0.95/ 5	0.333 ± 0.17	1.90/ 6
0.0364	0.176 ± 0.13	6.48/ 6	-0.083 ± 0.13	8.07/ 6	0.192 ± 0.16	3.23/ 6
0.121	-0.151 ± 0.11	4.15/ 7	-0.232 ± 0.11	16.7/ 7	-0.104 ± 0.14	8.11/ 7

stronger dependence on ν than lighter nucleii. A similar energy dependence has been observed in photoproduction (67). A comparision to the photoproduction result will be presented in the following section.

TABLE XXII: Q^2-Dependence Verses x_{Bj}

Target	dR(x_{Bj})/dLog$_{10}$(Q^2)	χ^2/NDOF
^{12}C/D	0.07731 ± 0.03664	17.14 /10
^{40}Ca/D	−0.03289 ± 0.03289	11.14 /10
^{208}Pb/D	0.06437 ± 0.0391	13.60 /10

TABLE XXIII: Linear Fits to R(ν) Verses ν

Target	A	B	χ^2/NDOF
^{12}C/D	0.974 ± 0.0159	$0.44 \times 10^{-5} \pm 0.1 \times 10^{-3}$	5.55/7
^{40}Ca/D	0.941 ± 0.0148	$-0.32 \times 10^{-3} \pm 0.100 \times 10^{-3}$	8.61/7
^{208}Pb/D	0.864 ± 0.0172	$-0.43 \times 10^{-3} \pm 0.12 \times 10^{-3}$	4.87/7

6.5 Comparison with Previous Results

Finally, the results of this analysis were compared with previously published results. Over the last twenty years there have been several muon and electron scattering experiments which have studied nuclear shadowing. In the following section I will compare to two experiments which most closely match the kinematic range of this analysis. In figure 6.12 this analysis was compare to shadowing results from the New Muon Collaboration(NMC) and 1987 E665 results. The carbon and calcium are compared with carbon and calcium NMC data (17). The lead result was compare to E665 run87 Xe(A= 131) data (8).

The arrow at the bottom of the plots indicated the expected ratio based on a parameterization of A_{eff}/A as measured in a photoproduction experiment (67). The A_{eff}/A as a function of photon energy, E_γ, in copper, was used to extract the energy of the photoproduction results. The A-dependence was determined at fixed photon energy for carbon,copper and lead targets. These effects were combined to yield

$$\frac{A_{eff}}{A}(E_\gamma, A) = 1.03 - 0.1611 \times \mathrm{Log}_{10}(A) - 0.672 \times 10^{-3}(E_\gamma). \tag{6.7}$$

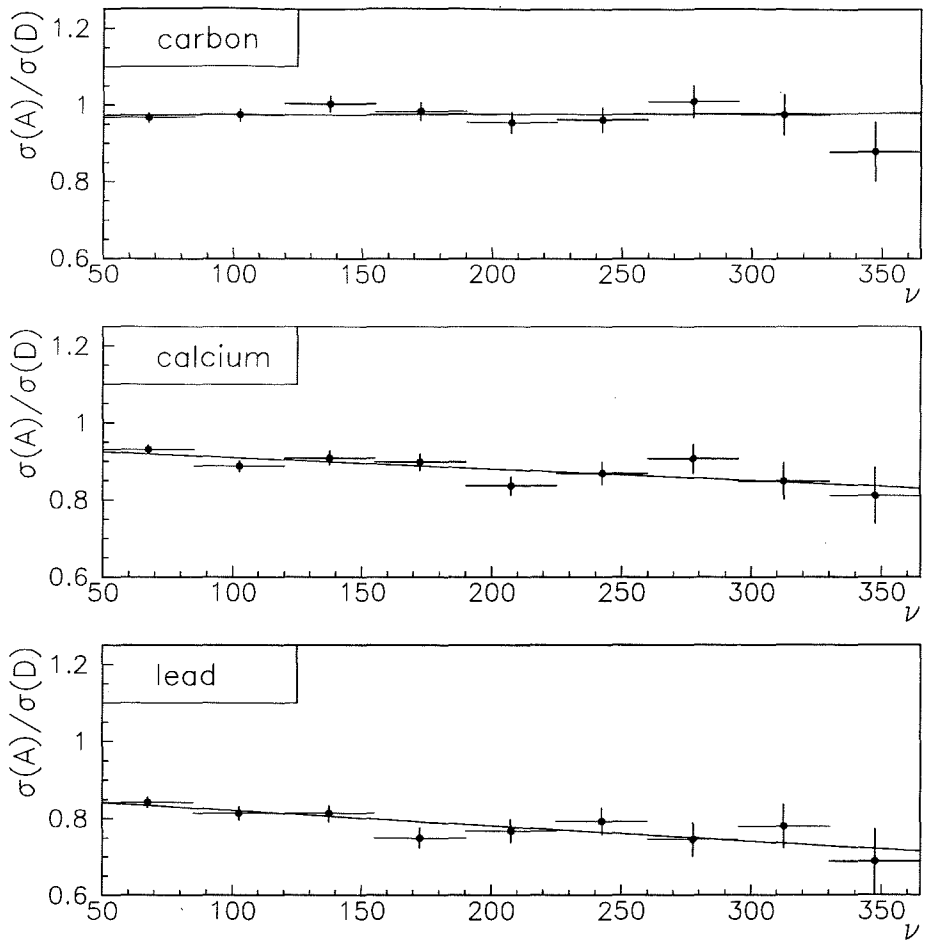

Figure 6.11: Nuclear Cross Section Ratios as a Function of ν

The the mean photon energy of the data at x_{Bj} below 10^{-3} was 210 GeV and was used to determine the expected amount of shadowing for real photons($Q^2 = 0.$) The results for carbon, calcium and lead are $0.714 \pm 0.056, 0.629 \pm 0.068$ and 0.514 ± 0.0623 respectively and are denoted by arrows in figure 6.12. The arrows indicate that shadowing at non-zero values of Q^2 is less pronounced than the shadowing of real photons.

This analysis agrees with previous E665 results despite the slightly difference in target. The

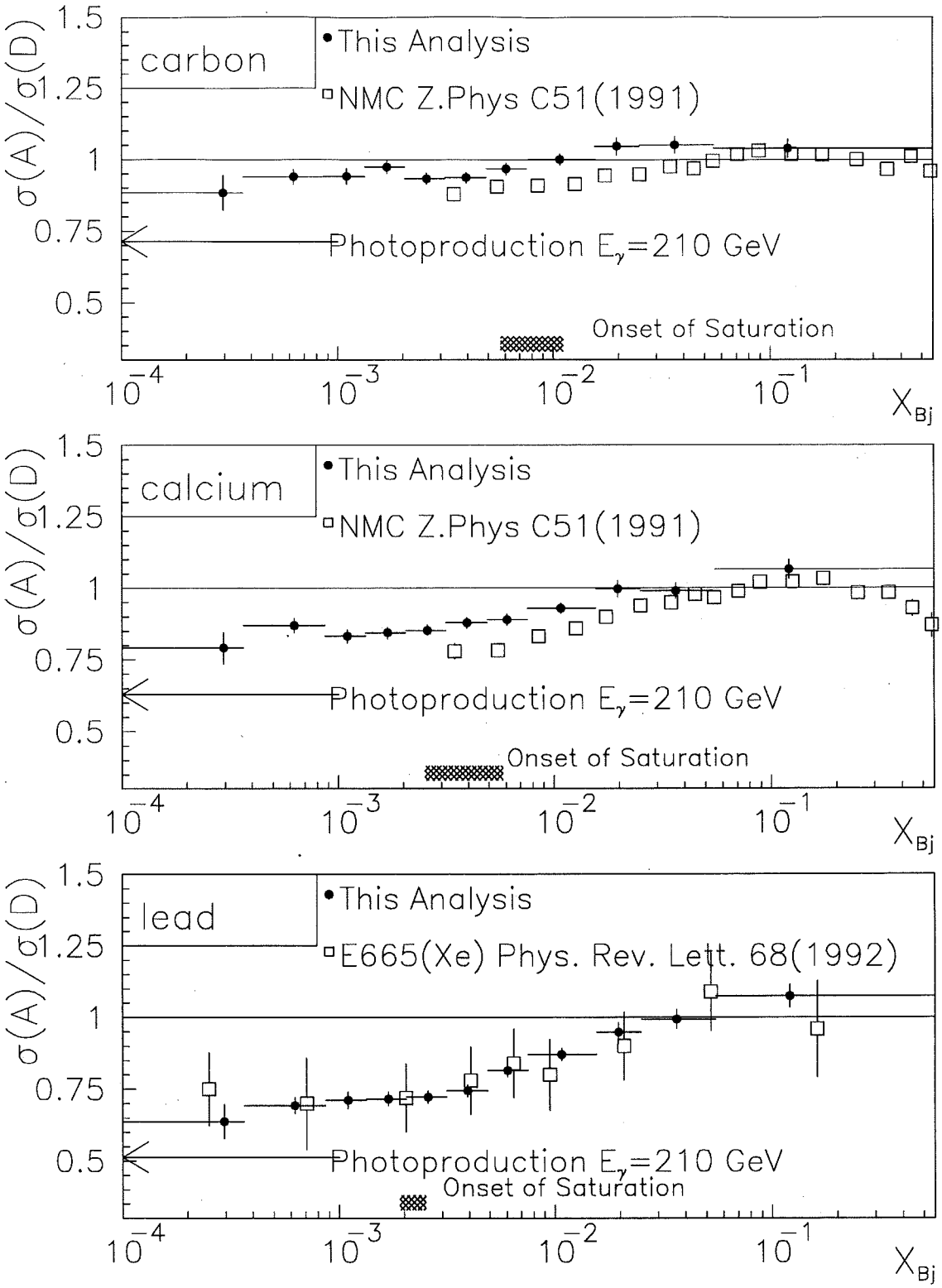

Figure 6.12: Comparison with Previous Results

large errors in the Xe/D data preclude any hard conclusions on the similarity between results. One might expect the Xe/D ratio to saturate at a higher level, R_s, as compared to the lead ratio. This discrepancy may be a result of the normalization of the run87 results. The errors on the Xe/D points are the quoted statistical and systematic errors in quadrature, an overall normalization uncertain of 10% has *not* been included. No correction for the non-isoscalarity of lead has been included. The isoscalarity correction was found to be less than 1% for $x_{Bj} < 0.1$.

The carbon and calcium results exhibit a more pronounced disagreement with previously the published results. The results of this analysis lie systematically higher than the NMC points in region $0.003 < x_{Bj} < 0.09$. The results converge at higher x_{Bj}, indicating it is not an error in the normalization of either data set.

In the region were the E665 data lie higher than the NMC results, Q^2 of the data are roughly equal. The Q^2 dependence of the NMC data was superimposed in figure 6.10. The Q^2-dependence of the NMC data are consistent with the E665 results. The most obvious difference between the two data samples was E665's use of the electromagnetic calorimeter for the identification of background processes. The NMC spectrometer was not instrumented with calorimetry, instead a Monte Carlo radiative correction procedure was used to correct their data.

Finally the ν dependence of the cross section ratios was compared to E665 xenon data (68) and the previously mention photoproduction experiment. The ν dependence of Xe/D ratio, and

the ratio A_{eff}/A as a function of photon energy, were fit to $A + B\nu$. The ratios and superimposed fits are shown in figures 6.13, 6.14.

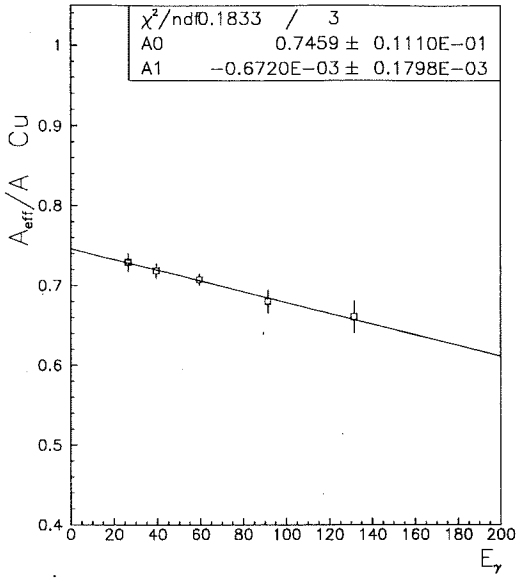

Figure 6.13: A_{eff}/A for Cu (Q^2=0)

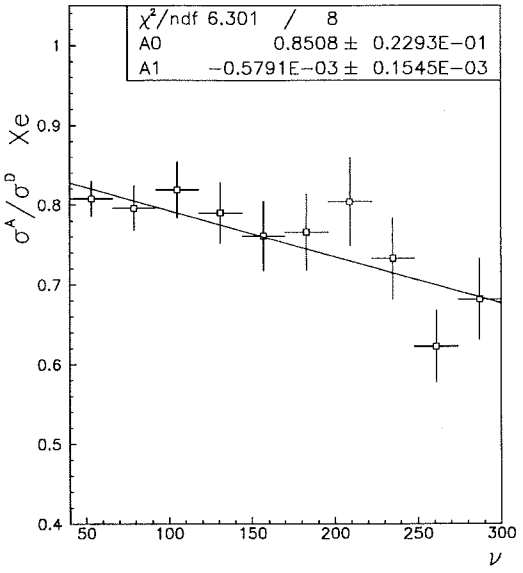

Figure 6.14: σ^A/σ^D E665 Xe

These slopes appear as an empty circle and triangle in figure 6.15. Figure 6.15 indicates the dependence of the cross section ratios on the virtual photon energy is more pronounced in larger nuclei. The muon DIS results exhibit a power law dependence on atomic number which is consistent with the photoproduction value.

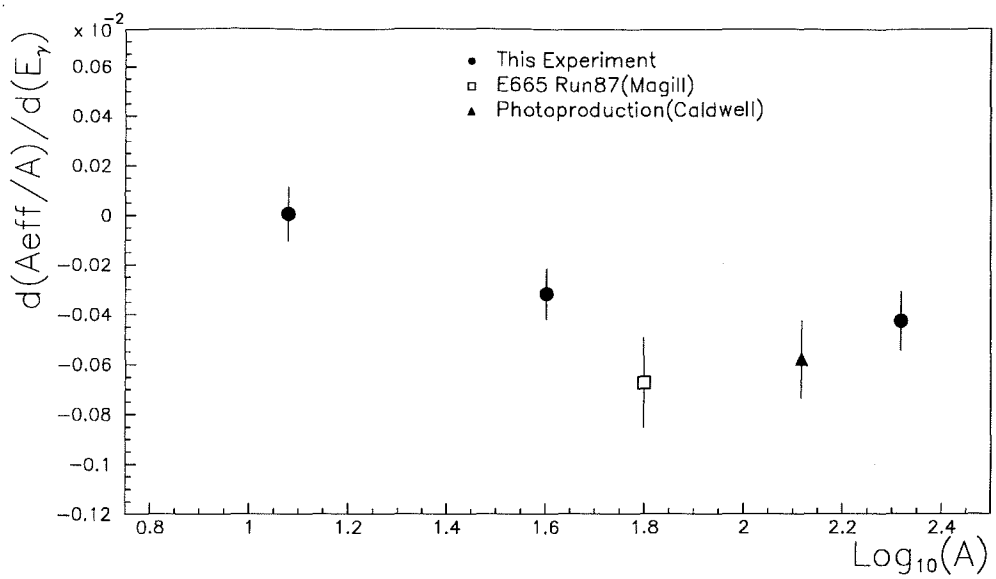

Figure 6.15: dR(ν)/dν Verses Atomic Number

6.6 Summary

The Q^2, ν and A-dependence of the per nucleon cross section ratios was studied. The ratios were observed to "saturate" at low x_{Bj}. The saturation region was defined using an iterative procedure which not only determined the value of the onset of saturation, but also the value of the saturated ratio $R_s(x_{Bj})$. The saturated ratios and onset of saturate were found to be target dependent, for larger target nuclei, the saturation becomes complete at lower x_{Bj} and lies below the ratio of lighter nuclei.

Both generalized vector dominance and parton recombination predictions of nuclear shadowing show qualitative agreement with this analysis. The logarithmic Q^2-dependence of the shadowing at fixed x_{Bj} was observed, in agreement with both models. The GVD interpetation

of Piller and Wiese shows agreement with the A-dependence of this analysis.

Previous measurements of carbon and calcium ratios were found to exhibit more shadowing than the results report here. The difference may be due to the method of background removal. The NMC analysis was based on Monte Carlo radiative corrections whereas this analysis removed background using an electromagnetic calorimeter.

The cross section ratios were found to show a linear dependence on the energy of the virtual photon, ν. The linear slope measured in this analysis was compared to run87 Xe/D results and a similar result measured at $Q^2 = 0$. The photoproduction result was found to be consistent with the E665 virtual photon data.

7. SUMMARY AND CONCLUSIONS

7.1 Summary

E665 has measured the per nucleon cross section ratios of carbon, calcium and lead relative to deuterium in inelastic muon-nucleus scattering. The kinematic range accessed by E665 has allowed these cross sections to be measured at lower values of $x_{Bj}(= Q^2/2\mathrm{M}\nu)$ than ever before. In the low x_{Bj} region, the per-nucleon cross section ratios exhibit shadowing. The shadowing observed is target dependent. For targets with larger nuclei, shadowing is more pronounced.

In the region where results have been presented, shadowing has been observed to saturate, meaning the ratios loose there dependence on x_{Bj}. The saturation of shadowing in carbon, calcium and lead targets has not been observed before this analysis. The A-dependence of shadowing can be approximated with an A^{α} form. The value of α was found to be x_{Bj} dependent, and reaches a minimum of $\alpha = -0.2$ at x_{Bj} below 0.001. The Q^2-dependence is logarithmic

if the scaling variable,x_{Bj} is held fixed. The ν dependence of shadowing is well represented by R(ν)=A+Bν.

The lead and calcium cross section ratios lie systematically higher than a similar measurement made by the New Muon Collaboration(NMC). The lead cross section agrees within the quoted errors to a previously published E665 result.

7.2 Conclusions

The cross section ratios in the low x_{Bj} region are proportional to the logarithm of the atomic number of the target. The observed Q^2 dependence is soft, and agrees with the predictions of both generalized vector dominance(GVD) and parton recombination(PR) interpretations of shadowing. The generalized vector dominance prediction of shadowing shows agreement with the A-dependence observed in this analysis. Additionally, A-dependent slopes of the R(ν) cross sections are consistent with photoproduction results.

Therefore, based on the predicted Q^2, and A-dependence of shadowing, along with the fact that the ν dependence is consistent with photoproduction results, I conclude the the shadowing measured in this analysis is a consequence of the interaction of the hadronic component of the virtual photon, as is predicted by generalized vector dominance models of shadowing.

Appendix: Tabulated Results

TABLE XXIV: Carbon/Deuterium Cross Section Ratio Verses x_{Bj}

$< x_{Bj} >$	σ^A/σ^D (stat) (sys)
.00029	0.885 +/- 0.0613 +/- 0.0771
.00063	0.940 +/- 0.0269 +/- 0.0204
.00110	0.941 +/- 0.0267 +/- 0.0079
.00169	0.974 +/- 0.0231 +/- 0.0155
.00260	0.934 +/- 0.0199 +/- 0.0164
.00394	0.937 +/- 0.0194 +/- 0.0194
.00610	0.968 +/- 0.0211 +/- 0.0336
.0107	1.001 +/- 0.0193 +/- 0.0222
.0196	1.047 +/- 0.0305 +/- 0.0359
.0364	1.052 +/- 0.0293 +/- 0.0199
.121	1.039 +/- 0.0331 +/- 0.0382

TABLE XXV: Calcium/Deuterium Cross Section Ratio Verses x_{Bj}

$< x_{Bj} >$	σ^A/σ^D (stat) (sys)
.00029	0.791 +/- 0.0552 +/- 0.0794
.00063	0.870 +/- 0.0246 +/- 0.0186
.00110	0.832 +/- 0.0237 +/- 0.0165
.00169	0.844 +/- 0.0203 +/- 0.0141
.00260	0.853 +/- 0.0181 +/- 0.0194
.00394	0.878 +/- 0.0181 +/- 0.0105
.0061	0.890 +/- 0.0195 +/- 0.0114
.0107	0.929 +/- 0.0178 +/- 0.0095
.0196	0.996 +/- 0.0291 +/- 0.0133
.0364	0.990 +/- 0.0274 +/- 0.0219
.121	1.065 +/- 0.0326 +/- 0.0525

TABLE XXVI: Lead/Deuterium Cross Section Ratio Verses x_{Bj}

$< x_{Bj} >$	σ^A/σ^D (stat) (sys)
.00029	0.638 +/- 0.0599 +/- 0.0886
.00063	0.693 +/- 0.0284 +/- 0.0182
.00110	0.711 +/- 0.0283 +/- 0.0127
.00169	0.715 +/- 0.0237 +/- 0.0216
.00260	0.723 +/- 0.0211 +/- 0.0168
.00394	0.745 +/- 0.0206 +/- 0.0169
.0061	0.815 +/- 0.0224 +/- 0.0194
.0107	0.870 +/- 0.0211 +/- 0.0164
.0196	0.948 +/- 0.0348 +/- 0.0343
.0364	0.994 +/- 0.0340 +/- 0.0180
.121	1.074 +/- 0.0400 +/- 0.0278

TABLE XXVII: Fully Corrected x_{Bj} Distributions for Deuterium

x_{Bj} bin	Events	$< Q^2 >$GeV^2	$< y_{Bj} >$
1	497	0.149	0.591
2	2831	0.250	0.473
3	2878	0.363	0.384
4	4129	0.460	0.319
5	5171	0.602	0.268
6	5544	0.824	0.240
7	4926	1.195	0.225
8	6112	2.176	0.231
9	2623	3.979	0.230
10	2965	7.091	0.223
11	2190	21.96	0.211

TABLE XXVIII: Fully Corrected x_{Bj} Distributions for Carbon

x_{Bj} bin	Events	$< Q^2 >$GeV^2	$< y_{Bj} >$
1	401	0.147	0.586
2	2446	0.250	0.475
3	2481	0.360	0.381
4	3647	0.461	0.318
5	4415	0.611	0.273
6	4713	0.846	0.244
7	4313	1.231	0.232
8	5559	2.198	0.232
9	2505	4.054	0.236
10	2806	7.177	0.224
11	2074	21.61	0.210

TABLE XXIX: Fully Corrected x_{Bj} Distributions for Calcium

x_{Bj} bin	Events	$< Q^2 >$GeV^2	$< y_{Bj} >$
1	440	0.150	0.598
2	2750	0.245	0.466
3	2664	0.359	0.383
4	3855	0.460	0.316
5	4918	0.604	0.270
6	5430	0.834	0.242
7	4918	1.203	0.227
8	6317	2.194	0.231
9	2968	3.992	0.231
10	3234	7.302	0.226
11	2558	21.32	0.207

TABLE XXX: Fully Corrected x_{Bj} Distributions for Lead

x_{Bj} bin	Events	$< Q^2 >$GeV^2	$< y_{Bj} >$
1	237	0.151	0.594
2	1529	0.249	0.465
3	1579	0.366	0.385
4	2247	0.460	0.314
5	2862	0.620	0.275
6	3111	0.851	0.246
7	2975	1.223	0.231
8	3968	2.162	0.227
9	1882	4.091	0.235
10	2191	7.263	0.226
11	1748	21.53	0.215

TABLE XXXI: Carbon/Deuterium Cross Section Ratio Verses ν

$< \nu >$(GeV)	$\sigma^{\mathrm{A}}/\sigma^{\mathrm{D}}$	$< Q^2 >$ (GeV^2)	$< x_{Bj} >$
66	0.967 $\pm$ 0.0125	2.76	0.023
101	0.973 $\pm$ 0.0158	3.08	0.016
136	1.003 $\pm$ 0.0202	3.46	0.014
171	0.983 $\pm$ 0.0235	3.11	0.009
206	0.954 $\pm$ 0.0270	3.73	0.009
242	0.962 $\pm$ 0.0323	3.31	0.007
276	1.010 $\pm$ 0.0410	2.68	0.005
310	0.975 $\pm$ 0.0529	2.43	0.004
345	0.878 $\pm$ 0.0773	3.30	0.005
377	1.205 $\pm$ 0.2468	4.90	0.006

TABLE XXXII: Calcium/Deuterium Cross Section Ratio Verses ν

$< \nu >$(GeV)	σ^{A}/σ^{D}	$< Q^2 >$ (GeV^2)	$< x_{Bj} >$
66	0.931 ± 0.0119	2.70	0.022
101	0.887 ± 0.0144	3.00	0.016
136	0.909 ± 0.0183	3.24	0.013
171	0.898 ± 0.0215	3.12	0.010
206	0.836 ± 0.0239	3.24	0.008
242	0.869 ± 0.0292	3.45	0.008
276	0.907 ± 0.0373	3.12	0.006
310	0.848 ± 0.0470	3.78	0.007
345	0.810 ± 0.0729	4.02	0.006
377	1.404 ± 0.2696	6.09	0.009

TABLE XXXIII: Lead/Deuterium Cross Section Ratio Verses ν

$< \nu >$(GeV)	σ^{A}/σ^{D}	$< Q^2 >$ (GeV^2)	$< x_{Bj} >$
66	0.842 ± 0.0137	2.80	0.023
101	0.814 ± 0.0170	3.42	0.018
136	0.814 ± 0.0213	3.52	0.014
171	0.750 ± 0.0257	3.73	0.012
206	0.767 ± 0.0298	3.97	0.010
242	0.793 ± 0.0349	3.42	0.008
276	0.746 ± 0.0432	3.49	0.007
310	0.780 ± 0.0565	3.75	0.006
345	0.688 ± 0.0850	4.06	0.006
377	1.132 ± 0.2492	2.42	0.003

CITED LITERATURE

(1) Weber, G., Proceeding 1967 International Symposium on Electron and Photon Interactions at High Energies , 59:75 (1967).

(2) Bjorken, J.D. , "Asymptotic Sum Rules at Infinite Momentum", Phys. Rev. **179**, 1547:1553 (1969).

(3) Feynman, R.P. Photon Hadron Interactions. Reading, Mass., W.A. Benjamin, Inc. 1972.

(4) Aubert, J.J. "The Ratio of the Nucleon Structure Functions F_2^N for Iron and Deuterium", Phys. Lett. **B123**, 275(1983).

(5) Stein, S. *et al* , "Electron Scattering at 4° with Enerergies of 4.5-20 Gev^2", Phys. Rev. **D12**, 1884 (1975).

(6) Bodek, A. ,*et al*, "Electron Scattering from Nuclear Targets and Quark Distributions in Nuclei", Phys. Rev. Lett. **50**, 1431 (1983).

(7) Bodek, A. and Ritchie, J.L., "Fermi-motion Effects in Deep-Inelastic Lepton Scattering from Nuclear Targets", Phys. Rev. **D23**, 1070(1981).

(8) Adams, M.R., *et al* , "Saturation of Shadowing at Very Low x_{Bj}", Phys. Rev. Lett. **68**, 3266 (1992).

(9) Bodek, A., *et al* , "Comparison of the Deep-Inelastic Structure Function of Deuterium and Aluminum Nuclei", Phys. Rev. Lett. **51**, 534 (1983).

(10) Arnold, R.G., *et al* , "Measurements of the A Dependence of Deep-Inelastic Electron Scattering From Nuclei", Phys. Rev. Lett. **52**, 727 (1984).

(11) Bari, G., *et al* , "Nuclear Effects in Deep Inelastic Muon Scattering on Deuterium, Nitrogen and Iron Targets", Phys. Lett. **B163**, 282 (1985).

(12) Benvenuti, A.C., *et al* , " Nuclear Effects in Deep Inelastic Muon Scattering on Deuterium and Iron Targets ", Phys. Lett. **B189**, 483 (1987).

(13) Ashman, J., *et al*, "Measurement of the Ratios of Deep Inelastic Muon-Nucleus Cross Sections on Various Nuclei Compared to Deuterium", Phys. Lett. **B202**, 603 (1988).

(14) Arneodo, M., *et al*, " Shadowing in Deep Inelastic Muon Scattering From Nuclear Targets", Phys. Lett. **B211**, 493 (1988).

(15) Arneodo, M." Nuclear Effects in Structure Functions ", CERN Preprint, CERN-PPE/91-119 , Geneva, Switzerland, (1992).

(16) Arneodo, M., *et al*, "Measurements of the Nucleon Structure Function in the Range 0.002<x<0.17 and 0.2 Q^2 8 GeV^2 in Deuterium, Carbon and Calcium", Nucl. Phys. **B333**, 1 (1990).

(17) Amaudruz, P., *et al*, "Precision Measurements of the Structure Function Ratios F_2^{He}/F_2^D, F_2^C/F_2^D and F_2^{Ca}/F_2^D", Z. Phys. **C51**, 387 (1991).

(18) Amaudruz, P., *et al*, "Precision Measurements of the Structure Function Ratios For ^{6}Li,^{12}C and ^{40}Ca", Z. Phys. **C53**, 73 (1992).

(19) Adams,M.R., *et al*, "Shadowing in the Muon-Xenon Inelastic Scattering Cross Section and 490 GeV", Phys. Lett. **B287**, 375 (1992).

(20) Goodman, M.S., *et al*, " Observation of Shadowing in the Virtual-Photon Total Hadronic Cross Section on Nuclei", Phys. Rev. Lett. **47**, 293 (1981).

(21) Aubert, J.J., *et al*, Phys. Rev. Lett. **B121**, 87 (1983).

(22) Amaudruz, P., *et al*, "Measurements of $R^d - R^p$ and $R^{Ca} - R^C$ in Deep Inelastic Muon Scattering", CERN Preprint, CERN-PPE/92-134, Geneva, Switzerland, (1992).

(23) Benvenuti, A.C., *et al*, " A High Statistics Measurement of the Deuteron Structure Functions $F_2(x, Q^2)$ and R From Deep Inelastic Muon Scattering at High Q^2" Phys. Lett. **B237**, 592(1990).

(24) Dasu, S., *et al*, "Measurement of the Difference in R=σ_L/σ_T and of σ^A/σ^D in Deep Inelastic e-D, e-Fe and e-Au Scattering", Phys. Rev. Lett. **60**, 2591 (1988).

(25) Dasu, S.,*et al*, " Preliminary results from a precision measurement of the x,q2 and nuclear dependence of R=σ_L/σ_T" University of Rochester preprint UR-958 ER-13065-452

(26) Stodolsky, L., "Hadronlike Behavior of γ, ν-Nuclear Cross Sections", Phys. Rev. Lett. **18**, 135 (1967).

(27) Bilchak, C.L., Schildknecht, D. and Stroughair, J.D., "Shadowing in the Deep Inelastic Muon Scattering on Heavy Nuclei", Phys. Lett. **B214**, 441-4 (1988).

(28) Bilchak, C.L., Schildknecht, D. and Stroughair, J.D., "On the A- and Q^2 Dependence of the Shadowing in Deep -Inelastic Scattering on Heavy Nuclei", Phys. Lett. **B233**, 461 (1989).

(29) Shaw, G.,"Shadowing in the Scaling Region", Phys. Lett. **B228**, 125 (1989).

(30) Piller, G. and Weise, W.,"Shadowing Effects in Deep Inelastic Lepton-Nucleon Scattering", Phys. Rev. **C42**, R1834-7 (1990).

(31) Nicolaev, N.N. and Zakharov, V.I., "Parton Model and Deep Inelastic Scattering on Nuclei", Phys. Lett. **B55** 397 (1975).

(32) Berger, E. L., Coester, F., "Nuclear Effects in Deep Inelastic Lepton Scattering", Ann. Rev. Nucl. Part. Sci. **37**, 463-92(1987).

(33) Qiu, J., "Nuclear Shadowing at Small Values of x", Nucl. Phys. **B291**, 746-764 (1987).

(34) Berger, E.L. and Qiu, J., "A-Dependence in the Shadowing Region of Deep Inelastics Scattering", Phys. Lett.**B206**, 141-144 (1988).

(35) Close, F.E., Qiu, J. and Roberts, R.G., "QCD /Parton Recombination and Applications to Nuclear Structure Functions", Phys. Rev. **D40**, 2820-2831 (1989).

(36) Berger, E, Qiu, J. , "Nuclear Dependence of the Structure Functions in the Shadowing Region of Deep Inelastic Scattering", Topical Conference on Nuclear Chromodynamics, Argonne National Laboratory, Argonne, IL., 119-133 (1988).

(37) Adams,M.R., *et al*, "A Spectrometer for Muon Scattering at the Tevatron", Nuclear Instruments and Methods in Physics Research **A291**, 533-551 (1990).

(38) "The Tevatron Muon Beam: A High Intensity Beam with Well Defined Polarization" Malensek, A. and Morfin, J. G., Fermilab Technical Memo TM1193, Fermi National Acceleror Laboratory, Batavia, IL. (1983).

(39) Fenker, H., "A Standard Beam PWC for Fermilab" Fermilab technical report TM-1179, Fermi National Accelerator Laboratory, Batavia, IL. (1983).

(40) Schellman, H., "The E665 Proton Calibration Run - Part I" E665 Internal Memo AN152, Fermi National Accelerator Laboratory, Batavia, IL. (1991).

(41) Spentzouris,P. and Schellman, H., "The E665 Proton Calibration Run - Part II" E665 Internal Memo AN153, Fermi National Accelerator Laboratory, Batavia, IL. (1992).

(42) Melanson, H., Kirk, T. and Wolbers, S. "Fermilab Drift Chamber System", E665 internal memo FL0027,FS010, Fermi National Accelerator Laboratory, Batavia, IL.(1985).

(43) Bratzler, U., "Design, Fabrication and Testing of a Low-Mass, Multiwire Proportional Chamber System for Experiment 665 at Fermilab" Masters Thesis, University of Washington , Seattle,WA. (1991).

(44) Schmitt, M., " Deep inelastic exclusive ρ^0 Production using 485 GeV Muons" PhD Thesis, Harvard University, Cambridge, MA. (1991).

(45) Nickerson, R. " CAL " E665 Internal memo EM012, Fermi National Accelerator Laboratory, Batavia, IL. (1988).

(46) Ramberg, E. " Neutral Pion and Eta Production in Deep Inelastic Muon Scattering at 480 GeV" PhD thesis, University of Maryland, College Park, MD, 1989.

(47) Kotwal, A., "Run90 Calorimeter Alignment", E665 Internal memo AN172 , Fermi National Accelerator Laboratory, Batavia, IL. (1993).

(48) Kotwal, A., "Correcting for Run90 Calorimeter Gas Gain Using the Gas Gain Monitor", E665 Internal memo AN173 , Fermi National Accelerator Laboratory, Batavia, IL. (1993).

(49) Kotwal, A., "Preliminary Run90 Calorimeter Calibration Using Electron Beam Data", E665 Internal memo AN175 , Fermi National Accelerator Laboratory, Batavia, IL. (1993).

(50) Jaffe, D., "The Small Angle Scintillator(SSA)" E665 Internal memo FS033, Fermi National Accelerator Laboratory, Batavia, IL. (1990).

(51) Wittek, W., "Reconstruction Efficiency and Ghost Rates for VDC Pattern Recognition" E665 Internal memo AN161, Fermi National Accelerator Laboratory, Batavia, IL. (1992).

(52) Carroll, T., "Status of the Event Scalers for Run90", E665 Internal memo AN107, Fermi National Accelerator Laboratory, Batavia, IL. (1991).

(53) Carroll, T., "Measureing Beam Flux with Random Beams", E665 Internal memo AN135, Fermi National Accelerator Laboratory, Batavia, IL. (1992).

(54) Carroll, T., "Implimentaion of Event Scaler Normalization in Run90/91", E665 Internal memo AN147, Fermi National Accelerator Laboratory, Batavia, IL. (1992).

(55) Ryan, J., "The TMC Guide to ZEBRA", E665 Internal memo SW102 , Fermi National Accelerator Laboratory, Batavia, IL. (1989).

(56) Melanson, H., "E665 Wire Chamber Pattern Recognition Users Guide", E665 Internal memo SW073 , Fermi National Accelerator Laboratory, Batavia, IL. (1989).

(57) Ryan , J., " Particle Production in Deep Inelastic Muon Scattering ", PhD thesis, Massachusetts Institute of Technology, Cambridge, MA. (1991).

(58) Salvariani, A., " Multiple Scattering in Track Fitting ", E665 Internal memo SW058 , Fermi National Accelerator Laboratory, Batavia, IL. (1988).

(59) Carroll, T. ," Using TRASTF to Improve the Muon Matching Efficiency ", E665 Internal memo SW185 , Fermi National Accelerator Laboratory, Batavia, IL. (1992).

(60) Schmitt, M., "A Modification to Nickerson's Pad Clustering Routine", E665 Internal memo EM017 , Fermi National Accelerator Laboratory, Batavia, IL. (1991).

(61) Kennedy, R.D., " Run90 Spill Scaler Normalization" E665 Internal memo AN100 , Fermi National Accelerator Laboratory, Batavia, IL. (1991).

(62) Carroll, T., " Muon Matching in the High y_{Bj} Region ", E665 Internal memo SW195, Fermi National Accelerator Laboratory, Batavia, IL. (1993).

(63) Ecker, U., " Determination of the Liquid Target Densities in E665 Run 1987/1988 ", E665 Internal memo AN025, Fermi National Accelerator Laboratory, Batavia, IL. (1988).

(64) Allspach, D., Kinney, E., Melanson, H., Peifer, J. and Schellman, H., " Calibration of E665 Liquid Target Readouts." E665 Internal memo AN102, Fermi National Accelerator Laboratory, Batavia, IL. (1991).

(65) Spentzouris, P., " H_2 and D_2 Target Densities for 91", E665 Internal memo AN203, Fermi National Accelerator Laboratory, Batavia, IL. (1994).

(66) Kinney, E., " Target Thicknesses" E665 Internal memo AN191, Fermi National Accelerator Laboratory, Batavia, IL. (1991).

(67) Caldwell, D.O.,*et al*, " Measurement of Shadowing in Photon-Nucleus Total Cross Sections from 20 to 185 GeV", Phys. Rev. Lett. **42**, 553 (1979).

(68) Magill , S., " XE/D_2 Cross Section Ratio From Muon Scattering at 490 GeV/c " PhD thesis, University of Illinois at Chicago, Chicago, IL. (1990).